Electron-Phonon and Electron-Electron Interactions in Quantum Transport

Gerhard Klimeck

January, 1994

School of Electrical Engineering
Purdue University
West Lafayette, Indiana 47907-1285

DISCARD THIS PAGE

Abstract

The objective of this work is to shed light on electron transport through sub-micron semi-conductor structures, where electronic state quantization, electron-electron interactions and electron-phonon interactions are important. We concentrate here on the most developed vertical quantum device, the double barrier resonant tunneling diode. In this work we analyze particle interactions in two structural limits: 1) large, and 2) small cross-sections, in which the treatments are fundamentally different. Large cross-section structures involve particle-interactions with many electrons and these effects can be described in the Keldysh formalism in a single-particle picture by effective potentials. We present model calculations treating the phonon-peak and electrical bistability in this limit. Small cross-section structures involve only a few particles, whose interactions cannot be described by effective potentials, due to strong particle correlations. The single-particle picture breaks down and a full many-body description has to be used. We present high bias calculations for electron transport through single quantum dots (artificial atoms) and an analysis of the linear response conductance spectrum of two coupled quantum dots (artificial molecules).

Acknowledgements

Table of Contents

List of Figures

List of Tables

Chapter 1

Introduction

1.1 Significance

The improvements of molecular beam epitaxy have reached a state where the deposition of material layers on an atomic length scale is possible.[1-5] State-of-the-art x-ray and electron beam lithography allows horizontal patterning on a nanometer scale.[6,7] These technologies have given rise to a new class of devices that operate on quantum-mechanical principles. Some of the devices are close to reaching commercial status but most of the structures are still in their infancy. The technology for constructing devices has improved much faster than the device modelling capabilities and consequently the understanding of electron transport in these so-called "mesoscopic structures" is a topic of current research.

Vertical Devices

Quantum phenomena are most evident when the electronic dephasing length* is large compared to the confinement. Quantum Devices can be categorized into 2 general classes, vertical and horizontal, (Fig. 1.1) indicating the direction of current flow with respect to the confinement. In vertical devices, electron transport occurs perpendicular to the epitaxially grown layers. The critical length scale of such devices is determined by the epitaxial layer thickness, which is typically of the order of 10nm. In such structures quantum effects occur at high bias and high temperature. Examples of devices in this class are single and multi-quantum well structures which have possible applications[1-4,8-23] as oscillators, detectors and switches.

Lateral Devices

In lateral devices, where electron transport occurs in the epitaxially grown plane the critical dimensions are determined by lithography. The feature sizes feasible today are of the order of 100nm which is a factor of 10 to 100 larger than the vertical epitaxial layer spacing. Interesting quantum effects such as conductance fluctuations, quantized conductance, Coulomb blockade and Aharanov-Bohm oscillations are mainly observed at liquid Helium temperatures and biases less than $k_B T/q$.[5-7] Lateral devices are still in their infancy due

---

*The dephasing length is, roughly speaking, the length over which an electron propagates without any inelastic scattering with other particles.

to these temperature and bias constraints and are of little practical significance. However, it is expected that quantum effects will arise at higher temperatures and larger bias as the feature sizes continue to decrease.
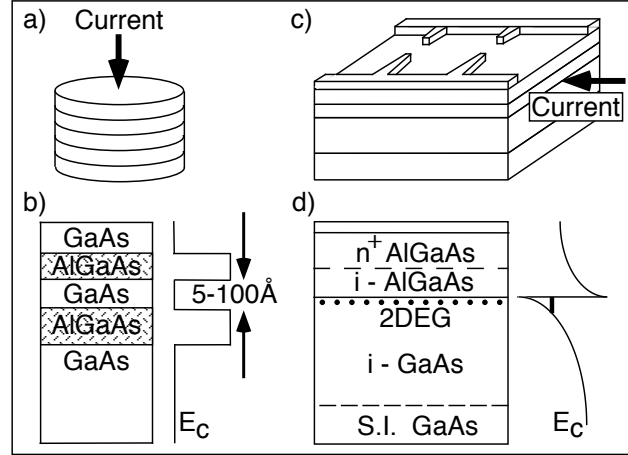
Figure 1.1 Structural comparison of vertical and horizontal quantum devices. (a) Example of a vertical structure. Current flow is along the direction of film growth and perpendicular to the film layers. (b) Vertical cut through the layers of a typical GaAs/AlGaAs structure with a corresponding conduction band profile. (c) Example of a horizontal structure. Electron transport is within one layer. (d) Vertical cut through the layers of a typical horizontal structure with a corresponding conduction band profile. By modulation doping a high mobility inversion layer is formed.

0–Dimensional Devices

Recently[24–29] vertical structures with finite cross-sections have been experimentally investigated, where electrons are confined in all three dimensions. Since the electrons do not have any translational degree of freedom, these structures are called zero-dimensional. Single electron tunneling, single electron-electron Coulomb interactions and 0–dimensional states have been observed.[7,24–32] With further advances in lithography, and in particular, the promise of STM lithography,[33] we envision semiconductor structures engineered on a nanometer scale in both the lateral and the vertical dimensions operating under high bias conditions. It can be expected that electron-electron interactions will play a more significant role, as they do in quantum chemistry[34] of atoms and molecules and many-body effects will become more important. This motivates our present modelling effort.

1.2 The Problem

1.2.1 Semi-Classical Transport

Electron transport in commercial semiconductor devices is usually modelled within the framework of drift diffusion. Electrons are assumed to scatter frequently with impurities, lattice vibrations and with each other. A constant driving force is needed to overcome the resistance due to scattering in order to transport the electron gas through a device.[35] As device structures become smaller, hot electron effects become important. Electrons scatter less frequently and may transverse a significant part of the device ballistically. Modelling of electron transport in this regime is usually undertaken using semi-classical Boltzmann type equations.[36] Sophisticated device simulators[37] accounting for many scattering mechanisms have been built and are already in use in many industry laboratories.

1.2.2 Coherent Transport

If the electron confinement shrinks under the length scales at which electrons scatter and lose their phase memory, the electron transport cannot be understood in semi-classical models anymore, but has to be described within a coherent quantum mechanical framework. Qualitatively, much of the transport phenomena in mesoscopic systems can be understood in terms of a single-particle picture, neglecting electron-electron interactions and inelastic processes in the device. Coherent transmission coefficients can be calculated from the Schrödinger equation and the flow of electrons can be treated as a scattering problem.[38–41] The single-particle picture employed in the treatment of coherent quantum transport neglecting phase breaking processes is a very intuitive one and can already be found in graduate level textbooks.[42]

We can therefore state that the two limits, 1) coherent single-electron, and 2) totally incoherent many electron transport are *in principle* well understood. Transport in the realm of mesoscopic devices, where electrons move coherently, where they may be correlated to other electrons and where they interact elastically or inelastically with impurities or the lattice is the challenge in our research area.

1.2.3 Transport in Interacting Systems

Importance of Electron-Phonon Interactions
Even in very pure materials inelastic scattering effects with the surrounding lattice occur for high energy electrons in a high bias device.[43] The lattice acts like a resonator, that can absorb (emit) energy from (to) the electrons. These electron-phonon interactions are present in every semiconductor (even at zero temperature) and are particularly strong in polar materials that are based on ionic bonding.[44, 45] For quantum devices operating in the high bias regime, inelastic scattering can play a crucial role in determining the correct transport physics.

A very clear demonstration of the importance of inelastic scattering on resonant tunneling is the appearance of the phonon-peak[43, 46–55] in the valley current of double-barrier

resonant tunneling diodes (DBRTD). The current is scattering enhanced over the non-resonant transmission due to electron-phonon interactions and a satellite peak past the main peak occurs in the current-voltage-characteristic (I–V–characteristic). Phonon peak currents as high as main resonance currents have been observed.[51]

We will be treating the problem of the phonon-peak on two levels. We first present numerical results using our simulator QUEST[56] in Chapter 2. In Chapter 3 we present a simple analytical model explaining the relative amplitude of the phonon peak to the main peak as a function of asymmetry in the structure. We will be deriving these results from a simple rate-equation based model and from the Green-function formalism of Keldysh, Kadanoff and Baym (KKB).[57–64]

Importance of Electron-Electron Interactions

Electron-electron interactions have been found to be important in DBRTD's as well. Large cross-section DBRTD's have a quantized density of states in one dimension and electrons have two degrees of freedom in the plane of the grown film.[42,65] Many electrons can therefore be accommodated in this resonant state and charge can be accumulated. Effects due to charge accumulation can generally treated in a macroscopic charging model,[66–68] where the quantum mechanical problem is treated in a single-particle picture and the influences due to other electrons are treated with "effective" potentials in the Hamiltonian. It is well understood that Coulomb charging shifts up the conduction band as well as the resonance level.[66–68]

The charge accumulation in the structure causes an intrinsic bistability,[66] which leads to a hysteresis in the I–V–characteristic. This hysteresis has been observed[46,47,55] in large cross section devices. We present numerical results of the bistability of asymmetric DBRTD's using our recently released simulator QUEST[56] in Chapter 2. We show, how a local charging potential introduces the bistability and represents experimental results correctly.

1.2.4 Strongly Correlated Transport

In small cross-section DBRTD's electronic states are quantized in three dimensions and electrons do not have a single degree of translational freedom (0D–structures). These so-called quantum dots can be filled with only few electrons[25,26] and transport can be considered to be determined by two physical effects: 1) the electronic state quantization to zero degrees of translational freedom, and 2) correlations of electrons due to charge interaction. Quantum dots have been called artificial atoms,[7] since the states in the quantum dots are determined by 1) the tight potential confinement and 2) the filling of the states with electrons.

Single electron tunneling and single electron charging effects have been observed in small cross-section DBRTD's.[24–29] The filling of a particular state by an electron in a quantum box of small size may change the spectrum of the other available states in the box significantly[34] and prohibit other electrons from tunnelling into the box (Coulomb Blockade[69–72]). The single electron Coulomb interaction may also give rise to a spin splitting of the resonance levels.[25,73] Evidence of the simultaneous importance of Coulomb blockade effects and inelastic processes in nanostructures has been recently reported.[74,75]

Electron-electron interactions can be treated in terms of "effective" potentials for large

cross-section DBRTD's, because a very large number of electrons interact with each other and a single electron "feels" an average potential due to all other electrons around it. This effective potential treatment breaks down if only few particles interact with each other, since they become strongly correlated. In Chapter 4 we work out a simple example showing how the "effective" potential point of view breaks down and we motivate the full many-body treatment in Chapters 5 and 6.

Chapter 5 treats electron transport through an artificial atom (quantum dot) at high bias including effects due to electron-electron correlation, subbands in the leads, and inelastic scattering. Chapter 6 treats linear response transport problems through coupled quantum dots, which could be considered artificial molecules.

1.3   Objective and Outline

The work presented in this report can be divided into two parts:

1. Large cross-section DBRTD's, where the treatment of electron transport is in a single-particle picture including interactions via "effective potentials" (Chapters 2 and 3), and

2. Small cross-section DBRTD's, where the treatment of electron transport is in a full many-body picture (Chapters 5 and 6).

Chapter 2 presents work we have performed with our recently released software package QUEST.[56] We start out with a brief explanation of the transport equation that is solved in QUEST. The mathematical details of the central quantities, the transmission coefficient, T, the occupation, f, and the scattering rate, $\frac{1}{\tau_\Phi}$, have been deferred to Appendix A. A simple calculation clarifying the "vertical flow" due to inelastic scattering is deferred to Appendix B. The results we have obtained with QUEST with respect to electron-phonon and electron-electron interactions deal with the phonon peak, Section 2.3, and electrical bistability, Section 2.4, in DBRTD's. In Section 2.5 we present simulation results that go beyond the 1D results presented in the previous sections.

Chapter 3 presents an analytical model for the phonon peak in resonant tunneling diodes based on a simple, intuitive rate equation picture. The simple results are supported by a rigourous derivation using a non-equilibrium Green-function approach. The work presented in Chapters 2 and 3 was performed in collaboration with Dr. Roger Lake.[56,76–81]

Chapter 4 discusses the fundamental limitations of effective potentials or self-energies to represent particle interactions in a single-particle picture, if only few particles are involved. If particles are strongly correlated, a full many-body approach has to be taken to calculate single-electron transport through small systems. This Chapter motivates the work that is described in Chapters 5 and 6.

Chapter 5 models high bias transport through quantum dots where electron charge correlation, inelastic scattering and the subbands in the leads have a strong influence. Starting from a rate equation model for sequential electron tunneling proposed by Beenakker[70] we include in a high bias calculation effects due to discrete subbands in the leads and inelastic

scattering within a single quantum dot. We show in three independent analytical examples how single-electron charge interaction, inelastic scattering, and non-adiabatic subband mixing can significantly enhance the valley current in finite cross-section double barrier structures significantly by opening new conduction channels. Numerical calculations of the high bias I–V–characteristics for a system of up to 26 electrons are presented. Symmetric structures with weak charge accumulation still show additional fine structure due to single-electron charging with little changes due to inelastic scattering. Asymmetric structures are shown to be a possible tool to estimate intra-dot relaxation times via high bias transport measurements. The work in Chapter 5 has been performed in collaboration with Dr. Roger Lake and Dr. Garnett Bryant.[82–86]

In Chapter 6 we investigate the linear response conductance through a pair of coupled quantum dots. The conductance spectrum under ideal conditions is shown to consist of two sets of twin peaks, whose locations and amplitudes are determined by the inter-dot coupling and the intra-dot charging. We will show that the qualitative features of the spectrum survive against experimental non-idealities such as detuning of the individual dots, inter-dot charging, multiple lateral states, and inelastic scattering. This work was performed in collaboration with Guanlong Chen.[87,88] An analysis of the linear response conductance of finite chains of quantum dots, whose mathematical and numerical treatment is similar to the work presented in Chapter 6 has been performed in collaboration with Guanlong Chen as well.[89]

Suggestions for future work are documented in Chapter 7, divided up along the line of this report into large cross-section DBRTD's and small cross-section DBRTD's. We suggest possible expansions of the simulator QUEST[56] to include a transverse momentum coordinate for the proper modelling of inter-subband scattering mechanisms and more realistic phonon modes. For our work with small cross-section DBRTD's we suggest further investigations into electron transport through single quantum dots including a better calculation of the many-body states and a investigation of transport through coupled quantum dots at high bias. We also suggest to connect the many-body approach to a single particle Green's function approach, to compare the two approaches and possibly to find an easier recipe to calculate conductance through a highly correlated electron system.

Chapter 2

Numerical Study: QUEST

2.1 Introduction

Our research group has developed and released two device simulators for the modelling of vertical devices in high bias at arbitrary temperature, SEQUAL[90] and QUEST[56,91] and one simulator for lateral devices at low bias and zero temperature, SQUALID-2D.[92] They have proven to be excellent tools in the understanding of electron transport in Mesoscopic structures.[91–96] In view of eminent device applications[1,2,8–23] of vertical structures at high temperature operation we have shifted our major interest to the modelling of these. QUEST and SEQUAL treat vertical structures as one-dimensional, where the material parameters may vary only along one, the material growth axis. SEQUAL was developed by Dr. Michael McLennan[90] and is based on the calculation of transmission coefficients assuming perfectly coherent electron transport. The body of the next generation program, QUEST,[56] was developed by Dr. Roger Lake[91,97] for the simulation of electron transport through vertical heterostructures including inelastic scattering based on the Green function formalism by Keldysh, Kadanoff and Baym (KKB).[57–64] I included a numerically stable, self-consistent charge interaction potential and electron-phonon scattering rates into QUEST and released it for public use.[56,76,77,91] QUEST has served us as a numerical tool in the analysis of several transport problems including electron-electron and electron-phonon interactions and we try to document its versatility and some of its limitations in this chapter.

In Section 2.2 we briefly introduce the transport equation which is evaluated in QUEST. Numerical results dealing with the problem of the phonon-peak in double-barrier resonant tunneling diodes will be given in Section 2.3. A very intuitive analytical model has emerged from these numerical results in the course of this numerical work and is presented in detail in Chapter 3.

In Section 2.4 we include simulations of the bistability of asymmetric DBRTD's due to charge accumulation. These calculation have exposed the limitations of a single-particle Hamiltonian in a system of highly correlated electrons to our research group and have lead us to work presented in Chapters 5 and 6. We will elaborate on these fundamental limitations of the single-particle picture employed in Chapter 4. In Section 2.5 we will use QUEST to

---

indicate the influence of multiple and infinite transverse modes on electron transport which will be compared against the results in Chapter 5.

2.2 Formalism

2.2.1 Multi-Probe-Formula

Most of the work of our research group has been inspired[64] by the Landauer approach[38, 39] which calculates the current through structures as a function of transmission coefficients and applied biases. The Büttiker[40] formula, in particular, has found widespread use. It relates the currents, I_i, at the probes, i, to the electro-chemical potential, μ_j, at the probes, j, by:

$$I_i = \frac{e^2}{h} \sum_j T_{ij} \ (\mu_i - \mu_j) \ .$$ (2.1)

The transmission coefficients T_{ij} are assumed** to connect the "probes", i and j, coherently at one energy. The equation can then be interpreted term by term as follows:

1. A particular chemical potential, μ_i, causes current to flow in lead, i, by transmission into the other leads, j.
2. The chemical potentials, μ_j, in the other leads, j, cause a back-injected current into lead, i.

The phases of the electrons become randomized in the ideal contacts while the transmission from contact to contact is perfectly coherent. This picture is very intuitive and the transmission coefficients, T_{ij}, may be calculated in a straight forward manner from a single-electron Schrödinger equation. Although quite successful in explaining many experimental observations (see for example References [98–100]), Eq. (2.1) is restricted to linear response[101, 102] and there were several other questions unanswered:

- How are phase breaking processes included?
- How can harmonic generation[103, 104] and large signal response[105, 106] be included?

2.2.2 Continuous-Probe-Formula

In the spirit of these questions Datta[64] has derived a continuous probe model, where the fundamental quantities are calculated based on a quantum kinetic approach. The current equation may now be written as

$$I(\vec{r}; E) = \frac{e}{h} \ \int d\vec{r}' \ T(\vec{r}, \vec{r}'; E) \ (f(\vec{r}; E) - f(\vec{r}';)) \ .$$ (2.2)

If each point, $\vec{r}$, in the device with associated energy, E, is assumed to be a terminal, we can then interpret the new Eq. (2.2) in a similar fashion as Eq. (2.1). The transmission

---

**The transmission coefficient matrix is symmetric, $T_{ij} = T_{ji}$, if there is no magnetic field in the device.

coefficient, $T(\vec{r}, \vec{r}'; E)$, connects transmission paths at the same energy from one "terminal", $(\vec{r}; E)$, to the next "terminal" ,$(\vec{r}'; E)$. The transmission between these new coordinates, $(\vec{r}; E)$ and $(\vec{r}'; E)$, is assumed to be coherent and once again the particles suffer phase breaking processes at these coordinates. In effect, every transmission path is delimited by phase breaking events (see Fig. 2.1).

This approach is good for the description of transport at high bias, including elastic phase breaking processes. In effect all energies are decoupled as visualized in Fig. 2.1. Eq. (2.2) may now be solved given the boundary conditions

$$
\begin{align}
I(\vec{r}; E) &= 0 & ,\{\vec{r}\} \in Device & \quad (2.3a) \\
f(\vec{r}; E) &= f_{Fermi-Dirac} & ,\{\vec{r}\} \in Contact & \quad (2.3b)
\end{align}
$$
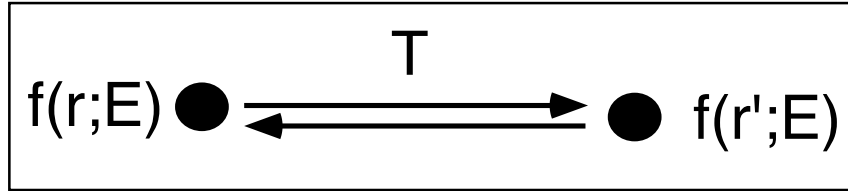
Figure 2.1 Coherent transport at *one* energy. Outflow from coordinate $(\vec{r}; E)$, back-flow from coordinate $(\vec{r}'; E)$. All energies are decoupled.

2.2.3   Inclusion of Inelastic Scattering

Inelastic processes couple different energy channels (Fig. 2.2). Each coordinate, $(\vec{r}'; E)$, which receives particles from another coordinate, $(\vec{r}; E)$, may be coupled to reservoirs at another energy at the same spatial coordinate, $\vec{r}'$, (local scattering). If, for example, all particles at $(\vec{r}'; E)$ are to be scattered away to other energies $(\vec{r}'; E')$ and $(\vec{r}'; E'')$, we do not have particles available to cause back-flow from $(\vec{r}'; E)$ into $(\vec{r}; E)$. The product of the occupation and the ratio of particle in-scattering and particle out-scattering $\left\{ f(\vec{r}'; E) \frac{I_{in-scatter}(\vec{r}'; E)}{I_{out-scatter}(\vec{r}'; E)} \right\}$ determines the effective occupation that is available for back-flow from $(\vec{r}'; E)$ into $(\vec{r}; E)$. We call this component the effective occupation, $f_\tau(\vec{r}'; E)$, which takes care of the coupling of the occupation at one spatial coordinate, $(\vec{r}'; E)$, to other energies, $(\vec{r}'; E')$, (see Fig. 2.2). We now write the transport equation including inelastic processes as

$$
\begin{align}
I(\vec{r}; E) &= \frac{e}{h} \int d\vec{r}'\, T(\vec{r}, \vec{r}'; E) \left(f(\vec{r}, E) - f(\vec{r}'; E) \frac{I_{in-scatter}(\vec{r}'; E)}{I_{out-scatter}(\vec{r}'; E)} \right) \\
&= \frac{e}{h} \int d\vec{r}'\, T(\vec{r}, \vec{r}'; E) \left(f(\vec{r}; E) - f_\tau(\vec{r}'; E) \right) . & (2.4)
\end{align}
$$

The effective occupation, f_τ, can be more formally defined as the ratio of the hole-out-scattering (electron in-scattering) and the total scattering (sum of hole and electron

out-scattering)

$$f_\tau\big(\vec{r}'; E\big) = \frac{\frac{1}{\tau_p(\vec{r}';E)}}{\frac{1}{\tau_\phi(\vec{r}';E)}} = \frac{\frac{1}{\tau_p(\vec{r}';E)}}{\frac{1}{\tau_p(\vec{r}';E)} + \frac{1}{\tau_n(\vec{r}';E)}} \ . \tag{2.5}$$

The hole out-scattering rates, $\frac{1}{\tau_p(\vec{r}';E)}$, the electron out-scattering rate, $\frac{1}{\tau_n(\vec{r}';E)}$, and the transmission coefficient, $T(\vec{r}, \vec{r}'; E)$, can be calculated from a microscopic model based on a non-equilibrium perturbative field theory approach by Keldysh, Kadanoff and Baym (KKB)[57–64] in a single-electron picture, where particle interactions are included by appropriate self-energies. The KKB formalism treats electrons and holes (the empty electron states) in one band on equal footing. Both carriers will have separate scattering rates associated with them. As in the usual valence and conduction band theory electrons tend to fall down in energy and holes tend to float up in energy.
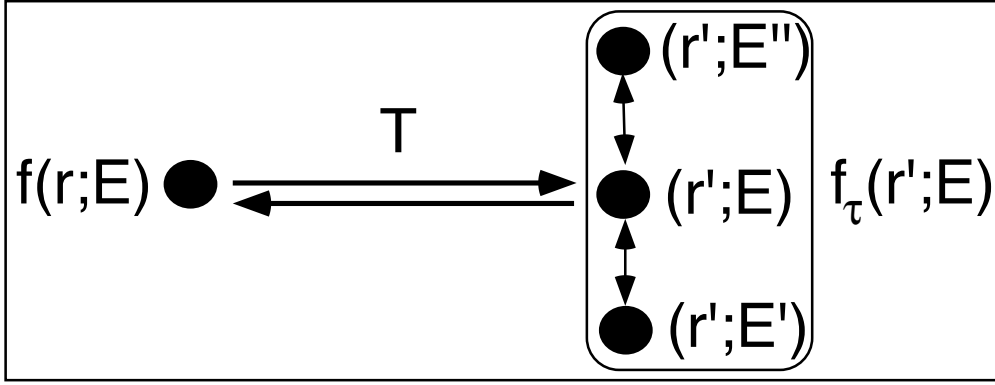
Figure 2.2 Inclusion of inelastic scattering. Outflow from coordinate $(\vec{r}; E)$, back-flow from coordinate $(\vec{r}'; E)$. The effective occupation available for back-flow at $(\vec{r}'; E)$ depends on other energies E' at the same site $\vec{r}'$. Different energy channels are now coupled, however, coherent transport is at one energy.

It is shown in Appendix A how the transmission coefficient, $T(\vec{r}, \vec{r}'; E)$, is related to the impulse response function of a single-electron Hamiltonian that includes the local interactions of the electron with the surrounding phonon bath via appropriate self-energies, which are in turn related to the scattering rates, $\frac{1}{\tau_p}$ and $\frac{1}{\tau_n}$. We will now consider optical phonons, which are assumed to have one particular eigen-energy, $\hbar\omega_0$. If we consider low temperatures, where $k_B T \ll \hbar\omega_0$, we can assume the Bose-Einstein factor to be negligible, $N = \frac{1}{exp\left(\frac{\hbar\omega_0}{k_B T}\right) - 1} \approx 0$. This means that all thermal phonons are frozen out and only spontaneous emission of phonons can occur. Our prescription for the calculation of the scattering rates in one dimension is then as follows (see Appendix A for details)

$$\frac{\hbar}{\tau_n(z; E)} = 2\pi U^2 \, N_0(z; E - \hbar\omega_0) \, (1 - f(z; E - \hbar\omega_0)) \ , \tag{2.6a}$$

$$\frac{\hbar}{\tau_p(z; E)} = 2\pi U^2 \, N_0(z; E + \hbar\omega_0) \, f(z; E + \hbar\omega_0) \ . \tag{2.6b}$$

These two terms indicate the electron out-scattering rate, $\frac{1}{\tau_n}$, and the hole out-scattering rate (= electron in scattering rate), $\frac{1}{\tau_p}$, at their particular coordinates, (z, E). The electron out-scattering rate at one particular energy, $\frac{1}{\tau_n(E)}$, is proportional to the density of states one optical phonon energy below, $N_0(E - \hbar\omega_0)$, and the probability to find an available state at that energy, $(1 - f(E - \hbar\omega_0))$. Electrons "look down" in energy to "find" an empty electron state. The hole out-scattering rate (electron in-scattering rate) at one particular energy, $\frac{1}{\tau_p(E)}$, is proportional to the density of states one optical phonon energy above, $N_0(E + \hbar\omega_0)$, and the probability to find an occupied electron state, $f(E + \hbar\omega_0)$. Holes "look up" in energy to find an empty hole state (i.e. an occupied electron state). A simple calculation of energy dependent scattering rates, $\frac{1}{\tau_n}$ and $\frac{1}{\tau_p}$, describing the "vertical flow" of electrons and holes due to optical phonon scattering can be found in Appendix B.

QUEST solves numerically for the transmission coefficient, T, the occupation, f, and the scattering rate, $\frac{1}{\tau_\Phi} = \frac{1}{\tau_n} + \frac{1}{\tau_p}$, self-consistently. The definition of the transmission coefficient, T, can be found in Appendix A Section A.3. The numerical algorithm for the self-consistent solution can be found in Reference [97].

2.3 Electron-Phonon Interactions: The Phonon-Peak

A very clear demonstration of the importance of inelastic scattering on resonant tunneling is the appearance of the phonon-peak[43, 46–55] in the valley current of double-barrier resonant tunneling diodes (DBRTD) (Fig. 2.3). If the bias condition is such that the resonance energy, E_r, is one optical phonon energy, $\hbar\omega_0$, below the energy of the incoming electrons, electrons can tunnel from the emitter into the well in the off-resonance condition, emit an optical phonon and thereby scatter down into the resonance state. The current is scattering enhanced over the non-resonant transmission through a double-barrier and a phonon peak occurs in the Current-Voltage-Characteristic past the main peak. The strength of the phonon peak seemed puzzling, since it did not scale in the same manner as the main peak in forward and reverse bias. In Fig. 2.3 we show our numerical results which reflect the different phonon peak to main peak ratios* in forward and reverse bias.

The Effect of Asymmetry, An Open Question

The phonon-peak problem and inelastic scattering in DBRTD's has been intensely theoretically investigated.[54, 107–126] However the question, why the phonon peaks scale differently with respect to the main peaks in forward and reverse bias had not been addressed yet.[76, 77] Essential in the occurrence of a scattering process is the availability of a scattering mechanism (electron-phonon interaction) and the availability of a final electron state. If a final state cannot be found for the scattering process, the scattering will be suppressed. This suggests that the filling of the resonant state may have an influence on the scattering rate and therefore on the strength of the phonon peak. The asymmetry in the DBRTD structure has been shown[46, 47, 55] to be the cause for charge accumulation (i.e. filling of the resonance)

---

*The difference of the main peaks (on a logarithmic scale) is about one order of magnitude, while the difference of the phonon peaks is more than two orders of magnitude.
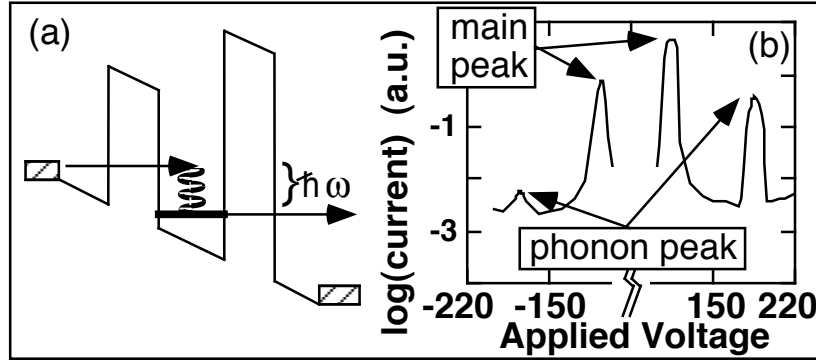
Figure 2.3 The phonon peak in DBRTD's. a) Conduction band (at forward bias) of a double-barrier resonance tunneling diode with bias such that the resonance is one phonon energy under the conduction band of the emitter. b) Current-Voltage Characteristic for forward and reverse bias neglecting charging effects. Left barrier is $220meV$ high, right barrier is $500meV$ high.

in one bias direction. Since the asymmetry of the structure leads to different degrees of filling in forward and reverse bias at the main peak, we are lead to believe that this is true also at the phonon peak and that the phonon peak strength is therefore also dependent on the asymmetry via the filling of the resonance.

Effect of Asymmetry, Numerical Approach

Using the simulator QUEST[56] we conducted the following numerical experiment in one dimension. We simulated the I–V–characteristics of several structures where we only varied the collector barrier height (Fig. 2.4). The main peaks show an expected behavior with respect to the collector barrier height, that can be modelled with the well known formula $\frac{\Gamma_E \Gamma_C}{\Gamma_E + \Gamma_C}$ where Γ_E (Γ_C) is the emitter (collector) transmission rate. The phonon-peak, however, behaves quite unexpectedly. It appears to be *independent of the collector barrier height* in the forward bias direction, but dependent on the emitter barrier height in the reverse bias direction. As observed in experiments, we obtain a phonon peak that is much stronger in forward bias than in reverse bias. These results leave us now with the following two questions:

1. Why is the phonon-peak in forward bias independent of the collector barrier?
2. Can we increase the collector barrier height ad infinitum and still carry current?

We will answer these questions in detail in Chapter 3. Regarding question number two, we state here in passing, that the phonon-peak current clearly has to be suppressed by extremely high barriers. This suppression is due to the filling of the resonance due to lack of outflow to the collector side. The filling of the resonance inhibits further scattering processes and the phonon-peak current will therefore be suppressed**. The Pauli-Exclusion Principle can therefore play a major role in the calculation of the scattering rate as the scattering rate is reduced if the final state is filled. A simple Fermi-Golden-Rule type calculation[107, 108]

**See Appendix B for a simple example explaining the suppression of the scattering rates due to the filling of the resonance.

involving only the scattering mechanism (the matrix element of the interaction) and the density of final states may not be good enough in asymmetric DBRTD's.

Effect of Asymmetry, Analytical Approach

In the course of this work we have been able to obtain analytical results for the off-resonant current and the filling of the resonance by collapsing the extended numerical problem into a 3 spatial node problem (emitter, well, and collector). These analytical results for the current and the filling of the resonance provide, for the first time, intuitive physical insight into the problem of one-dimensional transport through a resonant tunneling diode and will be presented in detail Chapter 3.
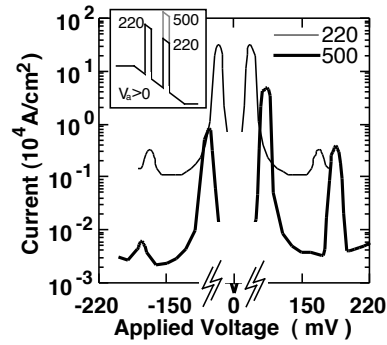
Figure 2.4 I–V–characteristic calculated for two different structures (see inset). Phonon-peak in forward bias remains unchanged and changes drastically in reverse bias. The main-peak changes with asymmetry in forward and reverse bias.

2.4 Electron-Electron Interactions: Electrical Bistability

The phonon peak was discovered somewhat by accident in the experimental studies of asymmetric structures in the search of proof of the predicted intrinsic bistability.[46,47,55] It is well understood[66,67] that Coulomb charging shifts up the conduction band as well as the resonance level. The charge accumulation in the structure causes an intrinsic bistability,[66] which is exposed by a hysteresis in the Current-Voltage-Characteristic. This hysteresis has been observed[46,47,55] in large cross section devices. Figure 2.5 depicts the mechanism of the bistability of the DBRTD. Without charging we assume the resonance of the density of states, which is centered in the double barrier structure (Fig. 2.5), to be linearly dependent on the applied bias. The thin dashed line in Figure 2.5b depicts the trace of the resonance
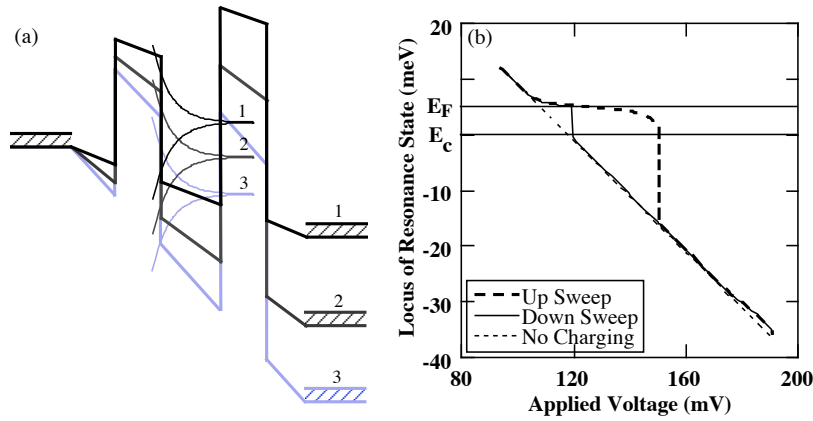
Figure 2.5 Locus of the resonance in a DBRTD. (a) Lorentsian density of states in the central region. Applied bias pulls down the resonance state proportionally without charging. (b) Locus of the resonance. Linear relationship without charging (thin dashed line). Hysteresis in locus due to charging (thick dashed line=increasing bias, solid line=decreasing bias).

peak as a function of applied bias, as almost linear[†]. The two horizontal lines indicate the conduction band edge and the Fermi-sea in the emitter. The resonance will start to fill up, as it gets close to the Fermi sea of the emitter with increasing applied bias[‡]. As the resonance fills up, negative charge accumulates and causes the conduction band in the center of the structure to float up. This charging pushes the resonance up in energy, opposes the lowering of the resonance and the resonance "floats" on top of the Fermi-sea, until the resonance is completely filled, thick dashed line in Figure 2.5b. Once the resonance is filled completely, it follows the increasing bias and is pulled down further. As the resonance crosses the conduction band edge of the emitter, the resonance cannot be filled from the

---

[†]The effective barrier lowering due to increasing bias (Figure 2.5a) changes the confinement of the resonant state and therefore changes the eigen-energy of the state. Since the barrier is relatively large in our simulation (500meV) we can neglect this effect here.

[‡]The degree of the filling of the resonance depends on the rate of in-flow through the emitter barrier and the rate of out-flow through the collector barrier. The filling of the resonance is significant if the collector barrier is higher/thicker than the emitter barrier.

---

emitter anymore[§], the resonance empties and falls down to the no charging locus. As the bias is decreased from high bias, the resonance follows the bias linearly until it "touches" the the conduction band edge of the emitter. The resonance fills up due to the inflow from the emitter and floats atop the Fermi-sea.

This hysteresis in the locus of the resonance is exposed in the I–V–characteristic of the DBRTD as shown in Figure 2.6. Electron charging leaves the "conduction channel"
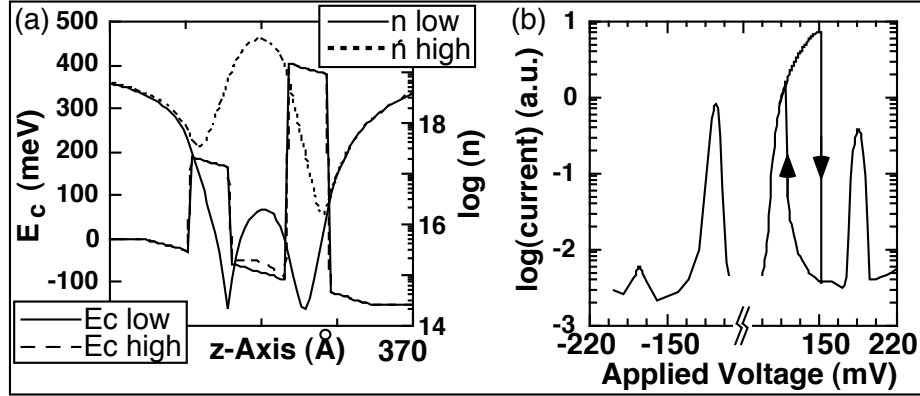
Figure 2.6 Electrical Bistability in the I–V–characteristic of an asymmetric DBRTD. a) Two conduction band profiles of a double barrier resonance tunneling diode at two bistable currents at one applied bias. Dashed line for the up-sweep of the applied voltage. Also shown is the calculated electron density for the two stable points. b) Current-voltage characteristic on a logarithmic scale from our simulation in a local charging model.

(between the Fermi energy, E_F, and the conduction band edge of the emitter, E_C) open for larger voltage range for increasing voltage sweeps than for decreasing voltage sweeps. Figure 2.6 considers two stable states of the locus of the resonance. One stable point is in the up-sweep of the applied voltage where the conduction band has floated up due to the charging (bulge in conduction band (dashed line) of quantum well), the other is in the down-sweep, where the conduction band drops off linearly. The charging has been calculated with a simplistic model[¶] of local charging only in the well, however it shows clearly the appearance of charge accumulation (continuous and dotted line in Fig. 2.6a) and hysteresis in the I–V–characteristic (Fig. 2.6b).

Note that there is no charging in the reverse direction or at the forward bias phonon peak. This indicates that for this particular structure a very low degree of charge accumulation is present in the quantum well at any other bias point but the forward bias main peak. The degree of filling of the resonance at the phonon peak will be addressed again in Chapter 3. We show here, how a local electro-static potential proportional to the number of electrons in the quantum well modifies the high bias I–V–characteristic significantly. The problem is

---

[§]We do not include inelastic scattering, due to acoustic phonons in this simulation, which would couple the resonance to the incident energy.

[¶]The single-electron Hamiltonian contains a potential of the form $V(z) = -q\frac{n(z)}{C(z)}$, where q is the elemental electron charge, $n(z)$ the electron-density and $C(z)$ a "local capacitance".

---

treated in QUEST[56] in one dimension for one lateral mode, the general behavior of large cross-section DBRTD's, however, is well described. On a linear scale the I–V–characteristic appears to have a ramp-like growing peak.[66]

2.5 Beyond 1–D

2.5.1 Lateral Modes

All simulations with QUEST presented so far are calculated for a single occupied lateral mode in one dimension. QUEST is laid out such that it can include several transverse subbands depending on the choice of cross section and Fermi energy. The wave-function in the transverse direction, given hard wall boundary conditions, can be expressed as sinewaves in terms of the transverse coordinates, x and y,

$$\psi(x,y) \propto sin\left(n_x\pi\frac{x}{d}\right) \times sin\left(n_y\pi\frac{y}{d}\right) \ , \tag{2.7}$$

where the quantum numbers, n_x and n_y, are positive definite. The length of the cross-section, d, is in this example assumed to be the same in the x and the y-direction. The corresponding eigen-energies in the transverse direction are

$$E_{n_x,n_y} = \frac{\hbar^2\pi^2}{2\ m^*\ d^2}\left(n_x^2 + n_y^2\right) \ . \tag{2.8}$$

QUEST assumes the structure to be homogeneous in the lateral dimensions and states with a particular set of lateral quantum numbers in the quantum well couple only to subbands in the leads with the same set of quantum numbers[‖]. The different lateral modes appear as independent channels through the structure.

In the following we will present an example calculation for a DBRTD structure with multiple occupied lateral modes. The turn-on biases of the lateral modes are determined by the energetic spacing of the modes, $\Delta E \propto \frac{\hbar^2\pi^2}{2m^*d^2}$, as the localized states in the quantum well are pulled down one by one with increasing applied bias into the Fermi sea of the emitter. The turn-off biases, however, are the same for *all* modes since all states in the quantum dot are aligned with the bottoms of their corresponding subbands in the emitter at the same bias. Table 2.1 lists the lowest lateral quantum states, indexed by the lateral quantum numbers, n_x and n_y, and ordered by their corresponding eigen energy, which is proportional to the sum of the squares of the quantum numbers, $n_x^2 + n_y^2$. In the particular simulation presented here, we have adjusted the Fermi energy such that the lowest four subbands are occupied in the leads.

Figure 2.7 depicts results of two sets of simulations obtained[56] with QUEST: 1) a single-moded, and 2) a multi-moded DBRTD. The particular device parameters can be found in Reference [56]. The turn-on and turn-offs have the general features described above. The lateral modes turn on one after the other, and they turn off all together. The four distinct

---

[‖]See Chapter 5 for a detailed discussion of this topic, including subband mixing

Table 2.1 Lowest transverse eigen modes listed by increasing transverse energy. Several of the eigen modes are degenerate.

States (n_x, n_y)	Degeneracy	$n_x^2 + n_y^2$	occupied
(1,1)	1	2	yes
(1,2),(2,1)	2	5	yes
(2,2)	1	8	yes
(1,3),(3,1)	2	10	yes
(2,3),(3,2)	2	13	no
(1,4),(4,1)	2	17	no
(3,3)	1	18	no

turn-ons correspond to the four occupied subbands listed in Table 2.1. Note that the second current step is twice as large as the first one due to the degeneracy of the $(2, 1)$ and $(1, 2)$ lateral states as indicated in Table 2.1. The fourth channel turns on only over a very small voltage range since the Fermi energy barely occupies the corresponding subband in the emitter. The current increases only slightly ($\sim 20\%$) within the energy window of the Fermi sea in the emitter for the single-moded DBRTD. We attribute this small increase to the increasing transmission rates through the emitter and collector barriers due to the effective barrier lowering by the applied bias.
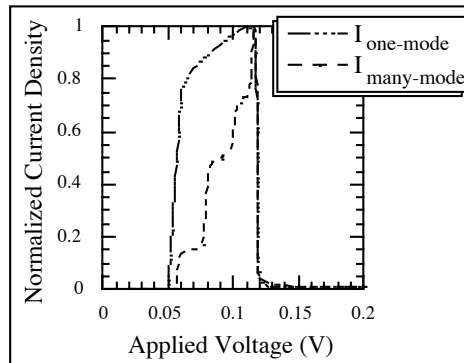
Figure 2.7 Comparison of current-voltage characteristics in the case of single-moded and multi-moded double barrier structures. Current is normalized to the maximum value. The first steps in the multi-moded and the single-moded structure are of the same height without normalization to the peak current. Note that the second current step for the many-moded structure is about twice as large as the first and the third current step. This corresponds to the degeneracy listed in Table 2.1. The forth step barely turns on since the forth eigen-energy is already close to the Fermi energy.

2.5.2   Infinite Cross-Section

QUEST can account for large transverse dimensions by assuming an infinite cross section with perfect translational invariance in the transverse directions. The wave-functions in the transverse dimensions become plane waves and the treatment of transverse energy co-ordinate becomes mathematically and numerically treatable.[91, 97] We will now compare the simulation with QUEST for an infinite cross-section DBRTD to the high bias I–V–characteristic of a single-moded and a multi-moded DBRTD of finite cross-section.

The three current voltage characteristics are depicted in Figure 2.8. They are normalized to their maximum current density. Note that the currents for the multi-moded and the infinite cross section structure are really scaled *down*. The first step in the multi-moded structure is really as big as the first step in the single-moded structure. The conductance along a one-dimensional structure is quantized** for each electron channel through the structure. The conductance only depends on the number of modes†† that are active in the current transport. Increasing the number of transverse modes therefore increases the conductance. The assumption of plane wave states in the transverse direction effectively places transverse modes infinitely small. Figure 2.8 shows nicely how the increase of number of nodes modifies the shape of the expected I–V–characteristic. The current steps due to
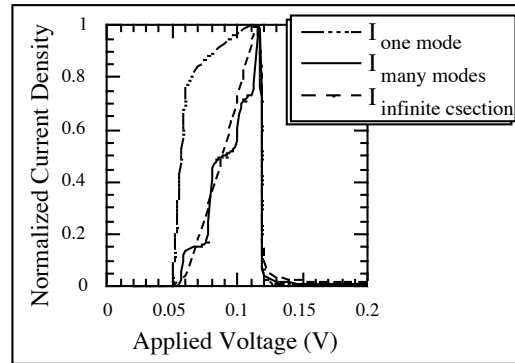
Figure 2.8   Comparison of current-voltage-characteristics of double barrier structures in the case of a single-moded, multi-moded and infinite cross section structure. The currents are normalized to their maximum value. The characteristics of the single-moded and multi-moded structure are repeated here for convenience from Figure 2.7.

adding transverse modes are smeared out in the limit of transverse plane waves. The step-like I–V–characteristic turns into a ramp-like I–V. We can understand this feature in the picture of infinitesimally closely spaced eigen energies (plane waves) whose momentum has to be matched by the electrons coming in from the Fermi-sea of the emitter. The number of electrons with transverse momentum, k, increases with the wave-vector, k, in the

---

**The barriers in our transport problem are very large so that the conductance through a single mode is much smaller than the conductance quantum of $e^2/\hbar$.

††The number of electrons in an electron waveguide is limited unlike the number of photons in an electro-magnetic waveguide since electrons are fermions that obey the Pauli-exclusion principle.

lead as $E(k) = \frac{\hbar^2 k^2}{2m^*}$, while the density of states in the quantum well is two dimensional ($\sim \Theta(E-E_R)$) due to the infinite cross section. The deeper the resonance "dips" into the Fermi-sea of the emitter, the more modes can be occupied and the current keeps increasing until the resonance drops under the conduction band of the emitter and transverse momentum conservation cannot be satisfied anymore.

The comparison between the finite and infinite cross section becomes even more interesting, if we look at the coherent and incoherent current components (see Figure 2.9). The
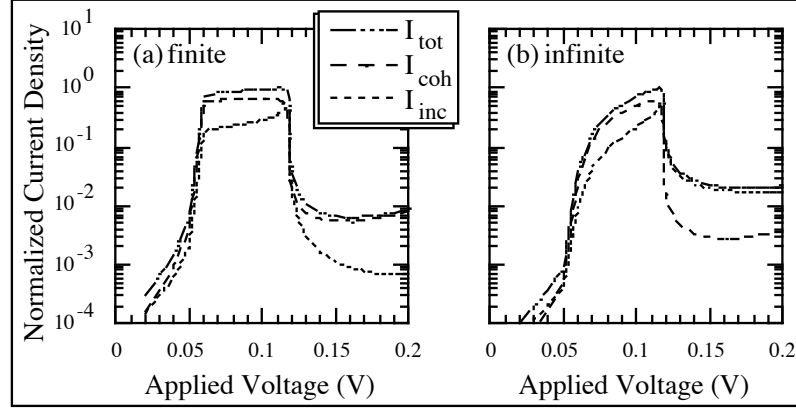
Figure 2.9 Comparison of current contributions for the single-moded and the infinite cross section case on a logarithmic scale. The dominance of the coherent over the incoherent contribution at resonance bias is the same for both cases. The incoherent contribution becomes negligible in the valley current in the single-moded case. The valley current of the infinite cross section structure, however, is carried by the incoherent contribution.

coherent current contribution accounts for all the electrons that are transmitted from the emitter to the collector without a single phase breaking event. The incoherent current contribution accounts for the electrons, whose phase was broken inside the device on their way from the emitter to the collector. In this example we had chosen[56] the elastic phase breaking rate such that the coherent and the incoherent current contributions to be of about the same order of magnitude at the main resonance peak for both, the single-moded and the infinitely moded, simulations. However, the distribution between coherent and incoherent currents is different in the two cases for the valley current. The valley current in the finite cross section device is mainly carried by the coherent current contribution, since the density of states in quantum well decreases rapidly. On the contrary, the valley current in the infinite cross section device is carried mostly by the incoherent current contribution. Elastic phase breaking events that randomize the momentum[‡‡] are still possible in a large (constant) two-dimensional density of states which does not exhibit a sharp cutoff. We will elaborate on the different effects of isotropic scattering in finite and infinite cross-section DBRTD's in Chapter 7, where we suggest improvements of QUEST's treatment of phase-breaking processes.

[‡‡]We have a local scattering potential here, which causes the scattering to be isotropic in k-space.

2.6 Conclusions

The released software package QUEST[56] has helped our research group significantly to analyze transport problems in large cross-section DBRTD's.[76–80] We have implemented into the simulator important mechanisms like electron-electron, electron-phonon interactions and modelled experimental results successfully. QUEST may prove to be a useful design tool for quantum devices, since it can be applied to many different vertical structures like multi-quantum wells and superlattices.

The fundamental limitations of QUEST with respect to electron-electron correlations in its single-particle description will be discussed in Chapter 4. These limitations have lead our research group to the work in Chapters 5 and 6 in which we use a full many-body model for electron transport.

Chapter 3

Analytical Study: The Phonon Peak

3.1 The Physical Picture

Inelastic scattering is of great interest from both basic and applied point of view for the understanding of electron transport through resonant tunneling structures.[43] A very clear demonstration of the importance of inelastic scattering is the appearance of the phonon-peak[46–55] in the valley current of double-barrier resonant tunneling diodes (DBRTD). If the bias condition is such that the resonance energy, E_r, is one optical phonon energy, $\hbar\omega_0$, below the energy of the incoming electrons, electrons can tunnel from the emitter into the well in the off-resonance condition, emit an optical phonon and scatter down into the resonant state. The current is scattering enhanced over the non-resonant transmission through a double-barrier and a "phonon peak" occurs in the current-voltage characteristic. The ratio of the phonon peak current to the main resonant peak current is enhanced by barrier asymmetry. Recently,[51] a phonon peak as large as the main peak was found. The fact that an off-resonant, inelastic channel carries as much current as the main resonant channel is surprising and has motivated our recent study of this phenomenon.[76,77] Here we present the simple, intuitive, rate equation picture that emerges from that work which summarizes the physics governing the ratio of the main peak current to the phonon peak current (see Fig. 3.1). We discuss the low temperature limit where we assume all relevant initial states in the emitter to be occupied ($f_E = 1$) and all relevant final states in the collector to be empty ($f_C = 0$). This parameter range corresponds to most experimental conditions.

A brief derivation of the current and occupation expressions based on a rate equation approach is given in Section 3.2. The full derivation based on a calculation on a one-dimensional tight-binding lattice can be found in Ref. [77]. The simple rate equation picture is supported by a rigourous treatment of transport based on the non-equilibrium Green function formalism at arbitrary temperatures and the derivations can be found in Section 3.3.
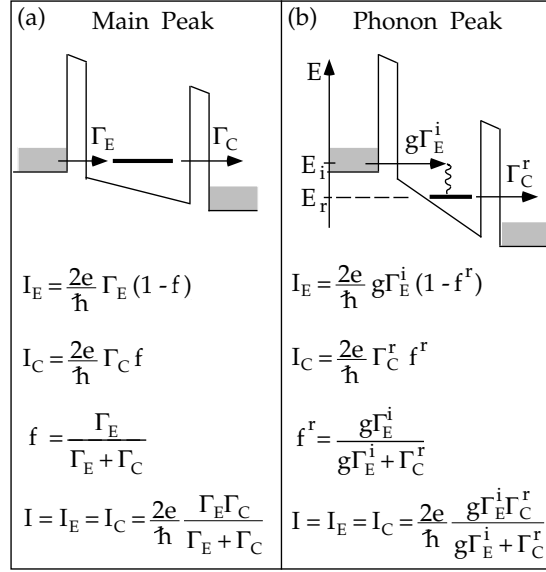
Figure 3.1 The phonon peak in DBRTD's: The physical picture. Rate equations corresponding to the (a) main peak and the (b) phonon peak in resonant tunneling diodes assuming low temperature ($k_B T \ll \hbar\omega_0$) and high bias ($f_E = 1$, $f_C = 0$). The superscripts, r and i, indicate that the quantity is to be evaluated at the resonant energy, E_r, and at the incident energy, $E_i = E_r + \hbar\omega_0$, respectively. $\Gamma_{E(C)}$ is $\hbar$ times the tunneling rate through the emitter (collector) barrier and $f_{E(C)}$ is the Fermi-factor in the emitter (collector) contact. f^r is the occupation of the resonance in the well. All the quantities for the main peak are evaluated at the resonant energy.

Before we discuss the analytical results for the phonon peak, we remind the reader of the well known results at the main peak. The amplitude of the main resonant current through a DBRTD is

$$I_{main} = \frac{2e}{\hbar} \frac{\Gamma_E \Gamma_C}{\Gamma_E + \Gamma_C}, \tag{3.1}$$

where $\Gamma_{E(C)}$ is the transmission rate of the emitter (collector) barrier (Fig 3.1a). For very asymmetric structures, where the emitter is much more transparent than the collector, $\Gamma_E \gg \Gamma_C$, the current decreases with the decreasing collector barrier transmission rate $I_{main} \approx (2e/\hbar)\Gamma_C$.

In a sequential picture the emitter current is proportional to the entry rate through the emitter barrier, Γ_E, multiplied by the probability of finding an empty resonant state, $(1-f)$. The collector current is proportional to the probability of finding a filled resonant state, f, times the out-flow rate into the collector, Γ_C. The filling of the resonance is given by the ratio of the in-flow, Γ_E, to the sum of in- and out-flow, $\Gamma_E + \Gamma_C$. The resonance starts to fill as the rate of out-flow, Γ_C, becomes smaller than the in-flow, Γ_E, and the current through the whole structure becomes limited by the availability of an unoccupied resonant state.

Figure 3.2 shows the filling of the resonance and the amplitude of the main-peak (m.p.) as a function of Γ_E/Γ_C. The current through the structure starts to roll off as the filling

of the resonance becomes significant at $\Gamma_E = \Gamma_C$. The current at the phonon peak bias
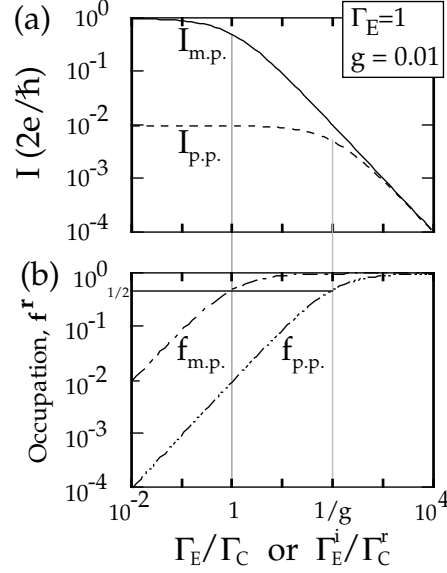
Figure 3.2 Current, I (a), and occupation of the resonance, f^r (b) at the main peak and the phonon peak assuming low temperature and high bias. $\Gamma_E(\Gamma_E^i)$ is fixed at $1meV$ and $g = 0.01$. Abbreviations $m.p.$ and $p.p.$ stand for main peak and phonon peak, respectively.

is intuitively assumed to exhibit the same behavior with respect to the collector barrier transmission rate. However, experiments[46,47,51,55] indicate that the ratio of the phonon-peak to main-peak current increases as the asymmetry of structures is increased.

The intuitive idea of sequential tunneling, where an electron hops from the emitter into the resonance and then out again into the collector proves to be very useful for the discussion of the phonon-peak as well. However, now an electron has to enter the structure through the emitter barrier *and* emit a phonon to hop into the resonance. Given some small probability, $g \ll 1$, to emit a phonon[§], we can model the total rate of entry into the resonance as $g\Gamma_E^i$, where the superscript, i, indicates the incident energy label (see Fig. 3.1b). The arguments for the current at this bias are now very similar to the ones presented at the main peak (Fig. 3.1b). The flow through the emitter barrier is proportional to the effective rate of tunneling, $g\Gamma_E^i$, and the availability of the resonant state, $(1-f^r)$, where the superscript, r, indicates the resonance energy. The out-flow through the collector depends on the filling of the resonance, f^r, and the rate of out-flow through the collector barrier, Γ_C^r. We can now see how all the expressions for the main peak can be symbolically transferred into the phonon-peak case by a substitution of Γ_E by $g\Gamma_E^r$.

The additional phonon emission process needed to tunnel into the resonance reduces the overall rate of in-flow into the resonance, which corresponds to an effectively more opaque emitter barrier. The collector barrier has to be even more opaque than this new effective

---

[§]We can here consider the probability g to be some empirical amplitude. The relation of g to a electron-phonon interaction Hamiltonian has been derived in Ref. [76].

---

emitter barrier in order for the resonance to fill. Structures have therefore to be much more asymmetric to fill the resonance at phonon-peak bias than to fill it at main-peak bias. Figure 3.2 compares the filling of the resonance at phonon peak (p.p.) bias to the filling of the resonance at main peak (m.p.) bias as a function of asymmetry (Γ_E/Γ_C). As long as the filling of the resonance is insignificant we can see that the phonon-peak current appears independent of the asymmetry for a wide range of parameters, whereas the resonance at main peak is already filled and the current decreases with increased asymmetry. At the phonon peak bias the resonance starts to fill (value $1/2$ in Fig. 3.2b) at about $\Gamma_C^r \leq g\Gamma_E^i$, and the two current peak amplitudes are about the same.

Our analysis predicts that very asymmetric structures can have a phonon-peak current which is as big as the main-peak current. These structures would also exhibit a significant filling of the resonance at the phonon-peak bias as shown by Turley.[51]

3.2 Rate Equation Approach

In the following section we will briefly sketch the idea of the rate equation model whose derivation starting from a tight binding model can be found in detail in Ref. [77]. We are interested in the occupation of a central resonant state (Fig. 3.3) and the inelastic current flow through this resonant state. We treat the single resonant state in the quantum well as weakly coupled to the emitter and the collector leads. The tunneling rates through the emitter and collector barrier are energy dependent as indicated with indices for incident and resonant energy, i and r, respectively. The number of thermally available phonons, N, is determined by Bose-Einstein statistics. The small, dimensionless quantity, g, determines the electron-phonon coupling strength. Every transition "up" in energy, i.e. from the resonance
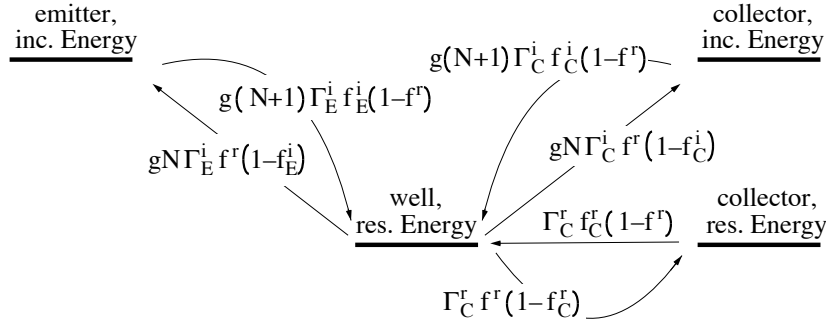
Figure 3.3 Rate-equation set-up for the phonon-peak problem. Superscripts i and r stand for incident and resonant energy, respectively. The electron-phonon interaction strength is indicated by g, the number of available phonons by N and the tunneling rates through the emitter (collector) barrier by $\Gamma_{E(C)}$.

energy, r, to the incident energy, i, requires the absorption of a phonon and is therefore proportional to the number of available phonons, N. A transition "down" in energy, i.e. from the incident energy, i, to the resonant energy, r, is allowed by spontaneous emission and stimulated emission of a phonon and the rate of such processes is proportional to $(N{+}1)$.

Within this model we denote the in-flow rate, Γ_{in}, and out-flow rate, Γ_{out}, to the resonant state as

$$\Gamma_{in} = \left[g(N+1)\Gamma_E^i f_E^i + g(N+1)\Gamma_C^i f_C^i + \Gamma_C^r f_C^r \right](1-f^r) , \qquad (3.2a)$$

$$\Gamma_{out} = \left[gN\Gamma_E^i \left(1-f_E^i\right) + gN\Gamma_C^i \left(1-f_C^i\right) + \Gamma_C^r (1-f_C^r) \right] f^r . \qquad (3.2b)$$

Assuming steady state with equal in-flow and out-flow, $\Gamma_{in} = \Gamma_{out}$, and solving for the occupation at the resonance, f^r, results in

$$f^r = \frac{\Gamma_C^r f_C^r + g(N+1)\left(\Gamma_E^i f_E^i + \Gamma_C^i f_C^i\right)}{\Gamma_C^r + gN\left[\Gamma_E^i\left(1-f_E^i\right) + \Gamma_C^i\left(1-f_C^i\right)\right] g(N+1)\left[\Gamma_E^i f_E^i + \Gamma_C^i f_C^i\right]} \qquad (3.3)$$

The inelastic current is given by the net flow through either the emitter or the collector barrier. For the net flow through the emitter barrier we denote (including a factor of 2 for spin degeneracy)

$$I_{inelast} = \frac{2e}{\hbar}\left[g(N+1)\Gamma_E^i f_E^i (1-f^r) - gN\Gamma_E^i f^r \left(1-f_E^i\right)\right] \qquad (3.4)$$

Substituting Eq. 3.3 into Eq. 3.4 results in two distinct current contributions.

$$\begin{aligned} I_{inelast} &= \frac{2e}{\hbar}\frac{g(N+1)\Gamma_E^i f_E^i \Gamma_C^r (1-f_C^r) + gN\Gamma_E^i \left(1-f_E^i\right)\Gamma_C^r f_C^r}{\Gamma_C^r + gN\left[\Gamma_E^i\left(1-f_E^i\right) + \Gamma_C^i\left(1-f_C^i\right)\right] + g(N+1)\left[\Gamma_E^i f_E^i + \Gamma_C^i f_C^i\right]} \\ &+ \frac{2e}{\hbar}\frac{g^2 N(N+1)\Gamma_E^i \Gamma_C^i \left(f_E^i - f_C^i\right)}{\Gamma_C^r + gN\left[\Gamma_E^i\left(1-f_E^i\right) + \Gamma_C^i\left(1-f_C^i\right)\right] + g(N+1)\left[\Gamma_E^i f_E^i + \Gamma_C^i f_C^i\right]} \qquad (3.5) \end{aligned}$$

The first current contribution is due to one-phonon processes in two different directions; electron transport from 1) the emitter to the collector, and 2) the collector to the emitter. In the first direction, with the positive contribution, an electron is injected from the emitter at the incident energy $(\Gamma_E^i f_E^i)$, emits spontaneously or stimulated a phonon $(g(N+1))$, and is transmitted to the collector at the resonance energy $(\Gamma_C^r (1-f_C^r))$. In the second direction an electron is injected from the collector at the resonance energy $(\Gamma_C^r f_C^r)$, absorbs a phonon (gN) and is transmitted to the emitter at the "incident" energy $(\Gamma_E^i (1-f_E^i))$.

The second current contribution in Eq. (3.5) is of second order in the electron-phonon interaction strength, g, and describes two-phonon-interaction processes, where one phonon is emitted and one phonon absorbed and the initial and final energy of the transmitted electron is at the incident energy, i. The current flow can be in both directions: 1) from the emitter to the collector with a positive sign, and 2) from the collector to the emitter, with a negative sign. Note that the occupation factor $\left(f_E^i - f_C^i\right)$ can be formed into $f_E^i \left(1-f_C^i\right) - f_C^i \left(1-f_C^i\right)$ which indicates the transport direction more clearly.

Starting from these general high temperature expressions, we can now consider the limit of zero temperature, where the thermally activated number of phonons is zero, $N=0$, and high bias with $f_E^i = 1$, $f_C^i = 0$, and $f_C^r = 0$. Upon substitution of these parameters into

Eqs. (3.3) and (3.5) we obtain for the occupation of the resonance and the inelastic current contribution at the phonon peak bias

$$f^r \quad = \quad \frac{g\Gamma_E^i}{g\Gamma_E^i + \Gamma_C^r} \ , \tag{3.6}$$

$$I_{inelast} \quad = \quad \frac{2e}{\hbar} \frac{g\Gamma_E^i \Gamma_C^r}{g\Gamma_E^i + \Gamma_C^r} \ , \tag{3.7}$$

which correspond to the equations at phonon peak bias in Figure 3.1b.

The current contribution for the main-peak can be calculated in a very similar rate equation model, not involving any electron-phonon interaction and is left out here for brevity. It can be found in some detail in ref. [77]. Reference [77] derives the rate equation approach above more formally on a one-dimensional tight-binding lattice including the electron phonon interaction on the central site. The basic physics is well described in Figure 3.3, however, and we do not include the formal tight binding notation here for brevity. In the next section we give the derivation for Eqs. (3.3) and (3.5) in the KKB formalism, which we discuss in detail in Chapter 2 and Appendix A.

3.3   KKB Formalism Solution

3.3.1   Discretization Scheme for the Analytical Calculation

We have stated in Chapter 2 already that we solved numerically in one dimension the equation

$$I(z, E) = \frac{2e}{h} \int dz' \, T(z, z'; E) \ \ (f(z, E) - f_\tau(z', E)) \ . \tag{3.8}$$

We now would like to simplify this extended coordinate equation to only three spatial coordinates: emitter, well, and collector. If can assume that the occupation factor, f, which is the central parameter in our problem, to be constant in these device regions, under two conditions: the occupation, f 1) does not vary significantly within the three regions emitter,well, and collector, and 2) varies sharply in the barriers between these regions. We can then discretize the extended spatial problem into three spatial nodes: emitter, well, and collector, as depicted in Fig. 3.4.

The transmission coefficients $T(z, z'; E)$ occurring in the transport Eq. (3.8) are then to be discretized according to

$$T_{EC}(E) = \int_{z \in E} dz \int_{z' \in C} dz' \, T(z, z'; E) \ , \tag{3.9}$$

and similarly T_{EW}, T_{CW}, and T_{WW}. With the discretization we can obtain for the current per unit energy in the emitter

$$I_E = \frac{2e}{h} \left(T_{EC} \ (f_E - f_C) + T_{EW} \ (f_E - f_W^\tau)\right) \ . \tag{3.10}$$
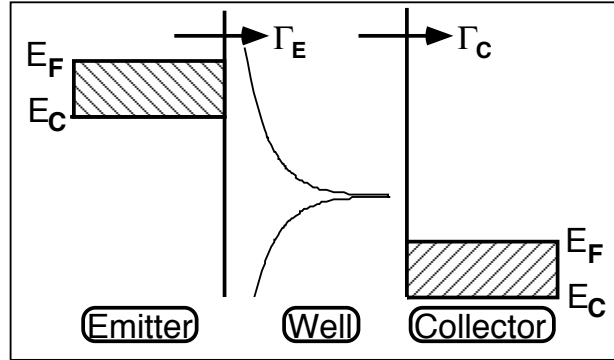
Figure 3.4 Set-up for the discretization scheme.

The current I_W is zero in the well and the equivalent equation to Eq. (3.10) in the well can be solved for the occupation in the well

$$f_W = \frac{T_{EW}\ f_E + T_{CW}\ f_C + T_{WW}\ f_W^\tau}{T_{EW} + T_{CW} + T_{WW}}\ . \tag{3.11}$$

If we restrict our view now to only two energy levels separated by one optical phonon energy, we can visualize Eqs. (3.10) and (3.11) with Fig. 3.5.
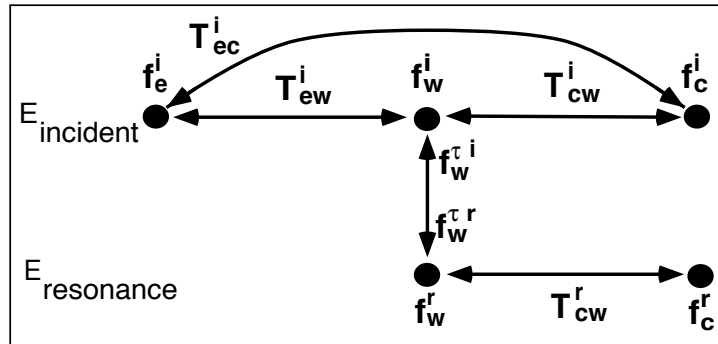
Figure 3.5 Two channels at incident and resonant energy are coupled by electron-phonon interaction. Note that there is no transmission from the resonance energy back into the emitter. Coupling of the two energies is controlled by the effective occupation, f^τ. The superscripts, i and r, stand for incident and resonance energy, respectively.

We can now see more explicitly the coupling between the two energies, if we only consider electron-optical-phonon interactions. Fig. 3.5 shows the coherent transmission path via T_{EC} and the sequential transmission path via $T_{EW}^i \to T_{CW}^r$.

3.3.2 Discretized Transmission Coefficients and Spectral Function

In order to actually evaluate the transport equation (3.10) we need to calculate the transmission coefficients T_{EC} etc. We have done this in two ways in Ref. [76]. We first calculated the transmission coefficients through a step-like double barrier structure in a continuous coordinate representation. The second approach is a calculation based on a tight-binding chain. We summarize the results here by stating the formulas relating the transmission coefficients to the spectral function in the well and the transmission rates through single barriers

$$T_{EC} = \frac{\Gamma_E \, \Gamma_C}{\Gamma} \, A \, , \tag{3.12a}$$

$$T_{EW} = \frac{\Gamma_E \, \frac{\hbar}{\tau_\Phi}}{\Gamma} \, A \, , \tag{3.12b}$$

$$T_{CW} = \frac{\Gamma_C \, \frac{\hbar}{\tau_\Phi}}{\Gamma} \, A \, , \tag{3.12c}$$

$$T_{WW} + T_{CW} + T_{EW} = \frac{\hbar}{\tau_\Phi} \, A \, , \tag{3.12d}$$

with $\Gamma = \Gamma_E + \Gamma_C + \frac{\hbar}{\tau_\Phi}$, $\frac{\hbar}{\tau_\Phi} = \frac{\hbar}{\tau_p} + \frac{\hbar}{\tau_n}$, and $\Gamma_{E(C)} = \hbar\nu \, T_{E(C)}$, where $\nu = \frac{v}{2d}$ is the attempt frequency in the well depending on the velocity in the well, v, and the well width, d. The spectral function in the well can be found to be

$$A(E) = \frac{\Gamma}{4 \, (\hbar\nu)^2 \, sin^2\left(\frac{\theta}{2}\right) + \frac{1}{4}\Gamma^2} \, , \tag{3.13}$$

in the continuous coordinate representation where $\theta = \Phi_E + \Phi_C + 2kd$ is the total round trip phase shift including the phase shifts due to reflection at the boundaries, Φ_E and Φ_C. We also evaluated the spectral function, A, in a tight binding model and obtained

$$A(E) = \frac{\Gamma}{(E - E_r)^2 + \frac{1}{4}\Gamma^2} \, . \tag{3.14}$$

The scattering rates, $\frac{1}{\tau_n}$ and $\frac{1}{\tau_p}$, which are necessary to evaluate the effective occupation, f_τ, in the transport Eq. (3.10), can now be calculated using the local density of states in the well, $N_0 = \frac{1}{2\pi} A$, and Eq (2.6). The phonon peak problem can now be solved analytically.

3.3.3 Analytical Solution of the Phonon Peak Problem

In this section we will show a derivation of the resonance occupation and inelastic current at the phonon peak bias including optical phonons that have some spectral spread, Δ, similar to the treatment that is included in our simulator QUEST.[56] This assumption does not have to made to obtain the correct expressions, however, we include this particular derivation here to connect up to the treatment in QUEST[56] with an analytical example.

Substituting Eqs. (3.12) into Eq. (3.11) we obtain for the occupations in the well at the incident and resonance energy

$$f_e^i = \frac{\Gamma_E^i f_E^i + \Gamma_C^i f_C^i + \frac{\hbar}{\tau_p^i}}{\Gamma_E^i + \Gamma_C^i + \frac{\hbar}{\tau_p^i} + \frac{\hbar}{\tau_n^i}} \ , \tag{3.15a}$$

$$f_e^r = \frac{\Gamma_C^r f_C^r + \frac{\hbar}{\tau_p^r}}{\Gamma_C^r + \frac{\hbar}{\tau_p^r} + \frac{\hbar}{\tau_n^r}} \ . \tag{3.15b}$$

To include a finite spectral spread in the optical phonon dispersion we modify Eqs. (A.29) in Appendix A.1 to include a spectral average over the rectangular line shape of width Δ to

$$\begin{aligned}
\frac{\hbar}{\tau_p(\vec{r};E)} &= \frac{1}{\Delta} \int_{E-\Delta/2}^{E+\Delta/2} dE' \, 2\pi U^2 \, \left\{ (N+1) \ N_0(\vec{r}, E'-\hbar\omega_0) \ (1-f(\vec{r}, E'-\hbar\omega_0)) \right. \\
&\qquad \left. + \ N \ N_0(\vec{r}, E'+\hbar\omega_0) \ (1-f(\vec{r}, E'+\hbar\omega_0)) \right\} , \tag{3.16a}
\end{aligned}$$

$$\begin{aligned}
\frac{\hbar}{\tau_n(\vec{r};E)} &= \frac{1}{\Delta} \int_{E-\Delta/2}^{E+\Delta/2} dE' \, 2\pi U^2 \, \left\{ (N+1) \ N_0(\vec{r}, E'+\hbar\omega_0) \ f(\vec{r}, E'+\hbar\omega_0) \right. \\
&\qquad \left. + \ N \ N_0(\vec{r}, E'-\hbar\omega_0) \ f(\vec{r}, E'-\hbar\omega_0) \right\} . \tag{3.16b}
\end{aligned}$$

We can now evaluate the set of Eqs. (3.16) for the incident (index i) and resonant (index r) energy, neglecting contributions at other energies. We assume that the occupation factors, f, are constant in these energy ranges. Using

$$\int_{E^r-\Delta/2}^{E^r+\Delta/2} dE' N_0(E') \approx 1 \ , \tag{3.17a}$$

$$\int_{E^i-\Delta/2}^{E^i+\Delta/2} dE' N_0(E') \approx N_0^i \ \Delta \ , \tag{3.17b}$$

we obtain four equations for the electron and hole-out-scattering rates at two different energies.

$$\frac{\hbar}{\tau_n^i} = \frac{2\pi U^2}{\Delta} \, (N+1) \, (1-f_W^r) \ , \tag{3.18a}$$

$$\frac{\hbar}{\tau_p^i} = \frac{2\pi U^2}{\Delta} N f_W^r \ , \tag{3.18b}$$

$$\frac{\hbar}{\tau_n^r} \;=\; 2\pi U^2 N N_0^i \left(1 - f_W^i\right) \;, \tag{3.18c}$$

$$\frac{\hbar}{\tau_p^r} \;=\; 2\pi U^2 \left(N+1\right) N_0^i f_W^i \;. \tag{3.18d}$$

We now use the relation $N_0(E) = A(E)/2\pi$ between the spectral function and the density of states, and we assume that $\hbar\omega_0 \gg \Gamma^i$ in Eq. (3.14). We define the phonon coupling constant, g, in terms of the constant U^2 and the optical phonon energy, $\hbar\omega_0$

$$g = \frac{2\pi U^2}{\Gamma^i} = U^2 \frac{A^i}{\Gamma^i} \approx \frac{U^2}{\left(\hbar\omega_0\right)} \;. \tag{3.19}$$

Upon substitution of Eqs. (3.15) into Eqs. (3.18) and using $\Gamma^i = \Gamma_E^i + \Gamma_C^i + \frac{\hbar}{\tau_p^i} + \frac{\hbar}{\tau_n^i}$ we obtain four coupled equations for the four scattering rates

$$\frac{\hbar}{\tau_n^i} \;=\; \frac{2\pi\hbar\omega_0}{\Delta} g \left(N+1\right) \frac{\Gamma_C^r \left(1 - f_C^r\right) + \frac{\hbar}{\tau_n^r}}{\Gamma_C^r + \frac{\hbar}{\tau_p^r} + \frac{\hbar}{\tau_n^r}} \;, \tag{3.20a}$$

$$\frac{\hbar}{\tau_p^i} \;=\; \frac{2\pi\hbar\omega_0}{\Delta} g \left(N+1\right) \frac{\Gamma_C^r f_C^r + \frac{\hbar}{\tau_p^r}}{\Gamma_C^r + \frac{\hbar}{\tau_p^r} + \frac{\hbar}{\tau_n^r}} \;, \tag{3.20b}$$

$$\frac{\hbar}{\tau_n^r} \;=\; gN \left\{ \Gamma_E^i \left(1 - f_E^i\right) + \Gamma_C^i \left(1 - f_C^i\right) + \frac{\hbar}{\tau_n^i} \right\} \;, \tag{3.20c}$$

$$\frac{\hbar}{\tau_p^r} \;=\; g \left(N+1\right) \left\{ \Gamma_E^i f_E^i + \Gamma_C^i f_C^i + \frac{\hbar}{\tau_p^i} \right\} \;. \tag{3.20d}$$

These four scattering rates can be solved for with an analytical software package like MAPLE or MATHEMATICA. Substitution of these rates into Eq. (3.15b) results in Eq. (3.3). The incoherent current contribution $\frac{2e}{\hbar} T_{EW} \left(f_E - f_W^\tau\right)$ in Eq. (3.10) must be integrated in energy over the width of the inelastic channel, Δ, to obtain Eq. (3.5).

3.4   Why bother about the KKB formalism?

We have shown in the previous two Sections 3.2 and 3.3 that two very different approaches lead to identical central results of the phonon-peak problem. We need to ask ourselves, why they give the same results, and why we should be still interested in the much more complicated KKB formalism. One difference between the two treatments is that the coupling to the leads is treated exactly in the KKB formalism, while the coupling to leads is treated in first order perturbation theory in the rate equation approach. Since the coupling of the central resonance is weak in this problem, we find that a treatment of tunneling to first order perturbation sufficient. Another difference between the two approaches is the treatment of the scattering. *Both* approaches are only valid for weak scattering and treat the scattering in first order perturbation theory. However, the KKB formalism treats the scattering in

the self-consistent first Born-approximation,[97] which results in a spreading of the resonance state due to the electron-phonon interaction. The two approaches give the same results in the phonon-peak problem because the optical phonon energy, $\hbar\omega_0$, is much larger than the resonance width in the quantum well, $\Gamma_E + \Gamma_C + \frac{1}{\tau_\Phi}$. The renormalization of the density of states due to scattering in the KKB formalism is much smaller than this energy scale and therefore not important.

The treatment of acoustic phonon scattering in a device where the phonon energy may be comparable to the natural line-width of the resonance state would have a strong influence on the line shape of the density of states, $N_0(E)$. A treatment using a pure rate equation approach would not include the spreading of the density of states due to the electron-phonon interaction and the results would become quite different from the KKB results. The device simulator QUEST[56] is based on a continuous coordinate representation of the device structure and allows to estimate the energetic spread of quantum resonances including electron-phonon interactions and may prove to be useful design tool in this respect.

3.5   Comparison between Numerical and Analytical Results

We have already introduced our numerical experiment regarding the phonon peak strength in asymmetric DBRTD's in Section 2.3. For convenience we include Fig. 2.4 again at this point as Figure 3.6. The surprising result of this simulation was the constance of the phonon
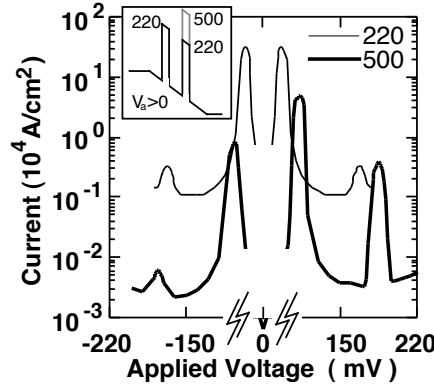
Figure 3.6   I–V–characteristic calculated for two different structures (see inset). Phonon-peak in forward bias remains unchanged and changes drastically in reverse bias.

peak in forward bias regardless of the collector barrier height.

From Eq. (3.7) we can see that there is a range of parameters where $g\Gamma_E^i \ll \Gamma_C^r$ which leaves the current at the phonon peak independent of the collector barrier height $I \simeq \frac{2e}{\hbar} g\Gamma_E^i$. This parameter range also corresponds to a negligible filling of the resonance as argued in Section 3.1. We have summarized the major results of Ref. [76] with respect to the numerical experiment in Figure 3.7 and the analytical expressions in Figure 3.1.

Fig. 3.7a shows the dependence of the phonon peak and the main peak at their corresponding biases. The phonon peak is clearly independent of the collector transmission

for a wide range of parameters, whereas the main peak shows a strong dependence. In forward and reverse bias we will have two different ratios of Γ_E/Γ_C since emitter and collector are inverted. If we now read off the difference in main and phonon peak current at
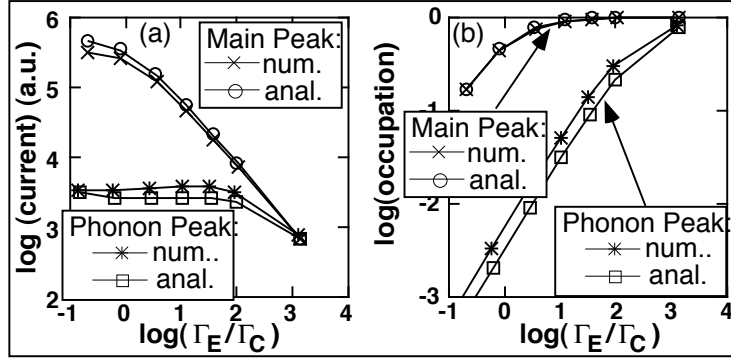
Figure 3.7   Comparison of numerical and analytical results. (a) The magnitude of the current, and (b) the occupation of the well, at the bias corresponding to the main peak current and the bias corresponding to the phonon peak current. The data points correspond to collector barrier heights (see inset of Fig. 3.6) of $V_C \in \{220, 300, 400, 500, 600, 700, 1000\} meV$ with an emitter barrier height of $220 meV$.

$log(\Gamma_E/\Gamma_C) = 1$ and -1 we see that forward and reverse bias result in different ratios of the phonon peak to the main peak.

Fig. 3.7b shows the occupation of the resonances at the phonon peak and the main peak biases. Clearly much more asymmetry is needed to fill up the resonance at phonon peak bias than at main peak bias.

In Fig. 3.8 we show the scattering times and escape times to the collector from the resonance involved in our numerical experiments. The scattering times at incident and
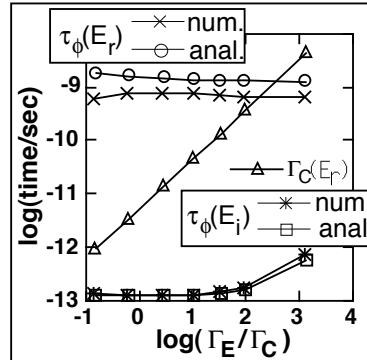
Figure 3.8   Self-consistent calculation of scattering times. Numerical and analytical results for the phase-breaking times at incident and resonance energy, $\tau_\Phi(E_i)$ and $\tau_\Phi(E_r)$, are compared to the collector leakage time, $\frac{1}{\Gamma_C(E_r)}$. When the collector leakage time becomes larger than the in-scattering time at the resonance energy, the resonance fills up and the out-scattering time at the incident increases.

resonant energy are clearly shown to be different due to the large difference in the density of states at resonance and off-resonance (see Fig. 3.4). Once the escape time through the collector from the resonance becomes comparable to the in-scattering time at resonance, the resonance starts to fill up and the scattering time at the incident energy becomes increased (scattering is reduced). Figs. 3.7 and 3.8 show a good agreement of our extended numerical calculation with the analytical model and indicate the interplay between the filling of the resonance and the scattering time. This dependence of the scattering rate on the filling of the resonance is also documented in a simple example in Appendix B.

3.6   Conclusions

We have modelled analytically the phonon peak problem in DBRTD's and obtain an intuitive physical picture. We are able to identify device regimes in which the off-resonant phonon peak current can be as big as the main resonant current as observed by Turley.[51]

The analytical results compare well to the numerical approach using the simulator QUEST. This agreement provides a good check for the analytical results, which are much easier and less time consuming to evaluate numerically. The available computation time may now be used to include more sophisticated scattering mechanisms as suggested in Chapter 7.

Chapter 4

Limitations of the Single-Particle Picture

QUEST can simulate electron-electron charging with a local Hartree-like potential in a single-particle framework, which describes the bistability in large cross section DBRTD's properly. We will show now in a simple analytic example, that this usage of an "effective" potential due to surrounding electrons cannot explain the phenomenon of Coulomb blockade. We will here consider a model problem where a *single* resonant state is charged up due to strong coupling to one lead and very weak coupling to the other lead in a double barrier structure. This model corresponds to a very asymmetric structure (see Fig. 4.1a) where we may assume the resonant state always to be filled by the strongly coupled lead. We assume that the tunneling to the weakly coupled lead is negligible and we are therefore left with a capacitor problem, where a single resonance is fed from one lead (Fig. 4.1b).
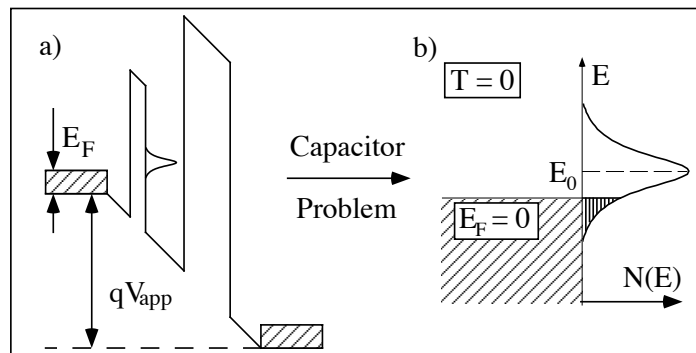
Figure 4.1 Set-up for the calculation of the charging of a single leaky resonance. a) Potential profile of a asymmetric double barrier resonance diode. b) Model capacitor problem of charging a finite width resonance.

We assume the resonance to be described by a normalized Lorentzian density of states

$$N(E) = \frac{\frac{1}{\pi \Gamma}}{1 + \left(\frac{E - E_0}{\Gamma}\right)^2} \; , \tag{4.1}$$

where Γ is the half width at half maximum and E_0 the resonance energy. We will assume zero temperature in our calculation, which will result in a sharp cut-off in the filling of the lead and resonance state.

If we neglect charging effects, we may write down a linear dependence between the applied bias and the resonance energy

$$E_0^0 = q\gamma \left(V_{th} - V_{app}\right) \; , \tag{4.2}$$

where we assume that the emitter lead is fixed in energy and an applied bias pulls the resonance down into the well. The threshold voltage, V_{th}, is the necessary applied voltage to place the center of the resonance right on the Fermi-level, which is set to be at zero energy. The geometry dependent constant, γ, determines the fractional voltage drop across the left barrier and q is the elemental electronic charge. Assuming that the Fermi sea is very wide compared to the width of the resonance, we calculate the filling of the resonance as

$$n(E_0) = \int_{-\infty}^{0} N(E) \, dE = \int_{-\infty}^{0} \frac{\frac{1}{\pi \Gamma}}{1 + \left(\frac{E - E_0}{\Gamma}\right)^2} dE = \frac{1}{2} + \frac{1}{\pi} \arctan\left(-\frac{E_0}{\Gamma}\right) \; . \tag{4.3}$$

Using Eqs. (4.2) and (4.3) with $E_0 = E_0^0$ we obtain the filling as a function of applied bias

$$n(V_{app}) = \frac{1}{2} + \frac{1}{\pi} \arctan\left(-\frac{\gamma q}{\Gamma} \left(V_{th} - V_{app}\right)\right) \; . \tag{4.4}$$

Results of Eq. (4.4) are plotted in Fig. 4.2a for various resonance widths, Γ, with $V_{th} = 0$, $\gamma = 1/2$. We see the expected result: the sharper the resonance, the sharper the turn-on of the charge accumulation in the well. The differential change of charge with applied bias can be calculated as

$$\left.\frac{dn}{dV_{app}}\right|_{E_0 = 0} = \left.\frac{q\gamma}{\pi\Gamma} \frac{1}{1 + \left(\frac{E_0}{\Gamma}\right)^2}\right|_{E_0 = 0} = \frac{q\gamma}{\pi} \frac{1}{\Gamma} \xrightarrow{\Gamma \to 0} \infty \; . \tag{4.5}$$

For an infinitesimally small resonance width, we obtain an infinitely sharp (step-wise) turn-on of the number of electrons in the quantum dot.

Given the filling of the resonance we may now associate a Hartree-like potential due to the accumulated charge

$$\delta V(E_0) = -\frac{q \, n(E_0)}{C} \; . \tag{4.6}$$

The accumulation of negative charge in the well will now raise the potential in the well and push the resonance higher. We therefore write down a new equation for the resonance energy, E_0

$$E_0 = q\gamma(V_{th} - V_{app}) - \alpha \, \delta V(E_0) \ , \tag{4.7}$$

where α is a unit-less geometry dependent constant of order 1. We therefore obtain (using Eqs. 4.4 and 4.6) an implicit equation for the resonance energy, E_0, of the form

$$E_0 = q\gamma(V_{th} - V_{app}) + \frac{\alpha q}{C}\left(\frac{1}{2} + \frac{1}{\pi}\arctan\left(-\frac{E_0}{\Gamma}\right)\right) \quad . \tag{4.8}$$
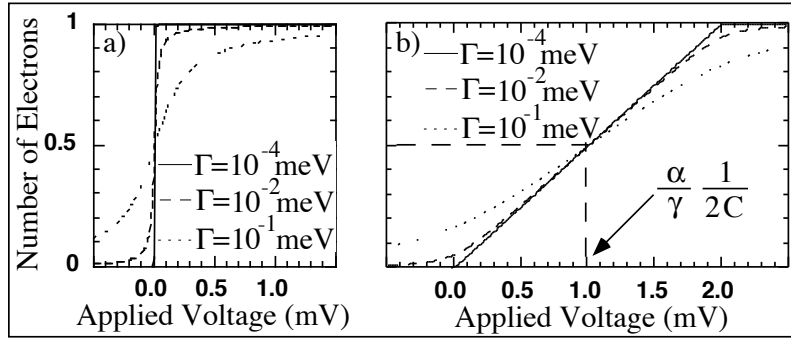
Figure 4.2 Number of electrons in the resonance versus applied bias. The parameters are $V_{th} = 0$, $\gamma = 1/2$: a) without charging. b) with charging, $\alpha = 1$, $\alpha q/C = 1 meV$.

Before we solve for the electron density, $n(V_{app})$, with a given set of parameters $\alpha q/C$, Γ, γ, and V_{th} numerically, we ask ourselves the question under which bias condition the resonance is exactly *half filled* in the interacting picture. Eq. (4.8) can be solved for the necessary applied voltage, V_{app}, exactly

$$V_{app}|_{E_0=0} = V'_{th} = V_{th} + \frac{\alpha}{\gamma}\frac{1}{2C} \quad . \tag{4.9}$$

The threshold to obtain half filling of the resonance is raised from V_{th} by $\frac{\alpha}{\gamma}\frac{1}{2C}$.

The questions that are naturally raised now are:
• Is the shift in threshold voltage a signature of Coulomb blockade ?
• Do we still get a sharp turn-on of charge accumulation in the well, that is merely shifted by the charging energy ?

The sharpness of the turn-on can be analyzed by examining the slope of the electron density, n, versus the applied bias, V_{app}, which can be calculated analytically to be:

$$\frac{dn}{dV_{app}} = -\frac{1}{\pi\Gamma}\frac{1}{1 + \left(\frac{E_0}{\Gamma}\right)^2}\frac{dE_0}{dV_{app}} = \frac{q\gamma}{\pi\Gamma\left(1 + \left(\frac{E_0}{\Gamma}\right)^2\right) + \frac{\alpha q}{C}} \quad , \tag{4.10}$$

where we have *at half filling* $(E_0 = 0)$

$$\frac{dn}{dV_{app}}\bigg|_{E_0=0} = \frac{\gamma q}{\pi\Gamma + \frac{\alpha q}{C}} \xrightarrow{\Gamma\to 0} \frac{\gamma}{\alpha}C \ . \tag{4.11}$$

It is crucial to see here that the *slope becomes finite* even for infinitesimally small resonance widths! In Fig. 4.2b we present a numerical evaluation of $n(V_{app})$ for several resonance widths, Γ, and $V_{th} = 0$, $\gamma = 1/2$, $\alpha = 1$, and $\alpha/C = 1mV$. The charging of the resonance clearly *stretches out the voltage axis* in comparison to Fig. 4.2a.

If we now consider the very weak coupling of the resonance to the collector as indicated in Fig. 4.1 the total current through the structure may be assumed to be proportional to the accumulated charge in the well and the tunnel rate through the right barrier

$$I(V_{app}) = qn(V_{app})\,\Gamma_{right} \ . \tag{4.12}$$

Since the current is now directly proportional to the accumulated charge in the well we can think of Figs. 4.2a and 4.2b as plots of current versus applied bias. Again we can see that turning on an "effective" Hartree potential interaction in the well based on a relative filling of the resonance state, stretches out the voltage axis in the current turn-on region and it therefore *converts the current steps into ramps.*

Single-electron tunneling and single-electron charging effects have been observed for small cross-section DBRTD's.[24–29] The filling of a particular state by *a single* electron in a quantum box of small size may change the spectrum of the other available states in the box significantly[34] and prohibit other electrons from tunnelling into the box (Coulomb Blockade[69–72]). The single-electron Coulomb interaction may also give rise to a spin splitting of the resonance levels.[25,73] Experimental I–V–characteristics exhibit a step-like structure (Coulomb Staircase) determined by the states in the device and not a ramp-like structure.

We therefore conclude here that calculating a Hartree potential from a partially filled, finite width resonance cannot explain the phenomenon of Coulomb blockade! We attribute this failure to the existence of fractional numbers of electrons in the quantum well due to our time average point of view. Given weak coupling to the leads, an electron either is, or is not in the quantum dot and the energy necessary to add an electron into the quantum dot is fixed. An average electro-static potential based on an average filling of the resonance, does not contain information about the necessary energy to add an electron into the quantum dot. Chapter 5 treats Coulomb charge correlation between electrons on a many-body footing where the occupation of each possible electron configuration is calculated and it presents a proper modelling of the Coulomb staircase. Chapter 6 treats the effects of Coulomb charge correlation for a system of coupled quantum dots.

Chapter 5

Strongly Correlated Transport: High Bias

5.1 Introduction

Large cross section double barrier resonant tunneling diodes (DBRTD's) have been extensively[1-5] studied and the quantization of the single-particle electronic state in the film growth direction has been shown to be crucial in the understanding of this quantum device. Charge accumulation[46,47,55,66] and inelastic scattering[43,46-55] have also been shown to modify the device behavior significantly. These interactions have been successfully treated with effective potentials in a single-particle picture.

In small cross section resonant tunneling diodes electrons are confined in all three dimensions. This confinement of few electrons in all three dimensions has a two-fold consequence: 1) the single-electron spectrum will be discrete, and 2) the usual effective potential treatment of electron-electron interactions becomes invalid and it is necessary to go beyond the single-particle picture in order to account for electronic correlations. Single-electron correlations effects are observable[24-27] in very asymmetric structures in a bias direction where the collector barrier is thicker and/or higher than the emitter barrier. This configuration corresponds to the one in which intrinsic bistability due to charge accumulation has been observed in large cross section DBRTD's.[46,47,55] There is no charge accumulation at all in the other bias direction,[24] and a very rich resonance spectrum can be observed. Nominally symmetric quantum dots (emitter and collector barrier heights are equal in flatband condition) are expected to have little charge accumulation in either bias direction because the applied bias effectively lowers the collector barrier height relative to the emitter barrier height and the rate of out-flow to the collector is larger than the rate of in-flow into the quantum dot from the emitter. The transport is expected to be mostly determined by the single-particle states and indeed a rich spectrum of resonance energies has been found experimentally.[28-32]

Beenakker[70] and Averin[69] have put forward similar rate equation models that include single-electron charge correlation and 0-D-states in the quantum dot. Their two approaches

---

differ only in the treatment of inelastic scattering in the quantum dot. Two extreme limits are treated: 1) no inelastic scattering,[70] and 2) strong inelastic scattering.[69,70] The inelastic scattering rate, $1/\tau$, needs to be compared to the tunneling rates through the barriers, which may vary from 10^9 to 10^{13} $1/s$ depending on the height and thickness of the barriers. Estimates of electron-phonon scattering rates in quantum dots have been estimated[127] to vary over the same wide range of values.

High bias current-voltage characteristics have only been calculated by Averin in the model of very strong inelastic scattering.[69] With a thorough analysis of the differences between the limits of $1/\tau = 0$ and $1/\tau \gg \Gamma^{L(R)}$ and the introduction of a finite τ, we will try to shed light on the effects of fast and slow electron phonon interaction in the quantum dots on the high bias I–V–characteristic.

Lateral confinement does not only alter the single-particle electronic states of the quantum dot, but also quantizes the contact states into waveguide-like subbands. The lateral confinement is determined by the charge depletion width at the lateral boundaries. The charge depletion, and hence, the lateral confinement, and the lateral energy quantization change with the changing doping level along the growth axis of the structure. The role of the transverse subbands in the leads on high bias transport has been analyzed theoretically for symmetric quantum dots using the assumption of negligible charge accumulation with a single-particle transmission coefficient approach.[32,128–131] It has been found by comparison to experimental results[30,132,133] that effects due to subbands in the emitter leading to the quantum dot are significant in high bias I–V–characteristics. In particular it was shown that non-adiabatic transport processes which couple lead subbands to quantum dot states of different lateral quantum numbers, cause additional resonance features in the valley current region.[128–130,132]

The treatments including single-electron charging, and elastic and inelastic scattering[69,70] do not consider effects due to subband mixing. The treatments of subband mixing[128–130] do not include single-electron charging and inelastic scattering. With this work we extend Beenakker's[70] many-body rate equation approach to include non-adiabatic coupling to discrete subbands in the leads and finite lifetime inelastic scattering in the quantum, and we address the following questions:

1. Can coulomb charge correlation play a role in nominally symmetric structures? Why is there no experimental evidence of single electron charging effects in such structures?
2. Is subband mixing important in very asymmetric structures as well as in symmetric structures? One may argue that this may not be the case, since the thick collector barrier governs the transport through an asymmetric structure and modifications due to coupling at the emitter will be negligible.
3. How important is the inelastic scattering in high bias transport through quantum dots? Can high bias I–V–characteristics be used to indicate whether there is a slow or a fast electron relaxation in the dot?

We first present the many body rate equation approach and simplify it for the case of two states in the quantum dot. Using this simplification we present analytical examples that

illustrate separately the importance of electron charge correlation, inelastic scattering in the quantum dot, and discrete emitter subbands on the high bias current voltage characteristic. We also discuss analytically the competition of an enhanced current due to single-electron interactions against electron relaxation in the quantum dot on the I–V–staircase. Finally we include a more sophisticated model of subband mixing and evaluate numerically the transport properties through two different quantum dots, symmetric and asymmetric, and address the questions stated above.

5.2 The Rate-Equation Model

We are interested in modelling high bias transport through a central confined system with interacting electrons. The states in a quantum dot (see Fig. 5.1) may be a complicated superposition of single-electron states.[134–140] We are following Beenakker[70] in the modelling of high bias transport using rate-equations. The complicated many-body state in the quantum dot are coupled to adjacent leads via sequential single-electron tunneling. We construct the many-body spectrum using a constant charging energy. The limitations of this Ansatz are discussed in the Appendix. We denote the many-body states in a configuration space notation[70] of the form $\{n_i\} = \{n_1, n_2, n_3, \ldots\}$ where the elements n_j can take on values of 0 and 1 indicating the occupancy of a particular orbital. The complicated task in this problem is to solve for the non-equilibrium occupation probabilities of *all* many-body states in the quantum dot.
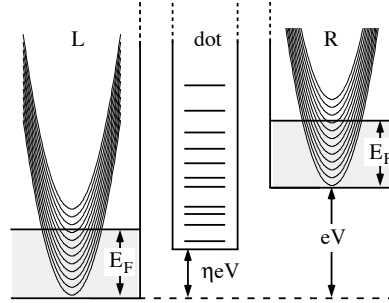
Figure 5.1 Conduction band profile of a quantum dot with applied bias. η is the fractional voltage drop over the left barrier. Quantum dot states are due to confinement in all three dimensions. Subbands in leads are due to lateral confinement.

To illustrate the rate-equation setup in the configuration space notation we consider a system of two single-particle states (Fig. 5.2). There are four possible configurations of electrons in the quantum dot: $\{0,0\}$, $\{1,0\}$, $\{0,1\}$ and $\{1,1\}$. The respective eigen-energies $E_{\{n_1,n_2\}}$ of these four states are 0, E_1, E_2 and E_1+E_2+U, where U indicates the modification of the eigen-energy due to electron-electron charge interaction. Figure 5.2a depicts the eigen-energy spectrum of the this simple many body system and its associated transition energies. The transitions between these many-body states are due to the tunneling to the adjacent leads as indicated in Figure 5.2b. The empty dot state $\{0,0\}$ in Fig. 5.2b, for example, is
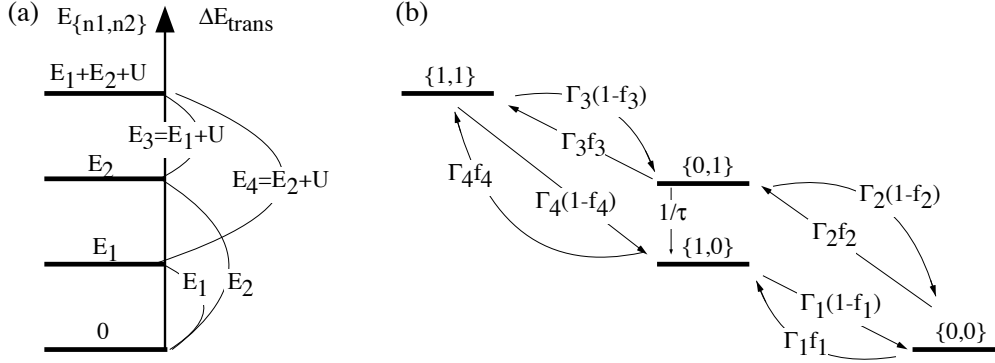
Figure 5.2 Interacting 2-particle system. (a) Eigen-energy spectrum and transition energies. (b) Configurations $\{n_1, n_2\}$ ordered vertically by their corresponding eigen-energy in (a). Coupling between configurations depends on transition rates, Γ, availability of initial (f), final ($1-f$) states and the necessary transition energy (subscripts 1...4). $1/\tau$ indicates the intra dot relaxation between configurations of constant number of particles.

coupled to the state $\{1,0\}$ via a transition through the left or the right barrier into state n_1 ($0,0 \to 1,0$). The rate $\Gamma_1 f_1$ of this transition is determined by the barrier properties and the coupling of the single-particle state E_1 to the lead subbands (Γ_1) and the condition that there is an electron available (f_1) with the necessary transition energy in the left or right lead. For legibility we have abbreviated this process to $\Gamma_1 f_1 = \Gamma_1^L f_1^L + \Gamma_1^R f_1^R$. The reverse process of $\{1,0\} \to \{0,0\}$ depends on the the tunneling rate, Γ_1, and the probability of finding an empty state in the leads, $(1-f)$. Using the same abbreviated notation as above we denote $\Gamma_1(1-f_1) = \Gamma_1^L(1-f_1^L) + \Gamma_1^R(1-f_1^R)$. All other transitions with changing numbers of electrons are similar, where we have indexed Γ's and f's by their appropriate transition energies E_1, E_2, $E_3 = E_1 + U$, and $E_4 = E_2 + U$. This picture described here is identical to the one used by Beenakker[70] to model linear response except for the inclusion of inelastic scattering.[75] We extend this model now to include a finite relaxation rate, $1/\tau$, connecting states of constant number of electrons in the quantum dot: $\{1,0\} \leftrightarrow \{0,1\}$ and solve it for high bias.

Each configuration $\{n_1, n_2\}$ has an associated steady state occupation probability, $P(\{n_i\})$, which is a function of the coupling to the leads and the quantum dot relaxation time. The equations that we solve do not provide more physical insight than Figure 5.2 and their discussion has been deferred to Appendix C.2. Effects due to non-adiabatic transport (subband mixing) enter our treatment via the tunneling rates, Γ, and the detailed discussion concerning the non-adiabatic coupling of lead subbands to quantum dot states is deferred to the next section.

Complexity of the Problem: The system of equations can be cast into matrix form and solved numerically. The solution of the rate equations becomes exponentially complex, since 2^p different occupation configurations exist for the maximum number of p single-particle states in the quantum dot, resulting in a set of 2^p coupled equations ($2^p \times 2^p$ matrix). The problem simplifies dramatically if the quantum dot is assumed to be close to or in local

equilibrium. Beenakker[70] has solved these coupled equations in the limit of linear response for the analysis of periodic conductance oscillations.

In high bias, however, the electron distribution is driven far away from its equilibrium value. Averin[69] has considered the case of rapid thermalization in the quantum dot, where the total number of electrons in the dot at high bias can be far away from its equilibrium value, however the electron distribution in the subset of constant number of electrons, N, is given by its equilibrium value. This assumption of rapid thermalization in the quantum dot simplifies the necessary calculations significantly since only the non-equilibrium *number* of electrons in the dot needs to be calculated. The problem reduces from 2^p to p unknowns. The rate equations for the non-equilibrium number of electrons in the quantum dot are given in Appendix C.3. We do not make this assumption of rapid thermalization and solve for the probability of relaxation of *all* configurations and therefore treat the problem more generally. We can show with our analytical results with finite relaxation time τ, how the limit of $\tau \to 0$ converges to the thermalization result by Averin. For the numerical treatment we only consider the two limiting cases of $1/\tau \gg \Gamma$ and $1/\tau = 0$.

In order to provide insight into the effects of the different interaction and transport processes (charging, inelastic scattering, and non-adiabatic subband mixing) we will first discuss in Section 5.3 a simplified model problem with two states, and then will present our numerical model and numerical results in Sections 5.4 and 5.5, respectively.

5.3   Analytical Results for a 2-State System

In this section we present our analytical results describing high bias transport through simple 2-state systems. The processes we discuss consider can be divided into two groups:
1) Electron-charge interactions and inelastic scattering are intra-quantum dot many-body properties.
2) Non-adiabatic transport due to subband mixing is determined by the coupling of the quantum dot to the adjacent leads.
We will divide up our analytical discussion along these lines and discuss intra-dot many-body effects in Section 5.3.1 first and then motivate effects due non-adiabatic transport in the following Section 5.3.2.

5.3.1   Coulomb Charge Interaction and Inelastic Scattering in the Quantum Dot

We now consider effects due to electron charge interaction and inelastic scattering in the quantum dot in the Gedankenexperiment depicted in Figure 5.3a and compare them to the simple single-particle result. We consider 3D to 0D adiabatic sequential tunneling through a system of two single-particle non-spin-degenerate transverse states. For the simplicity of this example we assume the 1D subbands in the leads to be infinitely closely spaced due to weak confinement in the leads. Like Averin,[69] we assume that lateral states in the quantum dot are only coupled to subbands in the leads with the same lateral quantum number.

Therefore every state in the quantum dot has only one corresponding subband in the lead and we only need to consider two lead subbands. The Fermi energy in the leads is assumed to be larger than the energy difference between the two single-particle states ($E_F > E_2 - E_1$). For simplicity we assume here that the coupling rates, Γ, are energy and state independent for energies above the emitter conduction band edge. The current expressions that we state in the next four sections are all derived in Appendix C.5.

Sequential Tunneling Through a Non-Interacting System

For a simple reference we repeat here the well known single-particle picture of high bias transport. Transitions from the emitter into the quantum dot will occur, if an electron in the emitter lead can provide the necessary transition energy. An electron with energy E_F at the Fermi-energy in the emitter will gain an energy αV ($\alpha = e(1-\eta)$, see Fig. 5.1) by hopping into the the dot due to the applied bias across the emitter barrier. $E_F + \alpha V$ is the maximum energy a single electron can provide for a transition. Given the two single-particle quantum states with two distinct excitation energies E_1 and E_2, we expect two distinct current turn-ons in the high bias I–V–Characteristic at biases of $\alpha V + E_F = E_1$ and $\alpha V + E_F = E_2$ (Fig.5.3a,b). Each of the independent channels carries a current of $I_{norm} = e\frac{\Gamma_L \Gamma_R}{\Gamma_L + \Gamma_R}$.

A bias of $\alpha V = E_1$ will pull state number 1 under the conduction band edge of the emitter turning off channel number 1 and leaving only channel number 2 conducting. Bias voltages beyond this point we will call "valley current" bias. The total current I_{norm} through the structure is carried by one channel until the second state is pulled under the emitter conduction band edge at a bias of ($\alpha V = E_2$). Figure 5.3b shows the expected I–V–characteristic with the current normalised by $I_{norm} = e\frac{\Gamma_L \Gamma_R}{\Gamma_L + \Gamma_R}$ for a symmetric ($\Gamma_R = \Gamma_L$) and asymmetric ($\Gamma_R = 50 \times \Gamma_L$) structure. The current response is the same for both structures due to the normalisation by I_{norm}

Relaxation Effects on the Valley Current

One well known mechanism which can enhance the valley current of the quantum dot is inelastic scattering. In Figure 5.3c we plot the expected I–V–characteristic in the 2-state case for inclusion of strong inelastic scattering ($\tau = 0$) in the quantum dot without any charge interaction. Comparing to Figure 5.3b we can see that the "valley-current" is increased for *both*, the symmetric and asymmetric structure. This region of valley-current is where the lowest single-particle state is pulled under the conduction band of the emitter (Fig. 5.3c). An electron that has tunnelled into the $\{0, 1\}$ configuration can, if it stays in the quantum dot long enough, relax into a $\{1, 0\}$ configuration (Fig. 5.2b). Electron relaxation opens up a new conduction channel at this bias and current is increased.

The analytic current expression for this bias region is quite lengthy and does not provide physical insight. However, the limiting cases for very small and very large scattering rates given $E_2 - E_1 \gg k_B T$, show nicely how the current in this voltage region is increased. For a long relaxation time, (small rate $1/\tau$), we obtain the single channel result increased by a
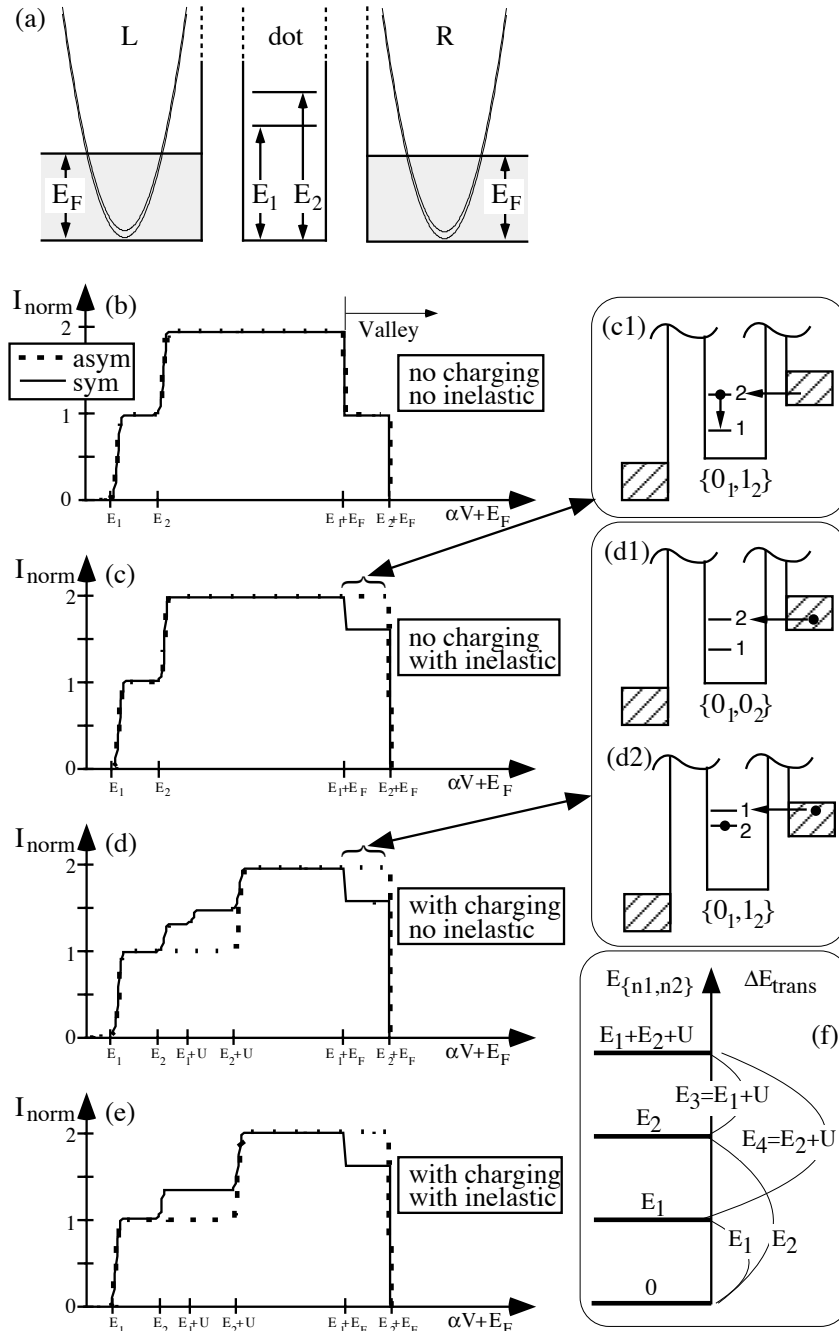
Figure 5.3 Analytic 2-state example. (a) conduction band set-up for 2 lateral non-degenerate states above the Fermi energies in the leads. (b)-(e) depict high bias I–V–characteristics for different models: (b) single-particle, non-interacting. (c) single-particle, inelastic scattering, (d) charge-interaction, no inelastic scattering, (e) charge-interaction and inelastic scattering. Inserts c1 and d1, d2 indicate the origin the enhanced valley current.

some small inelastic contribution

$$I = e\frac{\Gamma_L\Gamma_R}{\Gamma_L + \Gamma_R} + C\ \frac{1}{\tau}\ . \tag{5.1}$$

The result for the limit of strong inelastic scattering is

$$I = 2e\frac{\left(\Gamma_L + \Gamma_R\right)\Gamma_L\Gamma_R}{2\Gamma_L^2 + 2\Gamma_L\Gamma_R + \Gamma_R^2} - \tilde{C}\ \tau\ . \tag{5.2}$$

The expression is not intuitive, however, the limit $\Gamma_R \gg \Gamma_L$ at an infinite relaxation rate results in $I(\tau = 0) \overset{\Gamma_R \gg \Gamma_L}{\longrightarrow} 2e\frac{\Gamma_L\Gamma_R}{\Gamma_L+\Gamma_R} = 2I_{norm}$. This is the result for two channels through an asymmetric structure.

The well known conclusion of this subsection is that current flow can be significantly enhanced in the valley current region in the presence of intra-dot inelastic scattering. The increase in the current flow will depend on the particular relaxation rates between quantum states and rate of coupling into and out of the quantum dot.

Electron-Charge Interaction

Single charge interactions modify the single-particle transition energies of a quantum dot significantly (see Fig. 5.2a). The energy of a two electron state is raised by the charging energy, U. For simplicity we assume here the charging energy to be larger than the single-particle energy spacing, $U > E_2 - E_1$. Given four distinct transition energies (see Fig. 5.2a) E_1, E_2, $E_1 + U$, and $E_2 + U$ we expect four distinct channel turn-ons in the I–V–characteristic at biases of $\alpha V + E_F = E_1$, $\alpha V + E_F = E_2$, $\alpha V + E_F = E_1 + U$, and $\alpha V + E_F = E_2 + U$. Figure 5.3d shows the I–V–characteristics for a symmetric and asymmetric structure. The symmetric structure shows 4 characteristic turn-ons at the expected energies, however the asymmetric structure shows only two characteristic turn-ons. We will explain the difference in the rise-part of the I–V–characteristic of these two structures in Section 5.3.1.

In this section we will concentrate on one particular transition in the valley current region, where the first single-particle level, E_1, is pulled under the conduction band edge of the emitter (Fig. 5.3d). Configuration $\{0, 1\}$ effectively lifts single-electron level 1 *above* single-electron level 2 (the transition energy is $E_1 + U > E_2$) and another channel for conduction due to electron charge interaction is opened (Fig. 5.3d2). The availability of this channel depends on the filling of the quantum dot with electrons. An opaque collector barrier in an asymmetric structure causes charge to accumulate in the quantum dot and the valley current will be increased due to electron charge interactions (Fig 5.3d).

We can calculate an analytical expression (see Appendix C.5) for this case which indicates an enhanced current compared to the no-charging-interaction case. The analytical expression for this bias situation reads

$$I = 2e\frac{\left(\Gamma_L + \Gamma_R\right)\Gamma_L\Gamma_R}{2\Gamma_L^2 + 2\Gamma_L\Gamma_R + \Gamma_R^2} \overset{\Gamma_R \gg \Gamma_L}{\longrightarrow} 2e\frac{\Gamma_L\Gamma_R}{\Gamma_L + \Gamma_R} = 2I_{norm}\ \ . \tag{5.3}$$

In the limit of opaque collector barriers ($\Gamma_R \gg \Gamma_L$) we obtain the result of 2 independent channels that are opened by the electron-electron charge interaction. Figure 5.3d shows the enhanced current in the valley current region for an asymmetric and symmetric structure. with $\Gamma_R = 50\Gamma_L$ and $\Gamma_R = \Gamma_L$, respectively. Also indicated in this figure are the relevant transition energies. A full discussion on the rise part of the I–V–characteristic especially as to why there is no feature in the I–V–characteristic at E_2 and $E_1 + U$ for the asymmetric structure, will be given in Section 5.3.1.

We have assumed in the previous paragraphs that the charging energy is larger than the single-particle energy spacing, $U > E_2 - E_1$. If the charging energy, U, is less than the energy difference of the two single-particle states the turn-ons and turn-offs of particular transitions will be altered. The second channel, that has been opened by the single-electron charging, will be shut down at a corresponding bias of $\alpha V + E_F = E_1 + U$ which is less than $\alpha V + E_F = E_2 + E_F$ indicated in Figure 5.3d. This situation can be also visualised by a figure similar to Fig. 5.3d2 where the transition energy of the $\{0, 1\}$ state is not above the conduction band of the emitter.

Conclusion: The valley current of a multi-state quantum dot is enhanced due to single-electron charge interactions. The current is increased even in the limit of symmetric structures ($\Gamma_R = \Gamma_L$). Eq. 5.3 evaluated for $\Gamma_R = \Gamma_L = \Gamma$ results in $\frac{4}{5} e\Gamma$ compared to the single channel value of $e \frac{\Gamma_R \Gamma_L}{\Gamma_R + \Gamma_L}\big|_{\Gamma_R = \Gamma_L = \Gamma} = \frac{1}{2} e\Gamma$. The current does not quite double to two channels, but the single-particle charge interaction has increased the current flow by 60%.

Electron Charge Interaction and Relaxation Effects on the I–V–Staircase

In the previous Sections 5.3.1 and 5.3.1 we discussed electron charge interaction and electron relaxation independently of each other. We will now put both together and will discuss the current expressions for each of the relevant voltage regions in detail. Figure 5.3e shows the corresponding I–V–characteristic including electron charge interaction and very strong inelastic scattering. Note that the I–V–characteristic for the asymmetric structure appears to be unchanged compared to Figure 5.3d. However the symmetric structure looses one turn-on feature at $E1 + U$ due to the inclusion of strong inelastic scattering. We will now walk through the I–V–characteristic transition energy by transition energy and try to provide physical insight into the transport processes. We will explain how
1) single-electron charge interactions introduce new features in the I–V–Staircase at each transition energy, and
2) how inelastic scattering and structural asymmetry tend to wipe some features out.

E_1 Transition: In a bias range corresponding to $E_1 \leq \alpha V + E_F < E_2$ only the $\{0, 0\} \leftrightarrow \{1, 0\}$ transition is allowed. The current is transported through a single channel resulting in:

$$I_1 = e \frac{\Gamma_R \Gamma_L}{\Gamma_R + \Gamma_L} = I_{norm} \ . \tag{5.4}$$

E_2 Transition: Two transitions $\{0, 0\} \rightarrow \{1, 0\}$ and $\{0, 0\} \rightarrow \{0, 1\}$ are allowed to fill the empty dot from the right in a bias range $E_2 \leq \alpha V + E_F < E_1 + U$. Given the filling of the

dot with one electron, only one transition to the left (back to the $\{0,0\}$ state) is allowed. This corresponds to 2 entry channels from the right and 1 exit channel to the left and the current is[72]

$$I_2 = e\frac{2\Gamma_R \Gamma_L}{2\Gamma_R + \Gamma_L} = I_{3,\tau=0} \ . \tag{5.5}$$

This result is independent of the presence of inelastic scattering, since inelastic scattering does not modify the number of available entry and exit channels into and out of the quantum dot.

The current is suppressed from the no-charging result, $U = 0$, of $2I_{norm}$ due to single electron charge interaction, even in symmetric structures. The current is increased, however, from the single channel result I_1, in the previous voltage region by a fraction of $\frac{I_2-I_1}{I_1} = \frac{\Gamma_L}{2\Gamma_R+\Gamma_L}$. With increasing asymmetry of $\Gamma_R \gg \Gamma_L$ this additional current step is wiped out. Physically the equivalence of I_1 and I_2 in the of $\Gamma_R \gg \Gamma_L$ limit is determined by the number of channels through the most impeding barrier. The left barrier is the most impeding one here and the number of channels through it is one for both bias points.

$E_1 + U$ *Transition:* The $\{0,1\} \leftrightarrow \{1,1\}$ transition becomes available for biases in the range of $E_1 + U \leq \alpha V + E_F < E_2 + U$ and the state $\{1,1\}$ can only be achieved by this particular transition. This additional transition will increase the availability of channels of conduction through the quantum dot and the current can be calculated to be:

$$I_{3,1/\tau} = e\frac{\Gamma_L\Gamma_R}{\Gamma_L + \Gamma_R}\left(1 + \frac{\Gamma_L}{\Gamma_L + \Gamma_R}\right) - C\,\frac{1}{\tau} \tag{5.6}$$

in the limit of a small relaxation rate, $1/\tau$.

A finite relaxation rate reduces the current in this bias $(-C\frac{1}{\tau})$. A relaxation process $\{0,1\} \to \{1,0\}$ in the quantum dot decreases the population of the excited $\{0,1\}$ state, which is the initial state of the $\{0,1\} \to \{1,1\}$ transition, which in turn has increased the number of transport channels through the structure. The $\{0,1\}$ state will not be populated at all in the limit of very large relaxation rates where the tunneling into the dot from the right is slower than the relaxation in the dot. The additional transport channel is therefore shut down by the inelastic scattering in the dot and the current $(I_{3,\tau=0})$ remains the same as in the previous bias region where two entry channels and one exit channel were available (I_2 in Eq. (5.5)). Figure 5.3e shows how the additional current step is wiped out by the inclusion of inelastic scattering.

This additional step will also vanish in very asymmetric structures, where $\Gamma_R \gg \Gamma_L$, since the number of exit channels determines the current flow in this limit. We therefore have $I_1 \approx I_2 \approx I_3 \approx e\Gamma_L$ as shown in Figure 5.3d in the bias region $E_1 \leq \alpha V + E_F < E_2 + U$.

$E_2 + U$ *Transition:* Applied voltages corresponding to an transition energy range of $E_2 + U \leq \alpha V + E_F < E_1 + E_F$ allow for all four transitions depicted in Figure 5.2a to occur. This implies that each formerly single-particle level can now be filled independently of the filling of the other level. This corresponds to the availability of two independent conduction channels just as discussed in Section 5.3.1. The current through the structure is then again:

$$I_4 = 2e\,\frac{\Gamma_R\Gamma_L}{\Gamma_R + \Gamma_L} = 2I_{norm} \ . \tag{5.7}$$

This result is independent of the inclusion of inelastic scattering because inelastic scattering does not reduce the number of transport channels in this bias range.

Valley Current Region: The transport behavior in the valley current region of $E_1+E_F \leq \alpha V + E_F < E_2 + E_F$ has been discussed at length in Sections 5.3.1 and 5.3.1. The current expression in the presence of electron charge interaction for this voltage region does not depend explicitly on the relaxation rate in the quantum dot and is given by Eq. (5.3).

Conclusion: The conclusion we draw from this sub-section is that single-electron charge interactions can modify the high bias response even for symmetric structures and introduce new features. Single electron charge correlation modifies the transition energy spectrum of the quantum dot. These new transition energies allow for new transport channels into the quantum dot. However, if the overall transport is limited by the collector barrier, charge will accumulate and the number of entry channels into the quantum dot becomes irrelevant. Charge accumulation will therefore wipe out effects due to additional transport channels. Electron relaxation in the quantum dot tends to wipe out features that are due to filling of excited energy levels and couples lower lying levels that are elastically decoupled from the emitter.

5.3.2 Non-Adiabatic Transport – Effects of Quantized Emitter Subbands

So far we have assumed that every subband in the lead is only coupled to states in the quantum dot with the same lateral quantum number. The lateral confinement in the leads was assumed to be negligible, such that the subbands are almost degenerate (Fig. 5.3a). However, lateral confinement is clearly present in the leads as well as in the quantum dot. The lateral energy spectra in the leads and the quantum dot are only the same if the lateral confinement is the same in the regions and the assumption of adiabatic coupling of the lead subbands to the quantum dot states is only valid under this condition. This is the model Averin[69] has used. However, the electro-static transverse confining potential is generally position dependent, due to spatially depending doping, which causes subband mixing between the lead subbands and quantum dot states of different lateral quantum numbers. This can be thought of as confinement induced elastic scattering, which couples different lateral quantum numbers. This process introduces new features in the high bias I–V–characteristic.[128–130]

In the next sub-section we will only consider effects due to subband mixing. We will not include effects due to inelastic scattering or electron charge interaction. We consider a very simple 2-state example, where we motivate the expected effects due to subband mixing. The complete model proposed by Bryant[128–130] adapted for the use of rate equations will be explained in detail in Section 5.4.

We consider a model-system with 2 quantum states 1 and 2 with corresponding subbands a and b in the leads (see Fig. 5.4). We assume that the doping in the structure is such that only the *lowest* subband (a) is occupied with electrons. The treatment in the adiabatic limit allows only for coupling of states with the same lateral quantum numbers, i.e. only $a \leftrightarrow 1$ and $b \leftrightarrow 2$ transitions are allowed. Since subband b is not occupied with electrons, there will only be transport through state 1 indicated in Figure 5.4b.
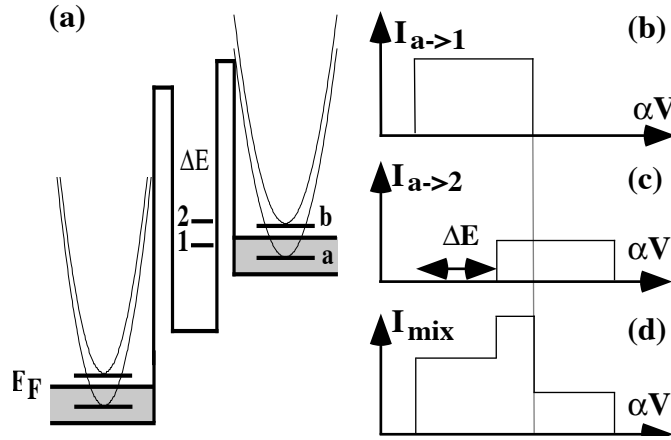
Figure 5.4 Adiabatic versus non-adiabatic transport. (a) Example conduction band profile with 2 non-degenerate, non-interacting lateral quantum levels. Energy splitting is ΔE. Only the lowest subband is occupied in the leads. (b) Current due to adiabatic transport through corresponding lateral states $a \rightarrow 1$. (c) Contribution due to coupling between different lateral quantum numbers $a \rightarrow 2$. (d) Sum of the two current contributions in (b) and (c) New features are introduced in the rise part of the I–V–characteristic and the valley current. Voltage region of current flow is extended.

Inhomogeneity in the lateral confinement will introduce some coupling between subband a and state 2. Figure 5.4c depicts the additional current contribution due to the $a \rightarrow 2$ transition. The magnitude of the current contribution is determined by the strength of the matrix element between subband a and state 2. The scattering matrix elements describing the coupling between all the states of the system needs to be unitary for reasons of current conservation. This implies that allowing for a $a \rightarrow 2$ transition with some particular amplitude, lowers the amplitude of the $a \rightarrow 1$ transition from its adiabatic value.

The $a \rightarrow 2$ transition will be offset from the $a \rightarrow 1$ transition by the energy $\Delta E = E_2 - E_1$. This has two consequences on the overall current through the structure:

1) New resonance phenomena are introduced on the rise part of the I–V–characteristic (Fig. 5.4d).

2) The bias region of current flow is increased and another mechanism for the generation of valley current has been introduced.

5.4   Numerical Approach

There are two key ingredients in the numerical evaluation of the rate equation model presented in Fig. 5.2, Section 5.2, extended to many quantum states: 1) the calculation of the coupling rates of the single-electron states in the quantum dot to the quantized emitter subbands, and 2) the numerically efficient setup of the rate equations. The second step is linked to the first one by the following argument. The subband mixing enters into the rate equation model via the coupling rates, Γ, into the quantum dot. The selection of states to obtain unitary subband mixing scattering matrices determines the number of quantum states that we consider in the quantum dot. After the selection of quantum states is done, we can consider their symmetry and simplify the problem to ease the numerical evaluation. In the next two sections we will pick up these two issues one by one.

5.4.1   Subband Mixing – The Model

We use the theory of multichannel quantum dot tunneling which was developed and employed previously by Bryant to study resonant tunneling through single dots with abrupt connections,[128–130] through dots with tapered connections,[130] and through coupled quantum dots.[141] We assume that the quantum dot nanostructure is a cylinder which is divided into separate regions for the emitter, the barrier between the emitter and the dot, the dot, the other barrier, and the collector. We assume that the lateral confinement potential in each region is parabolic. In each region the electron effective mass, lateral confinement potential, and the conduction band edge are locally constant. However, these parameters can change from region to region. To calculate the transmission coefficient for single barrier tunneling into (out of) the quantum dot, we propagate an electron incident from the emitter (collector) through the connection, across the barrier and into the dot. Wave function boundary conditions are satisfied at each interface between adjacent regions. Details are given in Refs. [128] and [130].

Mode-mixing is determined by how the lateral confinement potential changes where the leads connect to the dot. In previous work, Bryant considered abrupt connections[128–130, 141] in which the lateral confinement potential changes at the lead/barrier interfaces, and tapered connections,[130] in which the lateral confinement potential changes smoothly as the lead connects to the dot. Mode-mixing is qualitatively the same for both models. Here, we assume that the connections are abrupt to simplify the calculations. The overlaps

$$\langle l, m | r, q \rangle = \int dx \, dy \, \phi_{lm}^* \, \phi_{rq} \tag{5.8}$$

between lateral states, $\phi_{j,q}(x, y)$, on adjacent sides of an interface, $j = l$ (left) or $j = r$ (right), determine which lateral modes mix at an interface and how strong the mixing will be. If confinement is the same on both sides of the interface, then $\langle l, m | r, q \rangle = \delta_{m,q}$ and tunneling is a single-channel process. Lateral mode-mixing at the interface is possible, when the confinement is different in two adjacent regions.

When the quantum structure is cylindrically symmetric, as in a vertical quantum dot structure with parabolic confining potentials, the lateral modes in different regions can mix

only if the modes have the same lateral (x and y) parity. There are four independent sets of coupled channels (Fig. 5.5a) with even/even, odd/even, even/odd and odd/odd parity. We include the ground states $(0,0)$, $(1,0)$, $(0,1)$, and $(1,1)$ of each of these groups and the first 3 excited states for the first three parity groups. We have to leave out the $(3,1)$, $(1,3)$, and $(3,3)$ states due to numerical limitations (see Section 5.4.2). The resulting single-particle spectrum is depicted in Figure 5.5b. Note that each of these indicated states is spin degenerate.

For our simple model the overlap matrix for x (y) motion is 2×2. To conserve probability, the matrix must be unitary.[128] A real, unitary 2×2 matrix has the form

$$\begin{pmatrix} \beta & \gamma \\ -\gamma & \beta \end{pmatrix}$$

where $|\gamma| = (1 - \beta^2)^{1/2}$. If we specify β_x and β_y for the x and y overlaps, the total overlap matrix for the four coupled modes can be determined. For cylindrical structures $\beta_x = \beta_y = \beta$. Thus a single parameter determines the overlap matrix for a particular interface.

The strength β for the lateral mode coupling is determined by the overlap between lateral states in adjacent regions. If the confining potentials are parabolic, then the overlaps can

(a)

					(b)
				$6\hbar\omega$ $\{(3,2);(2,3)\}_8$	
(even,even)	$(0,0)$ - $(2,0)$ - $(0,2)$ - $(2,2)$			$5\hbar\omega$ $\{(2,2)\}_7$	
(odd,even)	$(1,0)$ - $(3,0)$ - $(1,2)$ - $(3,2)$			$4\hbar\omega$ $\{(2,1);(1,2)\}_5$ $\{(3,0);(0,3)\}_6$	
(even,odd)	$(0,1)$ - $(2,1)$ - $(0,3)$ - $(2,3)$			$3\hbar\omega$ $\{(1,1)\}_3$ $\{(2,0)(0,2)\}_4$	
(odd,odd)	$(1,1)$ $\boxed{(3,1)\ (1,3)\ (3,3)}$			$2\hbar\omega$ $\{(1,0)(0,1)\}_2$	
				$1\hbar\omega$ $\{(0,0)\}_1$	
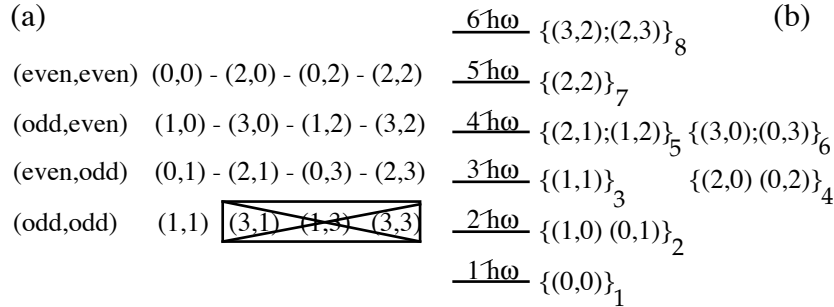
Figure 5.5 Parities and eigen-energies of included lateral states. (a) Subset of 16 lateral states (n_x, n_y) composed of 4 allowed quantum numbers in each dimension. Only states with the same x and y parity can couple to each other as indicated with dashes. States $(3,1)$, $(1,3)$, and $(3,3)$ are excluded in our calculation for reasons of numerical complexity. (b) Lateral single-particle eigen-energy spectrum. Each quantum state (n_x, n_y) is doubly spin degenerate. Grouping in curly brackets $\{\ \}_i$ indicates equivalent coupling to the leads; i.e. states in one group are equally likely occupied.

be determined analytically. Even if the confining potential is not exactly parabolic, the parabolic approximation should give a good qualitative estimate for the overlaps if the correct effective masses and lateral level spacings are used to model the parabolic potentials.

Estimates of β have been made for abrupt constrictions[128] for parameters appropriate for the quantum dot nanostructures, $\beta > 0.6$. In these calculations, we use β as a parameter, which we adjust in this range to test the effects of mode-mixing.

5.4.2 Implementation of Rate Equations

The rate equations as they were put forward by Beenakker[70] use a configuration space notation that indicates the occupation or vacancy of a Slater determinant by a 1 and a 0, respectively. Figure 5.5b indicates the structure of the single-electron quantum states that we are simulating. Altogether we are considering 13 spin degenerate states. The number of all possible configurations of these 26 quantum numbers in terms of an occupation number notation is $2^{26} \approx 6.7 \times 10^7$. The setup for a solution for all of the occupation probabilities would therefore result in a matrix of dimension $2^{26} \times 2^{26}$. However many of the lateral states are degenerate in energy and have equivalent coupling to the leads. This degeneracy can be used to reduce the number of equations that need to be solved.

To illustrate this degeneracy of states let us consider *single-particle*, lateral states characterized by two lateral quantum numbers, $n_{x(y)}$, and one spin index, α, denoted as (n_x, n_y, α). The 4 single particle states $(1, 0, \uparrow)$, $(1, 0, \downarrow)$, $(0, 1, \uparrow)$, and $(0, 1, \downarrow)$, for example, are energetically degenerate (Fig. 5.5b). Figure 5.5a indicates the coupling of $(1, 0, \alpha)$ to $(3, 0, \alpha)$, $(1, 2, \alpha)$ and $(3, 2, \alpha)$. Similarly the degenerate state $(0, 1, \beta)$ is coupled to $(0, 3, \beta)$, $(2, 1, \beta)$ and $(2, 3, \beta)$. Note now that these groups of coupled states $\{(3, 0, \alpha); (0, 3, \beta)\}$, $\{(1, 2, \alpha); (2, 1, \beta)\}$ and $\{(3, 2, \alpha); (2, 3, \beta)\}$ are also degenerate in energy. Given the equivalent coupling of the $(1, 0, \alpha)$ and $(0, 1, \beta)$ states to other states and their degeneracy, we compound these four single-particle states into one 4-fold degenerate state. This procedure leads to five 4-fold degenerate and three 2-fold degenerate states as indicated in Figure 5.5b. The dimension of the resulting configuration space is $5^5 \times 3^3 = 84375$. We can solve a system of equations of this dimension using iterative methods if we can provide a "good" guess for the solution. We defer the report of the rate equations, which utilize the the degeneracies as discussed above to Appendix C.

5.5   Numerical Results

In this section we present our results obtained for a multi-electron quantum dot system under high bias. We consider two example systems here: a symmetric and an asymmetric structure in which we analyze the effects of non-adiabatic transport, electron-electron charging and inelastic scattering.

5.5.1   Example Device

The example device we consider here is an undoped double barrier resonant tunneling structure (FIG. 5.6) which is sandwiched between lightly doped spacer layers and heavily doped contact layers. The transverse confinement changes in the longitudinal dimension due to the change of doping and the associated charge depletion along the growth axis of the diode. The single-particle energy spacing in the quantum dot, barriers and leads is assumed to be $15meV$, $16meV$ and $10meV$, respectively. A Fermi energy of $38meV$ populates the three lowest subbands in the leads. The conduction band floats up in the central region of the device due to the lack of doping $V_{float} = 50meV$. The well region is assumed to be $In_xGa_{1-x}As$ with a conduction band offset of $50meV$ and thickness of 60Å similar to the Reed[30] structure. We have estimated the energy quantization in the longitudinal direction to be $60meV$ and $245meV$ for the first two states with our Green's function simulator
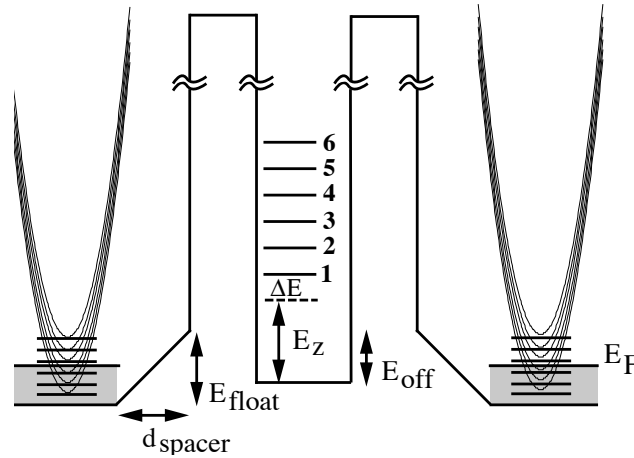
Figure 5.6   Conduction band profile for numerical simulation. Subband energy spacing in the leads is 10meV and single-particle state energy spacing in the quantum dot is 15meV. The Fermi energy in the leads is 38meV (3 subbands are occupied). The conduction band in the quantum dot and barriers is raised by $E_{float} = 50meV$ due to charge depletion. The quantum dot is assumed to be $In_xGa_{1-x}As$ with a conduction band offset of $E_{off} = 50meV$. The thicknesses of the spacer layers and the quantum well are 50Å and 60Å, respectively. The longitudinal energy quantization, E_z, is $60meV$. The temperature is $T = 0.9K$ corresponding to $k_BT = 0.08meV$. Barrier thicknesses and Al-fractions vary for the simulated symmetric and asymmetric structures.

QUEST.[56] Since the energy separation of these two longitudinal states is much larger than the assumed lateral state quantization we will neglect the second longitudinal state completely and consider only the lowest longitudinal quantum number state.

We assume that the single-particle state separations $\Delta E = 15 meV$, are larger than the charging energy, $U = 1.5 meV$. This allows us to use the simple charge interaction model (see Appendix C.4 for a discussion on charging models). Barrier thicknesses and Al-fractions[45] are chosen such that the single-particle levels can be assumed to be sharp with $\Delta E, U \gg k_B T \gg \hbar\Gamma$. This condition needs to be satisfied to use rate equations in the sequential tunneling picture.

5.5.2 Inelastic Scattering, Charging, and Subband Mixing treated independently

Before we put the effects due to inelastic versus elastic, charging versus no-charging, and adiabatic versus non-adiabatic transport together in two complex examples, we again present consequences of these three transport phenomena independently in this complicated electronic system. We will find that all the effects that we discussed in length in the analytic section 5.3 can be found in the numerical results. We consider an asymmetric structure with left/right barrier thicknesses of 105Å/80Å and an Al-fraction of 0.35/0.30 for these examples.

We use the simulation for elastic, adiabatic, no charge-interaction transport as baseline (thin line in Fig. 5.7) for comparison against the independent inclusions of inelastic scattering (Fig 5.7a), charge interaction (Fig. 5.7b) and subband mixing (Fig. 5.7c). The arrows marked "x–y" in Fig 5.7a indicate the voltage ranges over which subband "x" in the *emitter* can conduct adiabatically into quantum state "y" in the quantum dot. Note that due to (1) the different energy separations of the subbands in the leads ($10 meV$) and the single-electron states in the quantum dot ($15 meV$) and (2) the finite Fermi energy in the leads, the "3–3" transition is turning on when the "1–1" transition is already turned off[§]. As in our discussion in the analytical section we define the valley current region as the voltage region extending past the turn-off of the first transition (see arrow in Fig. 5.7a).

The introduction of inelastic scattering (solid line in Fig 5.7a) shows an increased current due to coupling of lower lying, elastically decoupled channels. The turn-off of the "1–1" transition, for example introduces a decrease in the current in the elastic calculation (thin line), however, electrons tunneling into the quantum dot in a "2–2" transition can relax down to level one in the quantum dot. Level one is therefore filled from the top via an inelastic channel. The current is increased due to this additional channel and the turn-off feature of the "1–1" transition is wiped out.

Fig 5.7b shows the effects of electron-electron charging in the elastic limit. The spin degeneracy of the single-electron states is broken by the charge interaction (arrow 1) and the turn-on of higher single-electron states is impeded (arrow 2) by the presence of two

---

[§]Section 2.5.1 treated adiabatic transport including several lateral modes. All modes turn off at the same bias in this limit (see Fig. 2.7)
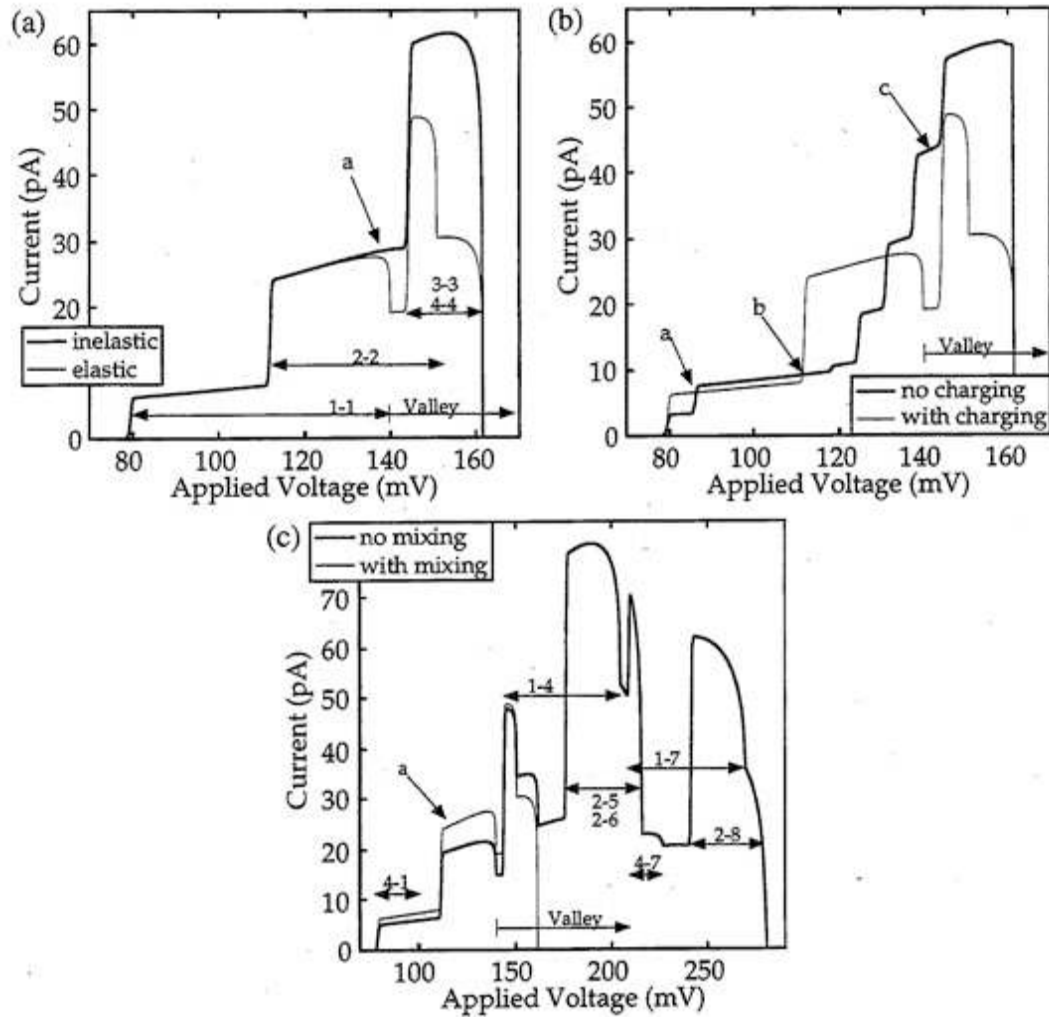
Figure 5.7 Effects due to (a) inelastic scattering, (b) electron charging, and (c) subband mixing are compared *independently* of each other to the elastic, adiabatic, single-particle result in an asymmetric structure. (a) Inelastic transport. Arrows labelled "x–x" indicate the regions of allowed adiabatic, elastic subband-to-quantum-state transitions where the numbers "x" correspond to the lateral state groups as indicated in Fig. 5.5. Electron relaxation wipes out features and increases the current in the "valley current" region where channel 1 has shut off already. (b) Single-electron charging. Spin degeneracy is broken (arrow a), turn-on of second single-particle level is impeded (arrow b). Current is increased in the "valley current" region (arrow c). Underlying single-particle spectrum cannot be identified. (c) Non-adiabatic transport. Subband mixing increases voltage-region of current flow. Unitarity condition on scattering matrix causes reduced current flow through direct channels (arrow a). Notation of the new coupling channels is the same as in (a).

electrons in the quantum dot. The valley current is increased as discussed in Section 5.3.1.

The increased region of current flow due to subband mixing is depicted in Fig 5.7c (solid line) and compared to the adiabatic result (dashed line). A weak subband mixing with $\beta = 0.95$ introduces a dramatic change in the overall I–V–characteristic (Note the change in the voltage scale.). The valley current is strongly enhanced. Arrow 1 indicates the reduced current of the I–V–characteristic due to subband mixing. Current conservation demands that the scattering matrix, which couples subbands and quantum states in the dot, to be unitary. Opening new scattering channels reduces the strength of the direct channels (arrow 1).

In the following two sections we will put the three transport phenomena (1) elastic versus inelastic transport, (2) non-interacting versus interacting transport and (3) adiabatic versus non adiabatic transport together piece by piece and explain their general effects on symmetric and asymmetric structures. For the symmetric structure we start from Bryant's[128–130] analysis of non-adiabatic transport in symmetric structures. We will show how the inclusion of charge interaction can change the high bias response of symmetric structures significantly. For the asymmetric structure we start from Averin's[69] analysis of adiabatic, thermalized transport through a charge interacting quantum dot and show how the inclusion of non-adiabatic transport phenomena and the exclusion of inelastic scattering in the quantum dot will alter the high bias I–V–characteristic dramatically.

5.5.3 Symmetric Structure

Is there single-electron charging? Single-particle quantum states in resonant tunneling diodes have first been observed by Reed[30] in a symmetric structure and evidence for single-electron charging effects has not been found. The supporting argument for the missing effects due to single electron charging is that the collector barrier is effectively lowered by the applied bias and that there is no charge accumulation to introduce effects due electron-electron interaction. However, the effect of the effective collector barrier lowering can be decreased if the barrier heights are raised. If then collector and emitter barrier transmission rates are of the same order of magnitude an average filling of a quantum state is 1/2. This will modify the excitation spectrum of the quantum dot and will leave an observable effect in the high bias I–V–characteristic. Another requirement[69,70] which is necessary for the observation of single electron charging effects has also not been satisfied in the symmetric Reed structure. The energetic spread of the quantum states due to the coupling to the leads can be estimated to be of the order of several meV, which is about the same order of magnitude as the charging energies involved with single electron charging. We therefore cannot expect to observe single electron charging effects. By the choice of thick barriers we can ensure, that we can satisfy the condition $\Delta E, U > k_B T \gg \hbar \Gamma$ for all possible transitions into and out of the quantum dot.

We analyze here the double barrier structure depicted in Fig. 5.6 with barrier thicknesses of 80Å and Al-fractions of 0.35. Fig. 5.8a depicts an I–V–characteristic that Bryant[128–130] could have obtained in his analysis of coherent, elastic transport through double barrier structures. Even weak subband mixing ($\beta = 0.93$) modifies the overall I–V–characteristic

significantly. Calculated modifications of this high bias characteristic due single-electron charge interactions are depicted in Figure 5.8b using a charging energy of $U = 1.5 meV$. There are clearly additional steps of the energy scale of $2U$ introduced due to single-electron charging. A slightly increased valley current due to electron charge interaction is visible as well.

Does Inelastic scattering play a role in symmetric structures? Figure 5.8c compares the simulations for perfectly elastic $(1/\tau = 0)$ and perfectly inelastic $(1/\tau \gg \Gamma)$ transport in the presence of electron charge interaction and subband mixing. The solid line from Fig. 5.8b is now dashed. The relative amplitudes of some current peaks (arrow 1) have changed
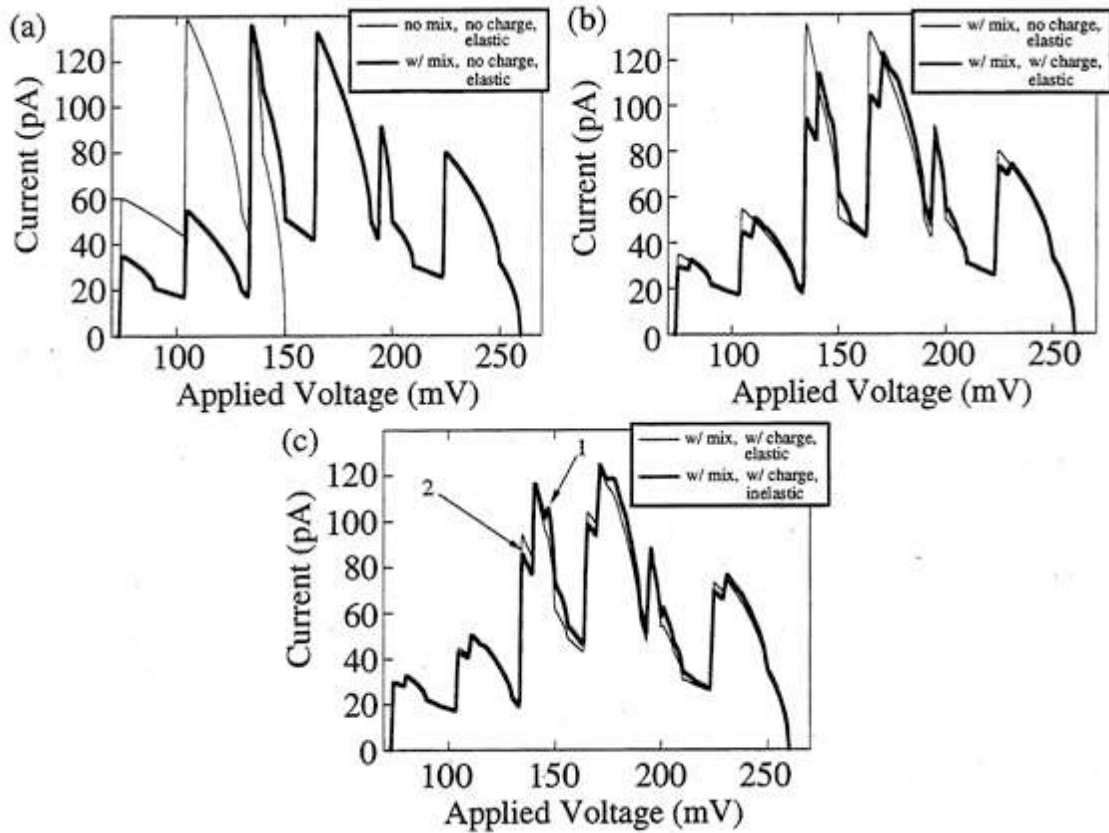
Figure 5.8 I–V–characteristic for a symmetric structure. Start with Bryant's "picture" (Ref. [128–130]) of coherent transport with and without subband mixing. We extend this picture to include single-electron charging and inelastic scattering. (a) adiabatic versus non-adiabatic transport. Voltage region of current flow is extended due to subband mixing $\beta = 0.93$ (thick line). (b) Include charging: Thick line from (a) is now thin. Electron-electron charging does introduce new features in the I–V–characteristic even for symmetric structures. (c) Include strong inelastic scattering: Thick line from (b) is now thin. Electron relaxation in the quantum dot has only small effects on the I–V–characteristic. Current is increased on the turn-off side of the peaks (arrow 1) and reduced on the turn on side (arrow 2).

due to the opening of new channels in the valley current (see Section 5.3.1). Current is slightly reduced due to inelastic scattering on the rise part of the I–V–characteristic (arrow 2) as discussed in Section 5.3.1. However, effects due to inelastic scattering in the quantum dot in the case of symmetric structures appear to be small. The two calculations for the extreme cases of $1/\tau=0$ and $1/\tau\gg\Gamma$ do give slightly different results but an experimental determination of relaxation times by high bias I–V–characteristics seems infeasible.

Conclusion: Our analysis shows that single electron charging will have effects on the high bias I–V–characteristic of symmetric double structures, provided the barriers are thick/high enough. In the limit of strong confinement where $\Delta E > U$ we expect the I–V–characteristic to be dominated by the single-particle spectrum. Superimposed on this spectrum we expect fine structure due to single electron charge correlations. Devices built in this parameter range would allow the clear separation of charging and quantum effects.

5.5.4   Asymmetric Structure

Averin[69] has assumed adiabatic coupling from 1D subbands in the leads to 0D states in the quantum dot for the lowest longitudinal energy level in his high bias transport analysis. He assumed that the electrons are in the quantum dot long enough to suffer an inelastic scattering process and calculated the canonical ensemble average. We start our analysis for asymmetric structures from this picture. However note that in our case we assume that the Fermi-energy in the same order of magnitude as the charging energy and the single-electron state separation (Fig. 5.6). This assumption allows us to analyze the effects of subband mixing and corresponds to doping levels similar to the structure by Reed[30] in which subband mixing is indeed important. Another difference in our analysis is that we keep the energy dependence of the collector barrier transmission rates, which makes the collector barrier more leaky at higher biases and reduces the charge accumulation.

The double barrier structure analyzed here is depicted in Fig. 5.6 with collector, emitter barriers thicknesses of 105Å, 80Å and *Al*-fractions of 0.35, 0.30, respectively. Figure 5.9a compares the effects due to single electron charging to the no-charging case. New steps reflecting the charging energy scale U have been introduced. The spin-degeneracy is broken (arrow 1) and the current has been impeded from single-particle turn-ons (arrow 2) on the rise part of the I–V–characteristic and the valley current (compare to Fig. 5.7a) is increased. The underlying single-particle spectrum cannot be identified in the high bias I–V–characteristic anymore, even though $U=1.5meV\ll\Delta E=15meV$.

Is subband mixing important in asymmetric structures?   Figure 5.9b shows the result of an inclusion of weak subband mixing (thick line) with $\beta = 0.95$ and compares it to to the formerly thick line of Figure 5.9a. The bias region of current flow is extended (note the change of scales) and the I–V–characteristic is dominated by the steps introduced by the electron-electron charge interaction. Note that the single electron spectrum current peaks (Fig. 5.7c) cannot be found in this result at all. Subband mixing changes the I–V–characteristic of asymmetric structures dramatically when the Fermi-energy, E_F, is of the same order of magnitude as the quantum dot energy scales: Charging energy, U, and single-electron spectrum, ΔE.

Does inelastic scattering play a role in asymmetric structures?   Inelastic scattering effectively couples lower lying quantum levels, that are not coupled elastically to the emitter lead in the valley current region. This issue has been discussed in detail in Chapters 2 and 3 in the context of the phonon-peak. The exclusion of inelastic scattering in the quantum
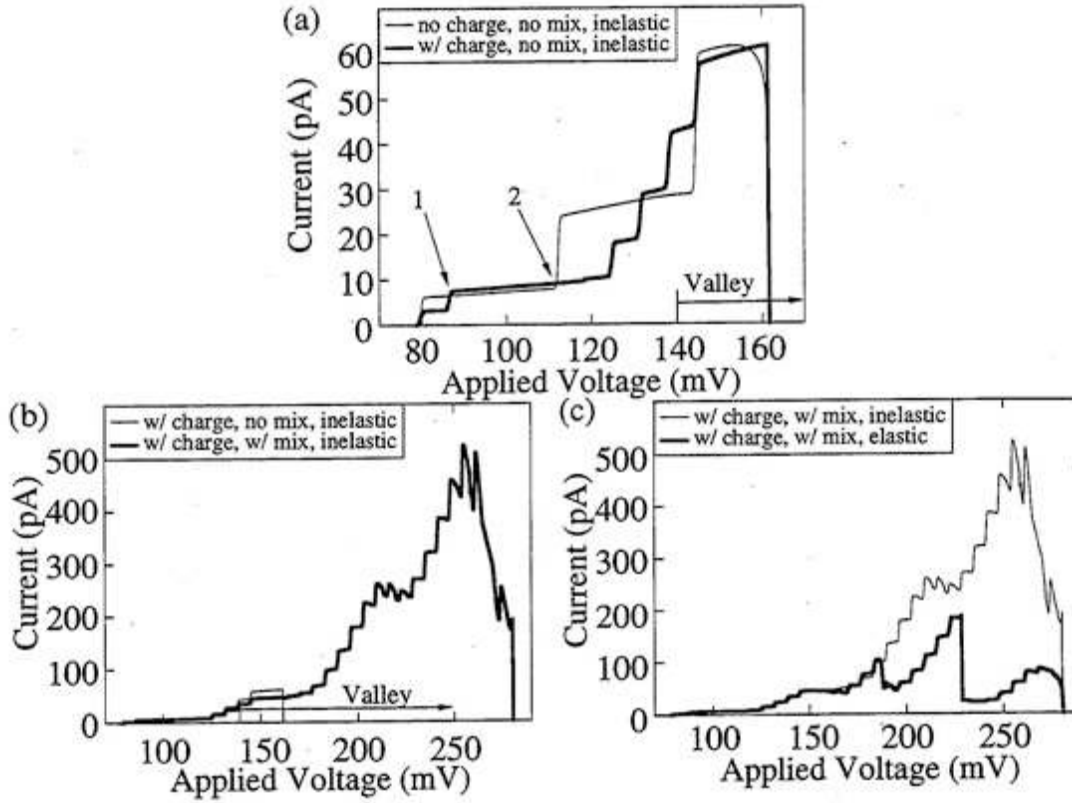
Figure 5.9 I–V–characteristic for an asymmetric structure. Start with Averin's "picture" Ref. [69] of inelastic, adiabatic transport with and without single-electron charging and show effects due to inclusion of subband mixing and exclusion of inelastic scattering. (a) Single-electron charging: Single-electron charging (thick line) introduces fine structure in the I–V–characteristic, breaks the spin degeneracy (arrow 1) and impedes current flow (arrow 1) at higher level turn-ons . (b) Include non-adiabatic transport: Thick line in (a) is now thin. Subband mixing increases the region of current flow. Features due to single-electron charging ($\approx 2{\times}U = 3meV$ are dominant. Single-particle spectrum (see Fig. 5.7c) cannot be identified. (c) Exclude inelastic scattering. Thick line in (b) is now thin. Fine structure due to the single-particle spectrum is exposed (see Fig. 5.7c).

dot (Fig. 5.9c) exhibits structure due to the single electron spectrum in the valley current region. Current is significantly reduced in this region. The two limits of $1/\tau \gg \Gamma$ (inelastic) and $1/\tau{=}0$ (elastic) give dramatically different results in asymmetric structures. The reverse bias measurement of an asymmetric structure will exhibit the single-particle spectrum since

there is no charge accumulation.[24] If single particle-features can still be found in the forward bias direction (this is the bias direction we considered here all along), we have an indication that the relaxation in the quantum dot is not very fast. If all the single particle features disappear, we have an indication, that the relaxation rate is large.

5.6   Conclusions

We have presented analytical and numerical results which explain the roles of inelastic scattering, single electron-charge interaction and non-adiabatic coupling to the leads in a 0D quantum dot. In the analytical work we have shown how all three of these effects increase the valley current of the I–V–characteristic compared to the non-interacting, non-adiabatic, single-particle analysis. We have analyzed numerically devices where the Fermi energy is comparable to the lateral state spacing. Non-adiabatic transport increases the voltage range of transport through symmetric and asymmetric structures. In symmetric structures effects due to single-electron charging have not been observed experimentally. However we show that additional steps in the I–V–characteristic should be observable even in the case of weak charge accumulation, provided the barriers are thick and/or high enough. The inclusion of inelastic scattering within the quantum dot does not introduce significant changes in the predicted I–V–characteristic of a symmetric quantum dot. Transport through asymmetric structures is shown to be dominated by charge accumulation in one bias direction. The treatment of inelastic scattering in the quantum dot modifies the predictions of high bias transport dramatically. Inelastic scattering effectively couples all lower lying levels to the emitter lead, as long as there is at least one (high level) entry channel. Weak inelastic scattering exposes the underlying single-particle spectrum in the valley current region and an experiment in this parameter range may give insight into the strength of the inelastic scattering in the quantum dot. Non-adiabatic transport appears to be very significant for asymmetric structures as well as for symmetric structures, if the Fermi energy is of the same order of magnitude as the quantum dot characteristic energies of Coulomb charging energy and single electron spectrum.

Overall we have tied two approaches together in our analysis: (1) non-adiabatic transport analysis in the elastic, no charge interaction limit, and (2) inelastic, charge interaction analysis in the adiabatic limit.

Chapter 6

Strongly Correlated Transport: Linear Response

6.1 Introduction

Single quantum dots have been widely studied and a fairly clear understanding of the transport through these artificial atoms has emerged.[7] Coupled quantum dots could be considered as artificial molecules and their study could open up new physics in which electron charging and electron coherence play a significant role. Most studies of coupled quantum dots include *only* charging.[142–147] Few studies[141, 148] have been performed on coupled quantum dots in which coherence and charge quantization are considered simultaneously.

The purpose of this chapter is to calculate the conductance spectrum including coherence and charging. Our approach is very similar to that developed by Beenakker[70] and Meir[71] for single dots. The main difference is that we calculate the exact many-body states of the "molecule" rather than a single "atom". We start with the ideal case of (1) identical dots, (2) no inter-dot charging, and (3) a single spin-degenerate lateral state in each dot. We then examine the effects of non-idealities, that are inevitable in an experiment. Due to numerical limitations, our method can be applied to a maximum of 12 single-particle states which is not sufficient to describe present day lateral structures. However, improved lithographic techniques will eventually allow lateral structures with fewer electrons. Using present day technology vertical structures can be fabricated having very few electrons.[24, 25, 30, 31] Such structures typically do not have a gate electrode[149, 150] which is necessary for linear response measurements. However, using shadow evaporation a sidewall gate could be fabricated as shown in Figure 6.1.

A system of two coupled quantum dots with one doubly spin-degenerate single-particle state in each dot (2×2 single-particle states) will exhibit four conductance peaks.[89] These peaks coincide with the fluctuation of the equilibrium number of electrons in the quantum dot as transitions $0 \to 1$, $1 \to 2$, $2 \to 3$, and $3 \to 4$ occur. These transitions of electron numbers in the quantum dot are expected to occur at characteristic Fermi energies that are determined by the transition energies of the many-body states in the quantum dot. The

---
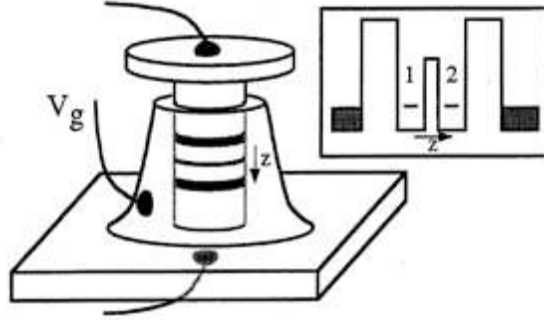
Figure 6.1 Proposed experimental set-up for a side-wall-gated small cross-section vertical triple barrier structure. Inset shows the simplified conduction band in the central region in the growth direction. Fermi-energy and lateral confinement can be changed with the gate voltage, V_g.

coupling strength t between the quantum dots and the charging interaction energy U in a single quantum dot determine the separation between the four conductance peaks. Here we show that that the expected double set of twin peaks in the conductance determined by the characteristic energies t and U survives against experimental non-idealities such as: (1) detuning of the bare energy levels of the quantum dots due to variations in confinement, (2) inter-dot charging, (3) excited lateral states, and (4) inelastic scattering.

6.2   Model

We consider a system described by a Hamiltonian with four terms: the coupled quantum dot (H_D), the charge interaction in the coupled quantum dot (H_C), the leads (H_L), and the coupling of the leads to the quantum dot (H_T).

$$H = H_D + H_C + H_L + H_T \tag{6.1a}$$

$$H_D = \sum_{\alpha;m;i} \epsilon_{im\alpha} c_{im\alpha}^\dagger c_{im\alpha} + \sum_{\alpha;m} \left(t_m c_{1m\alpha}^\dagger c_{2m\alpha} + c.c. \right) \tag{6.1b}$$

$$H_C = \sum_{i;m} U_{i;m,m} n_{im\uparrow} n_{im\downarrow}$$

$$+ \frac{1}{2} \sum_{\alpha,\beta;i;m\neq n} U_{i;m,n} n_{im\alpha} n_{in\beta}$$

$$+ \sum_{\alpha,\beta;m,n} W_{m,n} n_{1m\alpha} n_{2n\beta} \tag{6.1c}$$

$$H_L = \sum_{\alpha;m;k\in L,R} \epsilon_{km\alpha} c_{km\alpha}^\dagger c_{km\alpha} \tag{6.1d}$$

$$H_T = \sum_{\alpha;m;k\in L} \left(V_{km\alpha}^L c_{1m\alpha}^\dagger c_{km\alpha} + c.c. \right) + \sum_{\alpha;m;k\in R} \left(V_{km\alpha}^R c_{2m\alpha}^\dagger c_{km\alpha} + c.c. \right) \tag{6.1e}$$

The variables k and i symbolize states in the leads and the ith quantum dot, respectively. α and β are spin indices, and m, and n are lateral quantum numbers. $U_{i;m,n}$ represents the intra-dot, lateral state dependent repulsion in dot i. The inter-dot repulsion and inter-dot coupling between the two quantum dots are represented by $W_{m,n}$ and t_m, respectively. The tunneling matrix element V_{km}^L (V_{km}^R) connects dot 1 (2) to the left (right) lead. We assume the lateral confinement to be homogeneous and do not consider effects due to subband mixing[82] and energy dependence of coupling.

We assume the coupled quantum dots to be *weakly* coupled to the leads, such that H_T can be treated to first order in perturbation for single particle transitions. We evaluate the Hamiltonians H_D and H_C describing the decoupled "molecule" in the subset of constant numbers of electrons via direct diagonalization[151,152] in the basis of Slater determinants. In Appendix D we give an analytic example of the direct diagonalization scheme. We treat the coupled quantum dot as a *single* coherent system and use a conductance formula[70,71] which was developed for single quantum dots. However, the transition rates are more complicated in our case, since the spatial structure of the interacting eigen-states is more complicated:

$$G = \frac{e^2}{k_B T} \sum_{n=1}^{N_{max}} \sum_{ij} \frac{\Gamma_{nij}^L \Gamma_{nij}^R}{\Gamma_{nij}^L + \Gamma_{nij}^R} P_{n,i}^{eq} \left[1 - f(E_{n,i} - E_{n-1,j} - \mu)\right] \quad , \tag{6.2}$$

where Γ_{nij}^L indicate transitions from the ith n-particle state to the jth $(n-1)$-particle state via transitions through the left barrier. An example calculation of the transition elements can be found in Appendix D. $P_{n,i}^{eq}$ indicates the equilibrium occupation of the initial state (n,i) with eigen-energy $E_{n,i}$ calculated with

$$P_{n,i}^{eq} = \frac{1}{Z} exp\left[-\frac{1}{k_B T}(E_{n,i} - n\mu)\right], \tag{6.3a}$$

$$Z = \sum_{n,i} exp\left[-\frac{1}{k_B T}(E_{n,i} - n\mu)\right], \tag{6.3b}$$

where μ is the chemical potential in the leads. The electronic states in the leads are assumed to be 1-D subbands filled according to Fermi-Dirac statistics and $(1-f)$ indicates the probability to find an empty state in the lead, which satisfies the energy conservation requirement for the $(n,i) \rightarrow (n-1,j)$ transition. We assume the temperature to be high enough, such that we can neglect the Kondo effect due to correlations of electrons in the leads with electrons in the central system.

6.3   Results

6.3.1   Ideal Case

We start with the ideal case of a system consisting only of a single lateral, doubly spin degenerate state in each quantum dot. The conduction band we assume for our analysis is depicted in the insert of Figure 6.1. We assume the inter-dot charging to be zero ($W=0$)
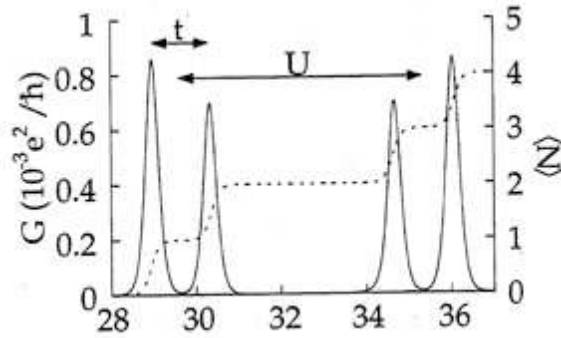
Figure 6.2   Conductance, G, (solid line) calculated for a system of coupled, symmetric quantum dots. Conductance peaks are grouped by charging energy, U, and the inter-dot coupling energy, t. Transitions in the total number of electrons, N, (dashed line) in the quantum dot coincide with the conductance peaks.

and assume the single-particle ground state in the two dots to be aligned with each other ($\epsilon_1 = \epsilon_2 = \epsilon$). The one-particle ground state of the coupled system is the bonding state with eigen-energy $E_1 = \epsilon - t$. Throughout this work we consider the case where the charging energy, U, is larger than the inter-dot coupling, t. Consequently electrons tend to distribute themselves throughout the structure to avoid the on-site charging energy and the two-particle ground state has an eigen-energy of $E_2 = 2\epsilon + O(t^2)$. The third electron has to "pay" charging energy in one of the quantum dots and the ground state of the three-particle ground state is $E_3 = 3\epsilon + U - t$. The fourth electron fills up the given orbitals and the eigen-energy of the four-particle many-body ground state is $E_4 = 4\epsilon + 2U$. Single-particle transitions which alter the number of electrons in the quantum dot can therefore occur at four particular Fermi-energies: $\epsilon - t$, $\epsilon + t$, $\epsilon + U - t$, and $\epsilon + U + t$.

We have calculated the conductance spectrum for energy independent tunneling matrix elements $V_{k\alpha}^{L/R}$ with a single particle single barrier transition rate $\Gamma = 1 \mu eV$ assuming that $\epsilon = 30 meV$, $t = 1 meV$, and $U = 5 meV$. The resulting conductance, G (solid line), is depicted in Fig. 6.2 with the corresponding average number of electrons in the quantum dot, $\langle N \rangle$ (dashed line), as a function of Fermi-energy. Note that the conductance peaks occur whenever the number of particles changes. There are 4 conductance peaks corresponding to the filling of the quantum dot system with 4 electrons. We obtain two sets of twin peaks where the 'twins' are separated by the inter-dot coupling energy t and the sets are separated by the intra-dot repulsion, U. The upper two peaks are the energetic mirror image of the lower

two taken at mid gap which is due to electron-hole symmetry in the problem. Note that the second peak is smaller than the first peak *not* due to an energy dependent tunneling rate, but due to the spatial and energetic structure of the many-body states in the dot (see Appendix D).

6.3.2 Detuning

Non-uniformities in the lateral or the longitudinal confinement of the quantum dots will lead to some detuning Δ of the single electronic ground states between the two dots (insert in Fig. 6.3). Figure 6.3 compares the calculated conductance for the coupled quantum dot system we discussed above for three different detunings (a) $\Delta = 0$, (b) $\Delta = U$, and (c) $\Delta = 2U$. The conductance G is plotted on the same linear scale in all three plots. Note that the first and fourth peak decrease in amplitude while the second and third peak are roughly unchanged in (a) and (b). Not only do the amplitudes of the four peaks change, but also their locations, indicative of changes in the excitation spectrum of the coupled quantum dots.

Figure 6.4 analyzes the conductance peak spectrum (a) and amplitudes (b) separately as a function of detuning, Δ. The amplitudes of peaks one and four (dashed lines) are equal as well as the amplitudes of peaks two and three (solid line). As the single-particle eigen-energy of the decoupled dots is raised in the second quantum dot, the first electron tends to localize in the first dot of the coupled system and the localization increases with detuning. The eigen-energy of the composite single-particle ground state changes (Fig. 6.4a) from $E_1 = \epsilon - t = 29meV$ ($\Delta = 0$) to $E_1 = \epsilon = 30meV$ ($\Delta = \infty$). As a result of the decreasing probability of finding the electron in the right well, the amplitude of the first conductance peak (Fig. 6.4b) decreases rapidly with detuning ($\propto \frac{t^2}{\Delta^2}$). For a symmetric structure without detuning we have equal probability to find an electron in the left or the right quantum dot ($\langle n_1 \rangle = 0.5$ in Fig. 6.3a). Figure 6.3b shows the average number of electrons in quantum dot 1 ($\langle n_1 \rangle$) at a detuning of $\Delta = 5meV$ as a function of the Fermi-energy. The average of ≈ 1 past the first conductance peak indicates the localization of the first electron in the left quantum dot.

Formally we denote the many-body states in a occupation number notation of the form $|n_{1\uparrow}, n_{1\downarrow}, n_{2\uparrow}, n_{2\downarrow}\rangle$, where the index 1 (2) refers to the left (right) dot and $\uparrow$, $\downarrow$ are spin indices. Using this notation we find that the one particle ground-state is two-fold degenerate with one up-spin and one down-spin state. We denote them neglecting the normalization as $|\psi_{1\uparrow}\rangle = |1,0,0,0\rangle - \alpha|0,0,1,0\rangle$ and $|\psi_{1\downarrow}\rangle = |0,1,0,0\rangle - \alpha|0,0,0,1\rangle$, where $\alpha \propto \frac{t}{\Delta}$. The probability to find an electron in dot two and the coupling to the right lead by transitions into state $|0,0,0,0\rangle$ is proportional to α^2.

Intuitively one expects the second conductance peak to exhibit the same behavior with detuning as the first peak. Given small detuning, $\Delta \ll U$, the 2-particle ground state is given[§] by $|\psi_2\rangle \approx |1,0,0,1\rangle + |0,1,1,0\rangle$, neglecting normalization. Transitions through the left barrier (e.g. $\langle \psi_{1\uparrow}|c_{1\downarrow}|\psi_2\rangle \approx \alpha$, where $c_{1\uparrow}$ is the up-spin destruction operator in dot 1)

[§]The states $|1,0,1,0\rangle$ and $|0,1,0,1\rangle$ are not included in the 2-particle ground state since they are not coupled to any other state in the set of six Slater determinants by the inter-dot coupling, t. They are therefore

are limited by the localization an electron in dot 1 and the weak leakage to dot 2. This is one possible current contribution to the second conductance peak. The intra-dot charge
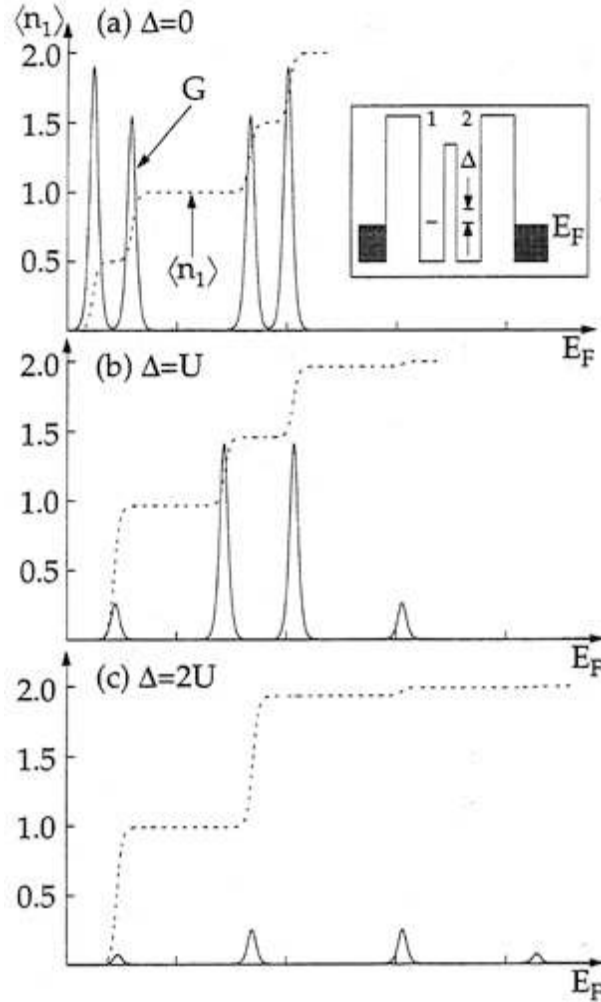
Figure 6.3 Conductance spectra G, (solid line) for different degrees of detuning, Δ, of the 2nd quantum dot against the 1st quantum dot (inset). (a)-(c) show G on the same scale for $\Delta{=}0$, $\Delta{=}U$, and $\Delta{=}2U$ in arbitrary units. Dashed line shows the average number of electrons in the 1st quantum dot ($\langle n_1 \rangle$).

interaction introduces a resonance feature (at $\Delta = U$) that allows for a second transport process through the quantum dot at even higher detuning. The argument is as follows.

---

two degenerate eigen-states of the coupled system with eigen-energy $\epsilon_1{+}\epsilon_2$. The basis state $|0,0,1,1\rangle$ is left out in this argument here because has an energy of $2\epsilon{+}2\Delta{+}U$ as diagonal entry in the $N{=}2$ Hamiltonian which is significantly higher in energy than the diagonal element $2\epsilon{+}U$ of basis state $|1,1,0,0\rangle$ and its contribution to the ground state is negligible.

When $\Delta = U$ we have a degeneracy of the three[‡‡] basis states $|1,0,0,1\rangle$, $|0,1,1,0\rangle$ and $|1,1,0,0\rangle$, which make up the ground state. The basis state $|1,1,0,0\rangle$ can couple well with
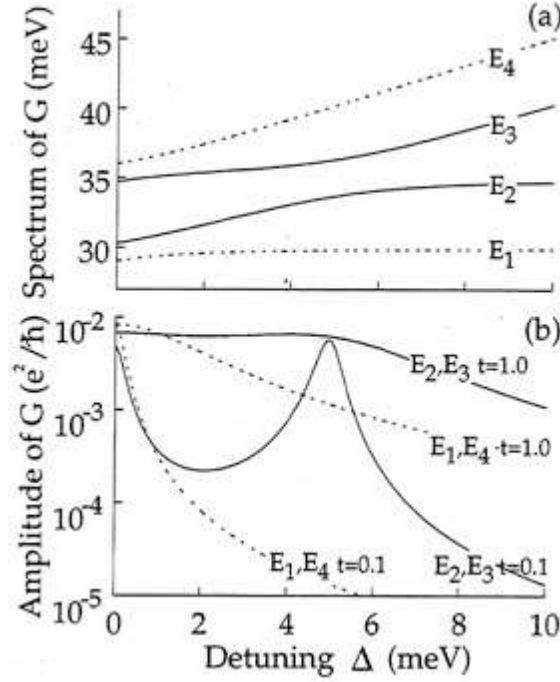
Figure 6.4 Conductance peak spectrum (a) and amplitudes (b) as a function of detuning, Δ. (a) $\Delta=0$ shows 2 sets of twin peaks at $E_F = 29$, 30 and 35, $36meV$ for $\epsilon_0=30meV$, $U=5meV$, and $t=1meV$. Anti-crossing is visible at $\Delta=U=5meV$. (b) Dashed lines correspond to the 1st and 4th peak in (a). Solid lines correspond to the 2nd and 3rd peak in (a). Inter-dot coupling t is a parameter. 2nd and 3rd peak are almost independent of detuning Δ if the inter-dot coupling, t, is large enough.

the 1-particle ground states $|\psi_{1\uparrow}\rangle \approx |1,0,0,0\rangle$ and $|\psi_{1\downarrow}\rangle \approx |0,1,0,0\rangle$ via transitions through the *left* barrier. The basis states $|1,0,0,1\rangle$ and $|0,1,1,0\rangle$ are well coupled to $|\psi_{1\uparrow}\rangle$ and $|\psi_{1\downarrow}\rangle$ by transitions through the *right* barrier. The 2-particle ground state is therefore well coupled to the 1-particle ground state via transitions through the *left and* the *right* barrier and the second conductance peak is large. Figure 6.3b indicates an average number of electrons in the first quantum dot of ≈ 1.5 in the case of equal detuning and intra-dot charging. $\Delta=U$ is the transition region where the "energetic payment" to reside in a higher single-particle level in dot 2 or the charging energy against the first electron in dot 1 are equal. This means that the second electron is actually 50% of the time in the first quantum dot "next" to the localized first electron.

Increased detuning where $\Delta > U$ will tend to localize *both* electrons in quantum dot 1

[‡‡]See footnote on page 67

and the ground state will consist mostly of basis state $|1, 1, 0, 0\rangle$. Figure 6.3c indicates an average number of electrons of ≈ 2 out of 2 electrons total in quantum dot 1 past the second conductance peak. The conductance will then decrease rapidly with Δ since no electrons are in quantum dot 2 to be coupled to the right similar to the behavior of the first peak amplitude.

The region of intermediate detuning where the detuning is smaller than the intra-dot charging energy $(0 < \Delta < U)$ is determined by a "competition" between the two transport processes discussed above. The first process is dependent on the leakage $\alpha \propto \frac{t}{\Delta}$ of the 1-particle state into dot 2. The second process is dependent on the mixing of the $|1, 1, 0, 0\rangle$ basis state into the 2-particle ground state. The 2-particle ground state is a spin 0 state and can be denoted as [‡‡] $|\psi_2\rangle = |1, 0, 0, 1\rangle + |0, 1, 1, 0\rangle + \beta|1, 1, 0, 0\rangle$, neglecting normalization, where $\beta \propto \frac{t}{U-\Delta}$ for $\Delta \ll U$. Transition contributions due to $\alpha \propto \frac{t}{\Delta}$ (localization of the first electron) decrease with detuning and contributions due to $\beta = \frac{t}{U-\Delta}$ (mixing of $|1, 1, 0, 0\rangle$) increase with detuning. Both contributions are proportional to the inter-dot coupling t. and the amplitude of the second conductance peak appears to be almost independent of detuning if the strength of the inter-dot coupling is strong enough (Fig. 6.4b).

The third and fourth conductance peak can be most easily understood by the formal electron-hole-symmetry in our notation. Every "electron" Slater determinant (e.g. $|1, 0, 0, 0\rangle$) has a complementary "hole" Slater determinant (e.g. $|0, 1, 1, 1\rangle$). The same arguments that we have given for the first two conductance peaks in terms of electron localization can be extended to arguments following hole localization. We can explain the first conductance peak with the transition of the first electron into the system from the $|0, 0, 0, 0\rangle$ state, similarly we can explain the fourth conductance peak with the transition of the first hole into the system from the $|1, 1, 1, 1\rangle$ state. Conductance peak one and four have therefore the same amplitude as functions of Δ (see Fig. 6.4). Indeed we find the amplitudes of peak two and three to be the same functions of Δ.

It is interesting to note that the conductance peaks coincide with fluctuations in the total number of particles in the quantum dot. Given the discrete energy spectrum of this system, the total number of particles always increases by one (see Fig. 6.2) with the same slope at every step (assuming small temperatures) independent of the detuning of the quantum dots ($\frac{\partial \langle N \rangle}{\partial \mu}$ is the same for all transitions.). The conductance amplitude however is dependent on the spatial structure of the composite many-body eigen-states and depends on the detuning.

Figure 6.4a shows the spectrum of the excitation energies of the coupled quantum dot as a function of detuning. An anti-crossing of the second and third excitation is visible at a detuning of $\Delta = U$ where the localization of 1 electron changes to the localization of 2 electrons in one quantum dot. We can see (Fig. 6.4b) how conductance peak 1 (4) decreases rapidly with Δ due to localization of the first electron (last hole) and peak 2 (3) decreases after localization of 2 electrons (holes). Although the relative amplitude and the spectrum of the conductance peaks change with detuning we still expect the double set of twin peaks to be observable. It is important to design the experimental structure such that the coupling between the two quantum dots is strong enough to compensate for detunings

---

[‡‡]See footnote on page 67

which are inevitable due to inhomogeneities in the confinement.

6.3.3 Inter-Dot Charging

Another physical process that may distort the double set of twin peaks in the conductance spectrum is inter-dot charging. With significant charge interaction[141] it seems reasonable that a strongly localized wave function in one quantum dot causes a non negligible potential in the neighboring quantum dot. Figure 6.5 shows the conductance peak spectrum (a) and amplitude (b) calculated as a function of inter-dot charging for the ideal structure discussed above. We have scanned the value of inter-dot charging from $0meV$ up to the value of intra-dot charging of $U=5meV$. Neither the locus nor the amplitude of the first conductance peak change since the addition and extraction of the first electron into and out of the system does not involve any inter-dot charging energy.
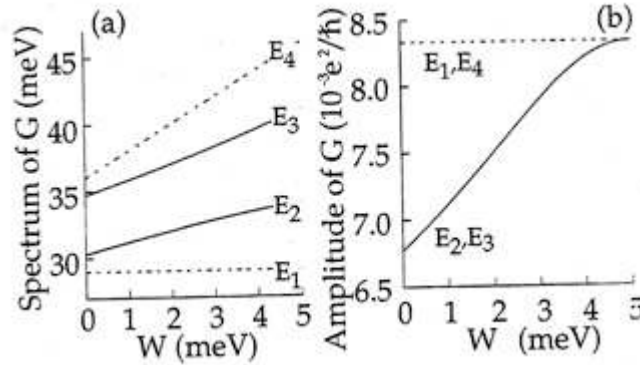
Figure 6.5 Conductance peak spectrum (a) and amplitude (b) as a function of inter-dot charging, W. (a) 1st peak is unchanged, 4th peak changes linearly with inter-dot charging. (b) Dashed line corresponds to peaks 1 and 4 in (a). Peaks 2 and 3 (solid line) increase until all four peaks have the same amplitude at $W=U$ where inter-dot and intra-dot charging energy are the same.

The locus of the second conductance peak becomes separated (almost) linearly from the first conductance peak as the inter-dot charging is increased linearly since the eigen-energies of the dominant[‡‡] Slater determinants $|1,0,0,1\rangle$ and $|0,1,1,0\rangle$ are $2\epsilon+W$. The two Slater determinants $|1,1,0,0\rangle$ and $|0,0,1,1\rangle$ have eigen-energies of $2\epsilon+U$. The strength of their mixture into the 2-particle ground state increases with the decrease in $U-W$. Since $|1,1,0,0\rangle$ and $|0,0,1,1\rangle$ are the states that allow for transport through the structure, as discussed above for the state $|1,1,0,0\rangle$, we expect the conductance to increase with an increased mixture of these basis states into the ground state.

The spatial separation of charges into different quantum dots ($|1,0,0,1\rangle,|0,1,1,0\rangle$) is energetically not preferable anymore once the limit of $W=U$ is reached. Indeed the degeneracies of the coupled dot eigen-state develop such that the first and the second conductance

---

[‡‡]See footnote on page 67

peak have the same amplitude in this limit. The loci of the third and fourth conductance peaks separate themselves from the previous peak with the same proportionality to inter-dot charging. The amplitude of the third and fourth conductance peak can be explained in the same fashion as the first and second peak by electron-hole symmetry[¶].

Notice that the double set of twin peaks is preserved even when inter-dot charging is included in the model. However, note that the separation of the conductance peaks does contain some information about the inter-dot charging energy. The energy difference between the first two and the last two peaks cannot be identified with the inter-dot coupling, t. Similarly the separation between the two sets of peaks cannot be identified with the intra-dot charging energy, U.

6.3.4 Multiple Lateral States

We now consider the influence of multiple lateral states on the conductance spectrum of the coupled quantum dots. The lateral confinement determines the single-particle energy quantization in the lateral dimensions. Strong confinements resulting in level separations of $\Delta E = 30\sim 50 meV$ have been observed.[30, 133] These values are larger than the observed[24, 25] single-electron charging energies which are of the order of $0.5\sim 5 meV$. If the lateral energy quantization, ΔE, is comparable to the charging energies, U, and the coupling t, we expect the excited lateral states to be mixed into the ground states of the coupled system. This would destroy the appearance of a double set of twin peaks in the conductance spectrum discussed above.

We have included the first two degenerate excited lateral states corresponding to a harmonic confinement potential. We have excluded any higher excited lateral states and considered only the diagonal elements of full[34] charge interaction Hamiltonian as indicated in Eq. 6.1. We have included the exchange interaction in that an electron does not "feel" the potential due to itself. We have calculated Hartree-type charging energies for a Coulomb and a screened Coulomb interaction[82, 134, 139] and have found a strong dependence on the choice of screening length. We defer a discussion of these calculations and the inclusion of off-diagonal elements to a later publication and use only order of magnitude estimates for the charging energies in this calculation.

Figure 6.6a shows the calculated conductance with a lateral energy quantization of $\Delta = 15 meV$. All intra-dot charging energies are taken to be $U = 5 meV$ independent of the lateral quantum number. The other parameters are still the same as in the previous discussions. The conductance spectrum shows two well separated groups of peaks due to the decoupled system ground states and the decoupled system excited states. There is no mixing of the excited states Slater determinants into the the lower group due to the large lateral energy quantization. The two groups could be calculated separately as the conductance spectrum of a coupled dot with one and a coupled dot with two lateral states.

[¶]Reference [89] shows how inter-dot charging breaks the electron-hole symmetry in a finite chain of quantum dots, due to localization of charge in the center of the chain, away from the two outermost quantum dots. The electron-hole symmetry is not broken here because only two equivalent dots are involved. See also Section 7.2.3 for a brief discussion of a finite chain of quantum dots.

Planes A and B in Figure 6.6a indicate the internal symmetries of the upper and lower
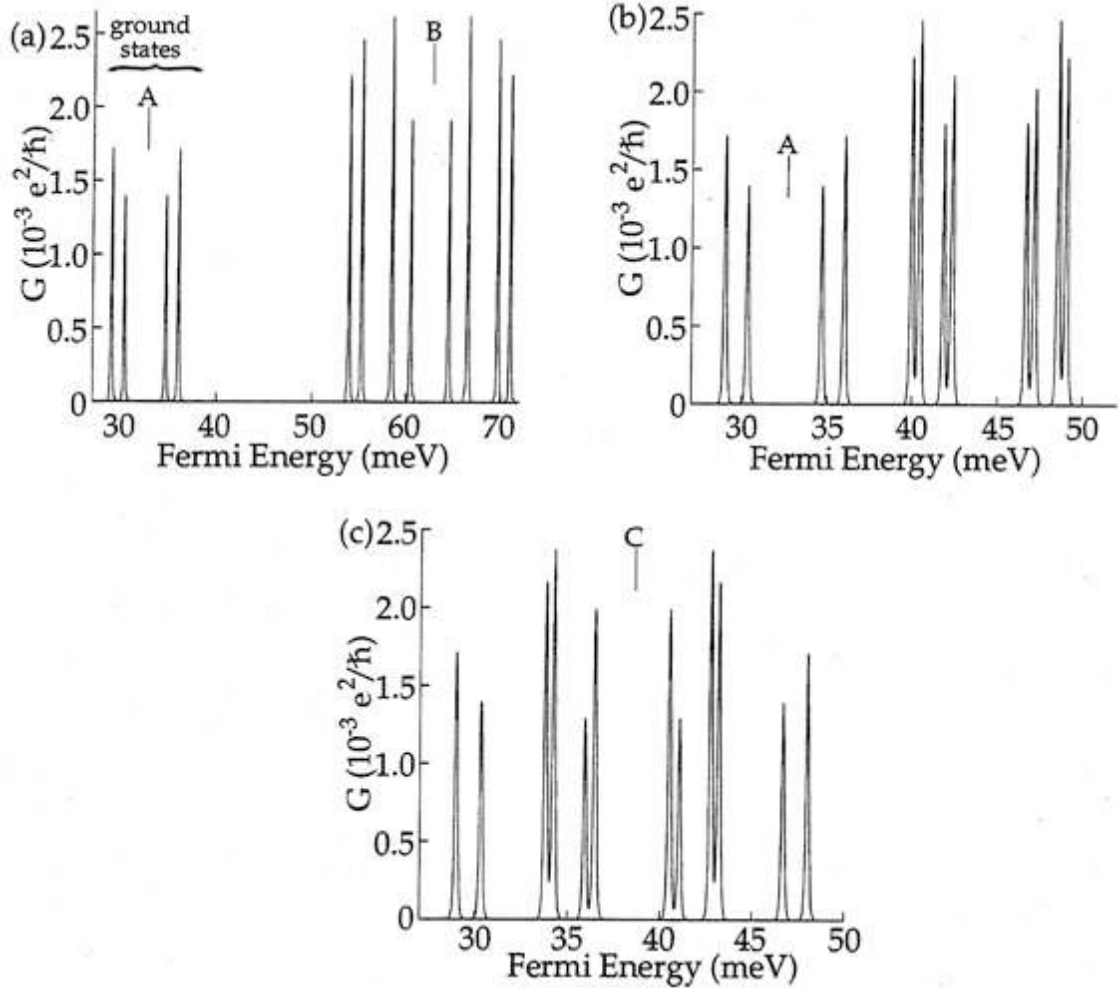
Figure 6.6 Inclusion of higher lateral modes. Conductance vs. Fermi energy including the first excited lateral modes. ($k_BT=0.05meV$, $t=1meV$.) Planes of symmetry are indicated by vertical lines and labelled A, B, and C. (a) $\Delta E=15meV$, state independent intra-dot charging $U=5meV$. Set due to lateral ground state (plane A) is well separated from higher lateral states (plane B). Each set has its own symmetry plane. (b) $\Delta E=5meV$, $U_{\{0,0\}\leftrightarrow\{0,0\}}=U_{\{1,0\}\leftrightarrow\{1,0\}}=5meV$, $U_{\{0,0\}\leftrightarrow\{1,0\}}=3meV$, and $U_{\{1,0\}\leftrightarrow\{0,1\}}=1meV$. The two groups are still separated. Symmetry of upper group is broken and only the lower group has still the same peak symmetry (A). (c) $\Delta E=2meV$, same charging parameters as in (b). Lateral ground states and higher states are mixed. Only one plane of symmetry in the middle of the spectrum (C).

group. The double set of twin peaks appears to survive given the strong confinement.

We now reduce the lateral energy quantization, ΔE, to $5meV$ *and* make the charging energies lateral state dependent. This state dependence can be understood as follows in

terms of single-particle, single quantum well harmonic oscillator quantum numbers $\{n_x, n_y\}$. With the three different lateral states $\{0,0\}$, $\{1,0\}$, and $\{0,1\}$ included in this calculation we have four distinct, direct charging energies $U_{\{0,0\}\leftrightarrow\{0,0\}}$, $U_{\{0,0\}\leftrightarrow\{1,0\}}=U_{\{0,0\}\leftrightarrow\{0,1\}}$, $U_{\{1,0\}\leftrightarrow\{1,0\}}=U_{\{0,1\}\leftrightarrow\{0,1\}}$, and $U_{\{1,0\}\leftrightarrow\{0,1\}}$. $U_{\{0,0\}\leftrightarrow\{0,0\}}$ and $U_{\{1,0\}\leftrightarrow\{1,0\}}$ involve the overlap of identical single-particle wave-functions and tend to be the largest ones in the group of four. Since the $\{1,0\}$ wave-function is spatially spread out more than the $\{0,0\}$ wave-function we have $U_{\{1,0\}\leftrightarrow\{1,0\}}\leq U_{\{0,0\}\leftrightarrow\{0,0\}}$. The other two charging energies involve the overlap of different orbitals and the corresponding charging energies are reduced compared to the first two. In addition $U_{\{1,0\}\leftrightarrow\{0,1\}}$ includes the overlap of two wave-functions of different parity and we generally have $U_{\{0,0\}\leftrightarrow\{0,0\}}\geq U_{\{1,0\}\leftrightarrow\{1,0\}}>U_{\{0,0\}\leftrightarrow\{1,0\}}>U_{\{1,0\}\leftrightarrow\{0,1\}}$.

Figure 6.6b shows the calculated conductance spectrum for a decreased lateral energy quantization of $5meV$. The charging energies are taken to be state dependent with values of $U_{\{0,0\}\leftrightarrow\{0,0\}}=5meV$, $U_{\{1,0\}\leftrightarrow\{1,0\}}=5meV$, $U_{\{0,0\}\leftrightarrow\{1,0\}}=3meV$, and $U_{\{1,0\}\leftrightarrow\{0,1\}}=1meV$. The two groups of the conductance spectrum have moved closer together in energy but appear distinguishable separated by about $U_{\{0,0\}\leftrightarrow\{1,0\}}=3meV$. The lower group due to the lateral ground states appears to be unchanged (symmetry plane A) whereas the relative amplitude and location of the conductance peaks of the second group (due to the excited lateral states) has changed due to the changed charging parameters. The upper group appears to be split into two groups by $U_{\{1,0\}\leftrightarrow\{1,0\}}=5meV$ and the grouping in these subgroups appears to be determined by $t=1meV$ and $U_{\{1,0\}\leftrightarrow\{0,1\}}=1meV$. Note that the conductance peak spectrum of the upper group is not symmetric to its central gap anymore, due to mixing of the states in the two groups. Overall we can see how the state dependent charging energy starts to correlate the excited lateral states and changes the transition energies and conductance peak amplitudes. The lower group consisting of the double set of twin peaks still survives, as long as the lateral quantization energy, ΔE is larger than the charging energies.

The resulting conductance peak spectrum in the case of further reduction of the lateral mode spacing to $\Delta E=2meV$ is depicted in Fig. 6.6c. The charging energies, U, are now comparable to the single electron lateral quantization energy, ΔE. Excited and ground state Slater determinants are now mixed into the single and two-particle ground states of the coupled system. The two conductance peak groups have merged together. The charging energies $U_{\{0,0\}\leftrightarrow\{0,0\}}= U_{\{1,0\}\leftrightarrow\{1,0\}}=5meV$ seem to split the conductance spectrum into two mirror images (symmetry plane C). If the lateral energy quantization, ΔE, becomes comparable to the charging energies, U, in the system we can see that the conductance spectrum which is indicative for the excitation spectra of the system for the lowest many-body states become severely modified due to electron charge correlations. This effect is evident without the inclusion of off-diagonal charge interaction elements into the Hamiltonian. In the example of Figure 6.6c we have a lateral quantization energy of $\Delta E=2meV$ which is smaller than some of the charging energies. In this case we expect even higher lateral modes ($\{1,1\}$, $\{2,0\}$, etc.) to be mixed into the ground state of the many-body system.

In practice, the confinement not only affects the lateral state quantization, but also the charging energies between the different lateral states (due to the different spatial spread of the wave-function). The expected changes in the charging energies with changing confine-

ment will depend strongly on the strength of the screening of the Coulomb interaction. In the case of strong screening we only find relatively small changes in the charging energies. We therefore have not included this effect into our calculations here.

6.3.5 Inelastic Scattering

We can account for strong inelastic scattering by using the following expression for G instead of Eq. 6.2:

$$G_{in} = \frac{e^2}{k_B T} \sum_{n=1}^{N_{max}} P_n^{eq} \frac{\langle\langle\Gamma_n^L\rangle\rangle\langle\langle\Gamma_n^R\rangle\rangle}{\langle\langle\Gamma_n^L\rangle\rangle + \langle\langle\Gamma_n^R\rangle\rangle} \tag{6.4}$$

where

$$\langle\langle\Gamma_n^{L(R)}\rangle\rangle = \sum_{ij} \Gamma_{nij}^{L(R)} F_{eq}(E_{n,i}|n)\left(1 - f(E_{n,i} - E_{n-1,j} - \mu)\right) \tag{6.5a}$$

$$P_n^{eq} = \sum_i P_{n,i}^{eq} \tag{6.5b}$$

$$F_{eq}(E_{n,i}|n) = \frac{1}{Z_n} exp\left(-\frac{E_{n,i}}{k_B T}\right) \tag{6.5c}$$

$$Z_n = \sum_i exp\left(-\frac{E_{n,i}}{k_B T}\right) \tag{6.5d}$$

This formula is essentially the same as that derived by Beenakker[70] for single quantum dots. The main difference is that the coupling terms, $\Gamma^{L(R)}$, have been modified to account for the nature of the electronic-states in coupled quantum dots. The effect of inelastic scattering in linear response is to thermally average all transitions through the left and the right barrier (Eq. (6.5a)) for the subset of constant number of electrons, n, in the quantum dot. $F_{eq}(E_{n,i}|n)$ is the canonical distribution function indicating the conditional probability of state (n,i) being occupied, given n electrons in the system.

The two conductance formulas in Eqs. (6.2) and (6.4) give the same[70] result under two independent conditions if 1) $\Gamma_{nij}^L/\Gamma_{nij}^R = const, \forall(nij)$, or 2) $k_B T \ll E_{n,excited} - E_{n,ground}$. For the non-idealities we have considered in this paper condition one is only violated in the case of detuning. Detuning introduces an asymmetry into the eigen-states of the system such that the ratio of left lead to right lead coupling becomes state dependent. We find that the amplitudes of the conductance peaks do change due to inclusion of inelastic scattering, however, the general shape of the conductance peaks does not change in the case of $k_B T \approx t$. The features due to inter-dot coupling t, will be thermally broadened and cannot be resolved in this limit. Since we are interested in resolving features of energy scale t, we require temperatures with $k_B T \ll t$ and Eqs. (6.2) and (6.4) will give the same results (condition 2 from above).

6.4 Conclusions

We have presented calculations of conductance spectra for two strongly coupled quantum dots that are weakly coupled to the adjoining leads. The conductance spectrum due to the first four electrons is determined by intra-dot charging, U, and inter-dot coupling, t. We analyze the effect of experimental non-idealities such as quantum dot detuning, inter-dot charging, excited lateral states and inelastic scattering on the conductance spectrum. We find that the spectrum is altered due to the first three effects, but the qualitative features persist. We suggest that the inter-dot coupling be made sufficiently strong, such that detuning due to variations in confinement does not decrease the amplitudes of the conductance peaks significantly. We show that strong confinement will ensure that excited lateral states should not change the symmetry of the ideal conductance peak structure of 2 sets of twin peaks. The conductance peak spectrum will contain information about the characteristic energies like intra- and inter-dot charging energies U and W, inter-dot coupling, t, detuning, Δ, and lateral mode spacing, ΔE. Inelastic scattering does not significantly alter the low-temperature conductance peak spectrum. The location of the conductance peaks coincides with transitions in the total number of electrons in the quantum dot. However, the peak amplitude is strongly dependent on the spatial properties of the many-body states in the quantum dots and varies from one peak to another although $\frac{\partial \langle N \rangle}{\partial \mu}$ is the same for every transition.

Chapter 7

Suggestions for Future Work

Following the division of this report into two parts according to 1) large cross-section DBRTD's (Chapters 2 and 3), and 2) small cross-section DBRTD's (Chapters 5 and 6) we divide up our suggestions for future work along these lines. Large cross section DBRTD's have been studied over a significant time now and have the potential for several possible applications[1,2,8–23] in the near future as oscillators, detectors, or switches. For an actual device design a modelling tool, which contains more sophisticated scattering mechanisms than implemented in QUEST[56] is necessary. We will suggest and motivate further work on a next generation device simulator in Section 7.1. Small cross-section DBRTD's (quantum dots or artificial atoms) have only been studied for a comparatively short time. Possible device concepts, device modelling and device design are still in their infancy. We will present several suggestions with regard to the modelling of small cross-section vertical quantum structures in Section 7.2.

7.1 Large Cross Section Structures

7.1.1 Anisotropic Scattering

Our previous work on the phonon peak problem was limited to purely one dimensional structures for two reasons: 1) numerical computing time, and 2) model limitations. The extension of the purely one-dimensional device to a large cross-section device assuming translational invariance and *perfectly isotropic scattering* has been implemented in the simulator QUEST.[56] The necessary CPU-time increases from 1/2 hour to 24 hours[§] for the calculation of a single point on a Current-Voltage-Characteristic. This increased consumption of CPU-time is due to the integration over all transverse momentum vectors at every spatially simulated point in the one-dimensional structure. An example simulation using the perfectly isotropic optical phonon scattering in large cross-section devices is given in Fig. 7.1. The perfectly isotropic scattering actually leads to phonon step instead of a phonon

---

[§]We have run QUEST on an IBM RISC 560 and an HP Apollo 730 workstation.

peak indicating the serious limitations of the model. This phonon step is due to the 2D-density of states in the quantum well, which does not turn off sharply and the isotropic randomization of momentum due to the isotropic scattering.
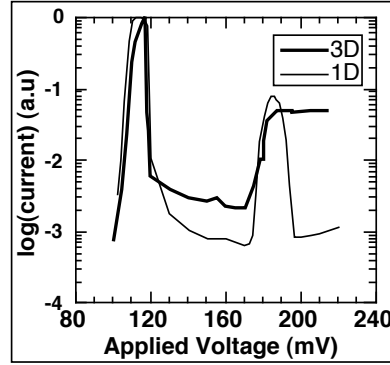
Figure 7.1 Limitations of the isotropic scattering model. Comparison of a purely one-dimensional calculation (thin line) and a three-dimensional calculation (thick line) with perfectly isotropic scattering. Perfect isotropy results in a phonon-step, rather than a phonon-peak.

We suggest to apply the knowledge how to treat a one-dimensional structure with very few spatial nodes to the understanding of large cross-section structures. This simplification would save significant computation time for the spatial coordinate resolution, which could be utilized to include more sophisticated scattering mechanisms into the model. The scattering model employed in the large cross-section structures implemented so far, assumes perfectly isotropic scattering and does not keep track of the transverse momentum quantum number in the large cross-section structure. We suggest to keep track of the total energy and the transverse momentum of the electron in the quantum well as good quantum numbers. The use of this basis set allows us to:

- monitor the filling of states with respect to longitudinal and transverse energy separately,
- analyze anisotropic scattering effects using more realistic models[153–156] for the electron-phonon-interaction in quantum confined devices.

The suggested scheme provides a framework for investigations on questions raised by experimentalists[157, 158] related to different phonon modes and hot electrons.

Phonon Modes and Scattering Rates

Experimental results in large cross-section GaAs-AlGaAs DBRTD's[48, 49, 51, 53, 54] show that that the phonon-spectrum in a DBRTD is different from that in Bulk GaAs. This can be understood as follows: The changing material parameters create an electro-dynamic environment for the atoms and electrons different from the bulk. Elastic and dielectric parameters change abruptly at the interfaces. Confined and interface phonon modes have been calculated[153–156] and the experiments[49, 51, 53, 54] are compatible with the theory of new phonon modes. The phonon-modes have been predicted to be *anisotropic*. Scattering Rates

for large cross-section structures have been calculated for DBRTD's using bulk and/or confined/interface phonons in a Fermi-Golden-Rule type approaches.[36, 51, 54, 107, 108, 123, 124, 155] These works have not considered the filling of the resonance states, which was shown to be essential in the understanding of purely-one-dimensional scattering processes in asymmetric DBRTD's. This omission has been realized and there is an expressed interest [157, 158] by experimentalists to obtain expressions/estimates for the degree of filling of the resonance.

Mathematical Implementation of Anisotropic Scattering

We will now introduce the scheme we suggest to solve the anisotropic scattering model. We will assume an infinitely large homogeneous cross-section (x-y-plane) and keep the scattering in the z-direction local. The final result of the new scheme will be, that we have the transverse momentum coordinates, k_x and k_y, everywhere in a 3-tupel of the form (k_x, k_y, E), where we used to have just one coordinate, the total energy, E. The calculation of the scattering rates, $\frac{\hbar}{\tau_n}$ and $\frac{\hbar}{\tau_p}$, involves now a summation over all transverse moments, k_x and k_y, since all transverse moments may be coupled by a matrix element $U_{\vec{q}}$ now. The matrix elements of the electron phonon interactions in an infinite cross section quantum well have been calculated theoretically.[153] We obtain as final prescription for the calculation of the scattering rates

$$\frac{\hbar}{\tau_n(z; k_x, k_y, E)} = 2\pi \int \frac{dk_x{}'}{2\pi} \int \frac{dk_y{}'}{2\pi} U_{\vec{k}-\vec{k}'} U_{\vec{k}'-\vec{k}} N_0\Big(z; k_x, k_y, E - \hbar\omega_{\vec{k}-\vec{k}'}\Big)$$
$$\Big(1 - f\Big(z; k_x, k_y, E - \hbar\omega_{\vec{k}-\vec{k}'}\Big)\Big) , \qquad (7.1a)$$

and

$$\frac{\hbar}{\tau_p(z; k_x, k_y, E)} = 2\pi \int \frac{dk_x{}'}{2\pi} \int \frac{dk_y{}'}{2\pi} U_{\vec{k}-\vec{k}'} U_{\vec{k}'-\vec{k}} N_0\Big(z; k_x, k_y, E + \hbar\omega_{\vec{k}-\vec{k}'}\Big)$$
$$f\Big(z; k_x, k_y, E + \hbar\omega_{\vec{k}-\vec{k}'}\Big) , \qquad (7.1b)$$

The Green's function equation that we need to solve for looks like:

$$\left(E - \frac{\hbar^2}{2m^*}\Big(k_x^2 + k_y^2\Big) - \frac{\hbar^2}{2m^*}\frac{d^2}{dz^2} - V(z) - \frac{i\hbar}{\tau_\Phi(z; k_x, k_y, E)}\right) G^R\Big(z, z{}'; k_x, k_y, E\Big)$$
$$= \delta\Big(z - z{}'\Big) . \qquad (7.2)$$

These equations and the corresponding transport equation can be solved in much the same way as the 1-D problems by discretization into three spatial nodes: emitter, well and collector. The transverse momentum dependence, k_x and k_y, can then be solved numerically.

7.1.2 Inter-Subband Scattering

In studying DBRTD's we are usually concerned with the tunneling processes through the first resonance which may create a negative differential resistance at a high enough bias. But a DBRTD may support a second resonance state if the barriers are sufficiently high and the well width not too thin. We can therefore have a second resonance current phenomenon in high bias. It is important to realize that the processes occurring in the tunneling of electrons in these two resonance conditions are very different. Inelastic scattering processes can be neglected in the case of tunneling through the first resonance since there are no scattering states available with lower energy to which electrons can scatter, if the energy range of the incident electrons is small. If this energy range is large, intra-band scattering processes may modify the electron distribution in the band.[91] Elastic scattering processes at the resonance energy have been shown to increase the resonance width without having an effect on the total current, if the range of incident electron energies is large compared to the resonance width.[114, 159]

The situation is different for tunneling through the second resonance, where inelastic processes cannot be neglected in any case, since final scattering states with lower energy may be available. Fig. 7.2 depicts a comparison of these two situations. The parabolas symbolize the two-dimensional character of the states in the quantum well indicating the total energy of an electron including the quantized energy in the z-direction (vertical offset) and the transverse energy (parabola). If the two subbands are separated by more than one optical phonon energy quantum, transverse momentum transfer is needed for an inter-subband transition.
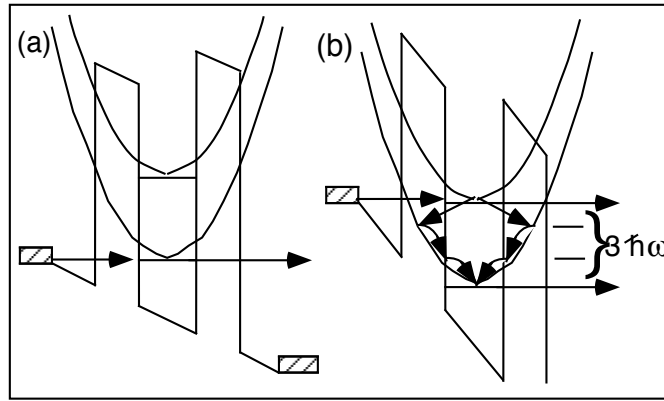
Figure 7.2 Importance of inter-subband scattering. Total energy of a single electron in two subbands. Parabolas indicate transverse energy. a) Bias for transmission through first longitudinal resonance. b) Bias for transmission through second longitudinal resonance. Arrows with vertical components indicate possible phonon scattering processes.

Tunneling through a second resonance and the filling of the lower resonance has been observed experimentally.[47, 50, 160–163] In one particular experiment,[163] the upper resonance was reported to be empty and the sequential current through the structure was estimated to be 50% of the total current. This again raises the question about the importance of the

scattering processes in the structure, the availability of states and the effect of a finite cross-section. While in the phonon peak problem a one dimensional treatment may be justified,[76] a *one-dimensional treatment for the inter-subband scattering seems to lack some important physics**.

So far we concerned ourselves with the electron-phonon interaction in single quantum well structures. We have indicated the interest in the understanding of the effect of scattering on the total current through the structure and the filling of the resonance states. We will now extend our view onto multiple quantum well structures which we suggest to be solved.

7.1.3   Tunneling through Triple-Barrier Structures

It is possible, as discussed in Chapter 6, to create several sets of barriers and wells in the growth process and create more that one quantum well in the structure. The growth of many sets of wells and barriers in series leads to a superlattice.[1–4] These structures have shown many potential device applications[1–3, 18, 21, 22] and are an active topic of current research. The DBRTD and the superlattice are two limits that bound the range of possible vertical device designs. The next logical extension from the Double-Barrier-Resonant-Tunneling-Diode is the Triple-Barrier-Resonant-Tunneling-Diode (TBRTD) (Fig. 7.3a) .
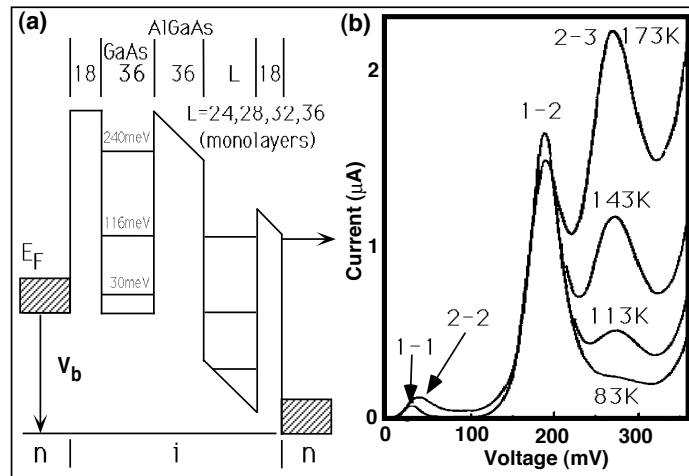
Figure 7.3 Experimental results of transport through a triple barrier structure. a) Typical conduction band profile of a triple barrier structure. b) Measured I-V-characteristic for different temperatures. The combinations x-y indicate the tunneling from state x in well number 1 to state y in well number 2. Figures are taken from Reference [165] (T. Nakagawa, T. Fujita, Y. Matsumoto, T. Kojima, and K. Ohta. *Appl. Phys. Lett.*, 51(6):445–447, 1987.).

The TBRTD has been predicted[166] and shown[167, 168] to have two enhanced performance features over the DBRTD:

---

*If we assume some "effective" phonon interaction that couples the two subbands in one dimension the problem can be solved analytically.[164]

1. the transmission peaks become more sharply defined,
2. the Peak-To-Valley-Ratio is enhanced.

These improvements are exciting for device engineers, since they increase the range of the output signal in the negative differential resistance region in analog devices and allows more reliable switching in digital devices.

The basic functionality of the TBRTD (Fig. 7.3) may be understood in a quite similar way to the DBRTD. In terms of our coherent picture, where we think of the TBRTD as the series combination of two bandpass filters. This implies that two device performance features may be enhanced. The coherent off-resonance transmission will be strongly reduced since 3 barriers are now in series.[169] This should reduce the availability of scattering states off-resonance which create the undesired valley current. It also implies that the main peak in the I-V-characteristic becomes more sharply defined. These effects have been analyzed theoretically in a calculation of transmission coefficients[166] and observed experimentally.[167, 168]

The possible improved device performance has prompted a whole series of work related to high bias application in GaAs/AlGaAs, SiGe/Si and InAs/GaSb structures involving electron, hole and inter-band tunneling processes.[165, 167, 168, 170–179]

The analogy of two bandpass filters in series is only of marginal usefulness in the analysis of the transmission coefficient and we will mention only in passing that the cross coupling between the wells may modify the states in both wells. See also Chapter 6 for a calculation of the eigen-states in a triple barrier structure. The well spectra have been studied theoretically[166] and very extensively experimentally using photoluminescence spectroscopy[180–184] with respect to well and middle barrier thickness.

Inelastic processes in TBRTD have been shown to be important[165, 185–188] and a very nice example[165] is given in Fig. 7.3. Resonant tunneling is shown to occur through several alignment combinations of states in the first and the second well. Note that the current flow indicated in Fig. 7.3a involves transport through a higher resonant state. This is similar to the problem addressed in the previous section and raises the same questions with respect to inelastic scattering processes to lower levels. Furthermore, notice that Fig. 7.3a indicates the potential drop across the device drops only over the second well indicating charge accumulation in the first well. These two issues again raise the question: How full is full? We suggest to analyze these structures with respect to the filling of the resonance states and the sequential currents through the structure.

We suggest to tackle the problem with a 1-D approach first. As in Ref. [76] we are thinking about a 1-D tight-binding chain where we now consider two special central sites rather than just a single one. We will not elaborate on this approach further, however we just indicate the similarity of the tight-binding phonon peak approach with the tight-binding triple barrier approach with Fig. (7.4).
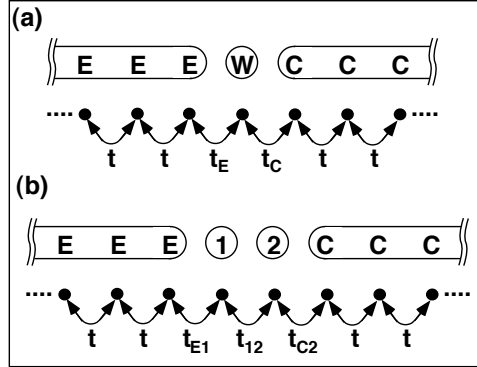
Figure 7.4 Comparison of two tight-binding chains. (a) one central site - phonon peak problem. (b) two central sites - triple barrier problem.

7.2 Small Cross-Section Structures

Chapters 5 and 6 deal with small cross-section resonance tunneling structures in which electron-electron and electron-phonon interactions strongly influence the transport. We will present several suggestions for future investigations in this direction of work. Technically speaking we can say that the hard problems in Chapter 5, such as the calculation of the occupation of *all* many-body states and non-adiabatic coupling to the leads, are the easy ones in Chapter 6, where assumption of near equilibrium and adiabatic transport were made. Vice versa the hard problems in Chapter 6, such as the calculation of the many-body spectrum and the coupling of the superposition states to the leads, are the easy ones in Chapter 5, where the assumption of a constant charging model was made. If we relax the simplifying assumptions in both problems several questions will be answered with respect to transport through artificial atoms and molecules. These suggestions will be given in Sections 7.2.1 and 7.2.2.

7.2.1 High Bias Transport through Single Quantum Dots

The hard job in the calculations of Chapter 5 were the solution for the occupation of *all* many-body states in the quantum dot and their coupling to the leads. The easier job was the construction of the many-body states using a simple constant charging model using the single-particle states which did not mix any of the orthogonal basis states. Different calculations[134–140] have been performed for many-body eigen-states in single quantum dots including more sophisticated charge interaction models as discussed in Section C.4 in Appendix C. The rate-equation approach that we use to determine the occupation of "every" possible many-body state in the limited set of states can be extended to more complicated many-body states. The determination of the "correct" many-body states is independent of the calculation of the occupation of these states. The coupling to the leads can be treated similarly to the treatment in Chapter 6, as long as the new many-body states can be represented in a limited, single-particle basis set. The tunneling rates, which lateral

quantum number dependent, can then be projected onto these new superposition states in terms of first order perturbation theory. The extension of the present model to include a better calculation of the many-body states in the single quantum dot would eliminate the model limitation that we discuss in Section C.4. The somewhat artificial distinction between charging and quantum effects would be eliminated.

7.2.2 High Bias Transport through Multiple Quantum Dots

The hard job in Chapter 6 was the calculation of the many-body eigen-states and their coupling to the leads. The bias applied to the structure was assumed to be small enough such that the occupation of the states in the artificial molecule could be assumed to be in equilibrium with the weakly coupled leads, which in turn is easily calculated in the grand canonical ensemble. The structure and the occupation of the eigen-states in the coupled dot system will change, if the bias is increased significantly. Calculations of the many-body eigen-states of a coupled quantum dot system at high bias have been calculated in Reference [189] including an extended, Coulomb-type potential, $\frac{e^2}{r}$. However, transport at high in the coupled dot system has not been calculated yet. We suggest a calculation of the occupation of the many-body based on the rate-equation approach applied in Chapter 5 and an improved calculation of the charging energies as discussed in Chapter 6 in Section 6.3.4.

7.2.3 Exact Many-Body Eigen-States and the Green's Function Formalism

Chapter 6 calculates the exact many-body states of a coupled dot system and proposes a possible experiment of conductance spectroscopy of this artificial molecule. Our research group has also considered finite chains[89] of coherently coupled artificial atoms in which we try to connect up to the work that has been performed on the infinite chain Hubbard Hamiltonian.[190,191] Similarly to the work presented in Chapter 6 we have solved the conductance through this chain of quantum dots using rate-equations[70] based on the exact eigen-states of the coupled system.

Solutions of the conductance problem in an infinite Hubbard[190,191] chain and and in a single-quantum dot[71] have been obtained using a Green's function formalism in which the single-particle excitations of the complicated many body-state have been considered. The Green function formalism is quite powerful in that methods exist[34,71,192] to calculate the single-particle excitation spectrum without the calculation of the all many-body states. These methods do, however, have severe limitations in that only small perturbations can be treated. The coherent coupling between the quantum dots and the intra-dot charging can be large, however, and the usage of mathematical methods like Wick's Theorem[192] which allow an easy calculation of the Green function cannot be applied.

Since we can calculate the full many-body spectrum, we can can construct the exact Many-Body Green Function (MBGF).[34] From this MBGF we can, for example, obtain the density of states in the device. We will show in the following paragraphs with two examples that the conductance is not strictly proportional to the density of states of a coupled dot

system, but it is proportional to an off-diagonal element of the MBGF. The conductance formula in terms the MBGF is different in structure than the Conductance formula which we used in our calculations in Chapter 6 and Reference [89]. The beauty (and the curse) of the Green's function formalism is that it projects the many-body states into a single-particle picture of single-particle excitations. Conductance is then treated with with the following point of view:

1) if a particle is injected at one site, i, of the coupled system, what is the probability extract an electron at another site, j, or

2) if an electron is extracted at one site, i, (a hole is created) of the coupled system, what is the probability to inject an electron into the vacant hole at another site, j.

The formalism we envision is depicted in Fig. 7.5. The basic element of the envisioned conductance calculation is the exact MBGF[34]

$$
\begin{aligned}
[G_{ij}(E)]_{k,N} &= \sum_{m,\alpha} \frac{\langle \Phi_{k,N} | a_{i,\alpha}^\dagger | \Phi_{m,N-1} \rangle \langle \Phi_{m,N-1} | a_{j,\alpha} | \Phi_{k,N} \rangle}{E - (\epsilon_{k,N} - \epsilon_{m,N-1})} \\
&+ \sum_{m,\alpha} \frac{\langle \Phi_{k,N} | a_{i,\alpha} | \Phi_{m,N+1} \rangle \langle \Phi_{m,N+1} | a_{j,\alpha}^\dagger | \Phi_{k,N} \rangle}{E - (\epsilon_{k,N} - \epsilon_{m,N+1})} \ , \quad (7.3a)
\end{aligned}
$$

$$
G(i,j) = \sum_{N,k} P(N,k) [G_{ij}(E)]_{k,N} \ , \quad (7.3b)
$$

where $|\Phi_{k,N}\rangle$ is the kth exact eigen-state of the coupled system in the subset of N particles[†]. The site and spin dependent electron creation and destruction operators are indicated with $a_{i,\alpha}^\dagger$ and $a_{i,\alpha}$, respectively. The equilibrium occupation of the state indexed with $\{k, N\}$ is calculated with Eq. 6.3 and depends on the Fermi-energy in the leads, E_F. The conductance
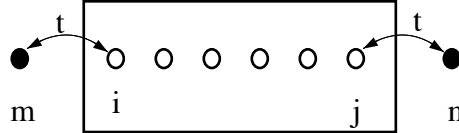
Figure 7.5 Proposed structure of a conductance formula based on Green's functions. The single-electron channel extends from subband m in the emitter to site i in the artificial molecule, extraction of an electron on site j in the artificial molecule and transmission into subband n in the collector lead. The injection at site i and extraction at site j is treated by the Green function $G^R(i,j)$.

formula we envision is now dependent on the overall coupling from mode m in one lead to mode n in the other lead by some weak coupling t (see Fig. 7.5).

$$
T_{m,n} = \hbar^2 v_m v_n |t(m,i) G(i,j) t(j,n)|^2 \quad (7.4)
$$

$$
G = \sum_{m,n} T_{m,n} \quad (7.5)
$$

[†]See Chapter 6 and Appendix D for details.

For out numerical evaluation of the Green's function we have included a small imaginary part, η, in the denominators of Eq. 7.3a to account for the finite lifetime of the excitations due to the coupling to the leads. We define the density of states as the trace over all sites

$$N_0(E, E_F) = -\frac{1}{\pi} Im \left\{ \sum_i G(i,i) \right\} \qquad (7.6)$$

and we will show that the conductance as calculated with Eq. 6.2 is not proportional to this density of states of the coupled system in two examples. However, one quantity,

$$G_{LR}(E, E_F) = |G(i{=}leftsite, j{=}rightsite)|^2 \qquad (7.7)$$

derived from Eq. (7.3) will be shown to be proportional to the conductance calculated with Eq. (6.2). The physical differences between the three quantities conductance (Eq. (6.2)), G, density of states (Eq. (7.6)), N_0 and connecting Green's function (Eq. (7.7)), G_{LR}, become apparent if some asymmetry in the eigen-states of the coupled system is introduced. In the following we will consider two examples indicating these physical differences:
1) A double dot system with detuning, as discussed in Section 6.3.2.
2) A finite chain of quantum dots with and without inter-dot charging as discussed in Reference [89].

Double Dot System with Detuning

We have discussed the conductance spectrum and amplitude of a double dot system given an inter-dot detuning of the single-particle eigen-energy in Section 6.3.2 in detail. We will now revisit this example and compare the calculated spectrum (see Fig. 6.4) to the spectrum of the density of states, $N_0(E_F, E_F)$, as defined by Eq. 7.6, and the Green's function G_{LR}, as defined by Eq. 7.7, evaluated at the Fermi energy (Fig. 7.6). The density of states does exhibit four peaks, since four electrons can be added to the quantum dot, as a function of Fermi energy. The locus of the density of states peaks corresponds to the locus of the conductance peaks (Fig. 7.6a), Their amplitudes (Fig 7.6c), however, do not correspond to the calculated conductance peaks (Fig. 7.6b). The density of states only includes information about the presence of four quantum states in the double dot system. These states may be filled from the left of the right lead, however this filling of the states does not reveal any information about the conductance through the system. We have discussed the uniform height of the steps (Fig. 6.2) in the number of electrons as a function of Fermi energy in detail in Section 6.3.2 and pointed out the non-uniformity of the conductance peak amplitudes. The density of states will always have four peaks, indicating electronic states for four electrons in the quantum dot system, the amplitude of the corresponding conductance peaks however is not proportional to the density of states. The off-diagonal Green's function quantity, G_{LR} in Figure 7.6d, however appears to present the general behavior of the conductance with detuning properly. It includes the injection of an electron at one end of the chain and the extraction of an electron at the other end of the chain, which effectively transports an electron[‡] through the chain.

[‡]A similar argument can be made for holes.
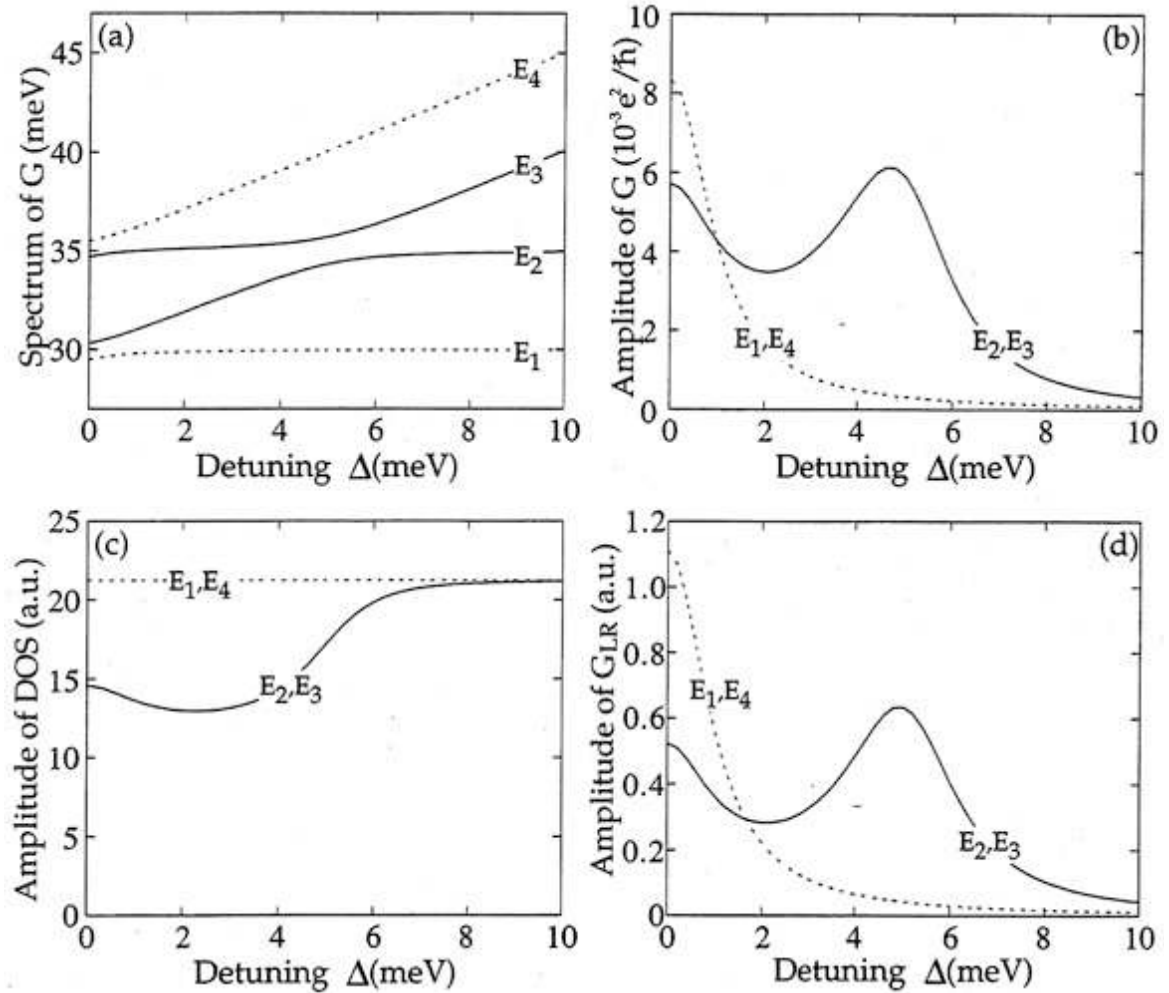
Figure 7.6 Two coherently coupled quantum dots under the influence of detuning (see Section 6.3.2). The model parameters are $\epsilon = 30meV$, $U = 5meV$, and $t = 0.5meV$. Conductance peak spectrum (a) and amplitudes (b) as a function of detuning, Δ, calculated with Eq. (6.2). (c) Amplitude of density of states (Eq. (7.6)), N_0, evaluated at the Fermi energy, E_F, as a function of detuning, Δ. (d) Amplitude of connecting Green's function (Eq. (7.7)), G_{LR}, evaluated at the Fermi energy, E_F, as a function of detuning, Δ.

Finite Chain of Quantum Dots

In Reference [89] we evaluate the linear response conductance through a finite chain of coherently coupled quantum dots. We show that two bands develop in the conductance spectrum, separated by the intra-dot charging energy, U, as more and more quantum dots are added[§]. For convenience we show here in Figure 7.7 an example calculation for 5 quantum dots with similar parameters[¶] as we have used in Chapter 6.

We elaborate in Reference [89] that the introduction of an inter-dot charging, W, modifies the symmetry of electrons and holes in the many-body states significantly. With a small inter-dot charging, $W = 1 meV$, electrons "prefer" to be on the left-most or right-most site in the quantum dot chain, since these two sites only involve charge interaction with one neighboring site, whereas all interior sites involve a charge interaction with two sites (a left and a right neighbors). This effect becomes stronger as the quantum dot fills up more and
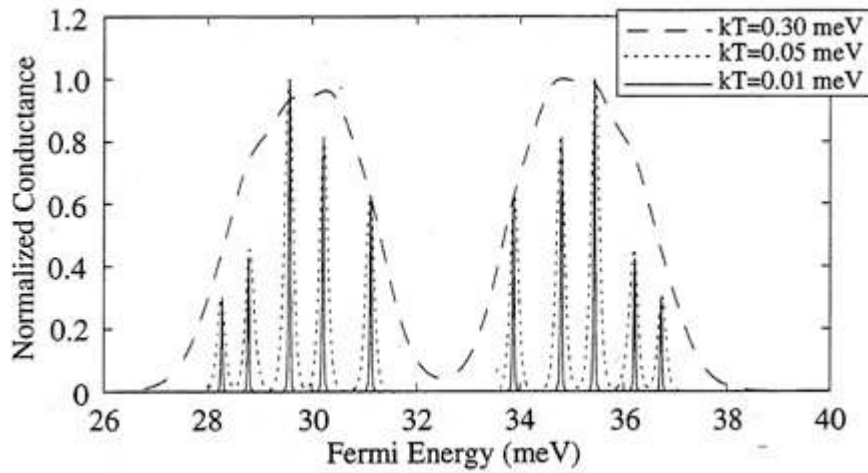
Figure 7.7 Conductance spectrum for a finite chain of 5 quantum dots. Conductance is normalized to the peak value for three different temperatures, $k_B T = 0.01, 0.05, 0.30 meV$. Two bands separated by the intra-dot charging energy, U, form (compare to Fig 6.2).

more, i.e. when the Fermi energy is raised. The probability to find a hole on an outer-most site becomes smaller and smaller as the number of electrons in the quantum dot increases. The conductance peaks therefore decrease with an increased number of electrons in the dot. The symmetry of the conductance spectrum in Figure 7.7 is broken and inter-dot charging modifies the conductance spectrum significantly (Fig 7.8a). Figure 7.8b depicts the density of states, N_0, evaluated at Fermi energy for a temperature of $k_B T = 0.01 meV$. The density of states, N_0, does not exhibit the same asymmetry of the conductance peaks depicted in Figure 7.8a. The connecting Green's function, G_{LR}, however, does exhibit the same asym-

---

[§]We consider quantum dot chains consisting of $2 \ldots 6$ quantum dots.

[¶]Intra-dot charging, $U = 5meV$, inter-dot coupling, $t = 1meV$, and single particle eigen-energy of each site, $\epsilon = 30meV$.

metry as the conductance. The arguments for the failure of the density of states to describe the conductance peak amplitudes are the same here as the ones presented in the previous subsection.

Conclusions for the Green's Function Model

Given these brief example calculations of the density of states, N_0, in the coupled quantum dot system we can conclude that the the density of states is not the quantity we are interested in with respect to the conductance through the coupled system. Usage of the connecting Green's function, G_{LR}, appears to describe the transport physics of the coupled dot system similarly as the rate-equation formalism used in Chapter 6 and Reference [89]. We suggest here to analyze the scheme to calculate conductance using this Green's function formalism further to possibly connect it to some easier single-particle approach, which is not based on perturbation.

Note that this new Green's function approach takes the average of the occupation of the many body states into account in a different order than the rate equation approach used in Chapter 6 and Reference [89]. Cryptically denoting this state average as $\langle \, \rangle$ we state here briefly that $\left| \left\langle G^R \right\rangle \right|^2 \neq \left\langle \left| G^R \right|^2 \right\rangle$ which may be comparable to the inclusion of inelastic scattering in Section 6.3.5.
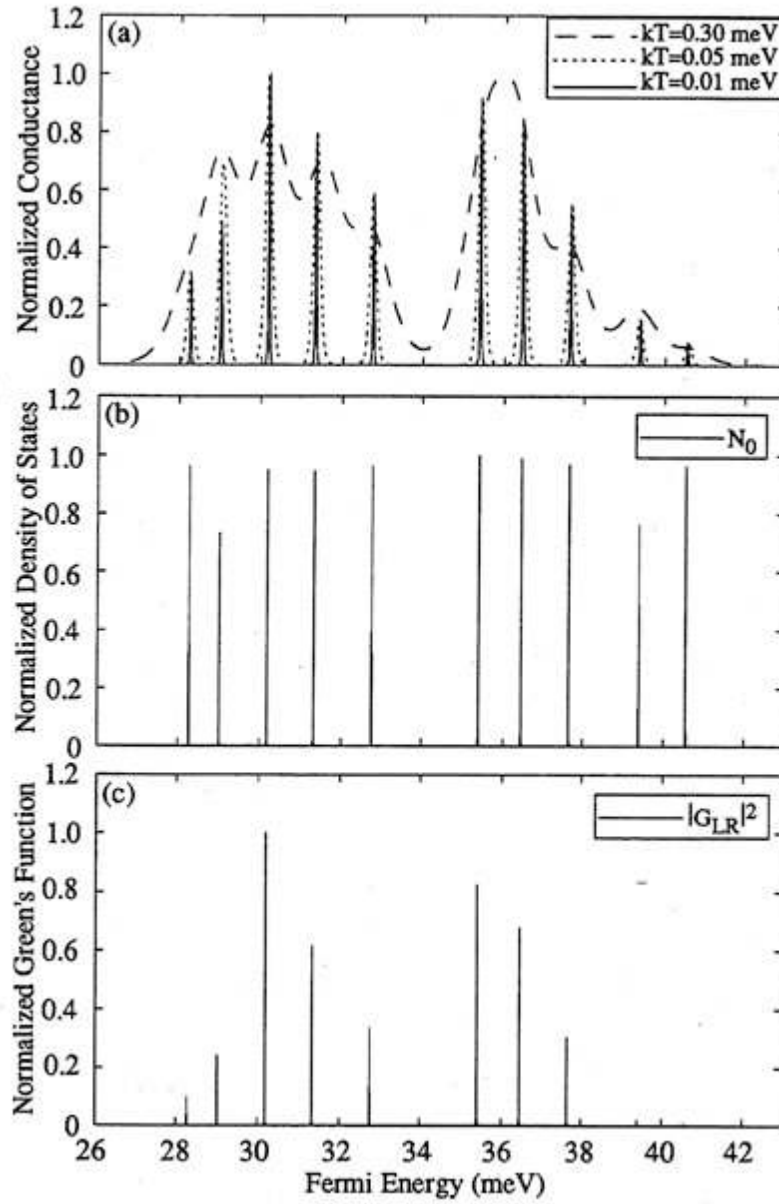
Figure 7.8 Conductance spectrum, density of states and connecting Green's function for a finite chain of
5 quantum dots including inter-dot charging. (a) Conductance is normalized to the peak value
for three different temperatures, $k_B T = 0.01, 0.05, 0.30 meV$. (b) Density of states at the
Fermi energy does not exhibit the asymmetry in the conductance peaks $(k_B T = 0.01 meV)$.
(c) Connecting Green's function, G_{LR}, evaluated at the Fermi energy exhibits the correct
proportionality $(k_B T = 0.01 meV)$.

List of References

[1] Frederico Capasso. Bandgap and interface engineering for advanced electronic and photonic devices. *MRS Bulletin*, June:23–9, 1991.

[2] Frederico Capasso, Khalid Mohammed, and Alfred Y. Cho. Resonant tunneling through double barriers, perpendicular quantum transport phenomena in superlattices, and their device applications. *IEEE Journal of Quantum Electronics*, QE-22(9):1853–69, 1986.

[3] Leo Esaki. A bird's eye view on the evolution of semiconductor superlattices and quantum wells. *IEEE Journal of Quantum Electronics*, QE-22(9):1611–24, 1986.

[4] G. Bastard and J. A. Brum. Electronic states in semiconductor heterostructures. *IEEE Journal of Quantum Electronics*, QE-22(9):1625–44, 1986.

[5] S. Datta and M. J. McLennan. Quantum transport in ultrasmall electronic devices. *Reports on Progress in Physiscs*, 53(8):1003, 1990.

[6] C.W. Beenakker and H. van Houten. *Solid State Physics*, volume 44. Academic Press, 1991.

[7] Marc A. Kastner. The single-electron transistor. *Rev. Mod. Phys.*, 64(3):849, 1992.

[8] T. C. L. G. Sollner, E. R. Brown, J. R. Söderström, T. C. McGill, C. D. Parker, and W. D. Goodhue. High-frequency oscillators based on resonant tunneling. In L. L. Chang, E. E. Mendez, and C. Tejedor, editors, *Resonant Tunneling in Semiconductors*, pages 487–494, New York, 1991. Plenum Press.

[9] Alan C. Seabaugh, Yung-Chung Kao, and Han-Tzong Yuan. Nine-state resonant tunneling diode memory. *IEEE Electron Device Letters*, 13(9):479–481, 1992.

[10] Yan Kuin Su, Ruey Lue Wang, Ching Hwang Su, and Hann Huei Tsai. The current-voltage characteristics of a delta-doped triple-barrier switch. *Jap. J. Appl. Phys.*, 31(1):30–34, 1992.

[11] G. Abstreiter A. Köck, E. Gornick, G. Böhm, M. Walther, and G. Weimann. Double wavelength selective GaAs/AlGaAs infrared detector device. *Appl. Phys. Lett.*, 60(16):2011–2013, 1992.

[12] D. A. B. Miller, D. S. Chemla, T. C. Damen, A. C. Gossard, W. Wiegmann, T. H. Wood, and C. A. Burrus. Novel hybrid optically bistable switch: The quantum well self-electro-optic effect device. *Appl. Phys. Lett.*, 45(1):13–15, 1984.

[13] T. H. Wood, C. A. Burrus, D. A. B. Miller, D. S. Chemla, T. C. Damen, A. C. Gossard, and W. Wiegmann. 131 ps optical modulation in semiconductor multiple quantum wells (mqw's). *IEEE Journal of Quantum Electronics*, QE-21(2):117–118, 1985.

[14] P. Li Kam Wa, J. E. Sitch, N. J. Mason, J. S. Roberts, and P. N. Robson. All optical multiple-quantum-well waveguide switch. *Electronics Letters*, 21(1):26–27, 1985.

[15] D. A. B. Miller, D. S. Chemla, T. C. Damen, T. H. Wood, C. A. Burrus, A. C. Gossard, and W. Wiegmann. Optical-level shifter and self-linearized optical modulator using a quantum-well self-electro-optic device. *Optics Letters*, 9(12):567–569, 1984.

[16] F. Beltram, F. Capasso, D. L. Sivco, A. L. Hutchinson, S. G. Chu, and A. Y. Cho. *Phys. Rev. Lett.*, 64:3167, 1990.

[17] H. C. Liu, M. Buchanan, G. C. Aers, and Z. R. Wasilewski. Single quantum well intersubband infrared detector using GaAs/AlGaAs asymmetrical double barrier structures. *Semicond. Sci. Technol.*, 4:C124–C127, 1991.

[18] G. Abstreiter, M. Besson, R. Heinrich, A. Kock, W. Schlapp, G. Weimann, and R. Zachai. Intersubband absorption and real space electron transfer in GaAs quantum wells. In L. L. Chang, E. E. Mendez, and C. Tejedor, editors, *Resonant Tunneling in Semiconductors*, pages 505–513, New York, 1991. Plenum Press.

[19] J. W. Choe, G. U. Perera, M. H. Francombe, and D. D. Coon. Estimates of infrared intersubband emission and its angular dependence in GaAs/AlGaAs multiquantum well structures. *Appl. Phys. Lett.*, 59(1):54–56, 1991.

[20] B. O, J. W. Choe, M. H. Francombe, K. M. S. V. Bandara, D. D. Coon, Y. F. Lin, and W. J. Takei. Long-wavelength infrared detection in a kastalsky-type superlattice structure. *Appl. Phys. Lett.*, 57(5):503–505, 1990.

[21] Q. Hu and S. Feng. Feasibility of far-infrared lasers using multiple semiconductor quantum wells. *Appl. Phys. Lett.*, 59(23):2923–2925, 1991.

[22] A. Katalsky, V. J. Goldman, and J. H. Abeles. Possibility of infrared laser in a resonant tunneling structure. *Appl. Phys. Lett.*, 59(21):2636–2638, 1991.

[23] W. Chen and T. G. Andersson. Intersubband transitions for differently shaped quantum wells under an applied electic field. *Appl. Phys. Lett.*, 60(13):1591–1593, 1992.

[24] Bo Su, J. V. Goldman, and J. E. Cunningham. Single-electron tunneling in nanometer-scale double-barrier heterostructure devices. *Phys. Rev. B*, 46(12):7644–55, 1992.

[25] M. Tewordt, L. Martin-Moreno, J. T. Nicholls, M. Pepper, M. J. Kelly, J. V. Law, D. A. Ritchie, J. E. F. Frost, and G. A. C. Jones. Single-electron tunneling and coulomb charging effects in asymmetric double-barrier resonant-tunneling diodes. *Phys. Rev. B.*, 45(24):14407–10, 1992.

[26] Bo Su, J. V. Goldman, and J. E. Cunningham. Observation of single-electron charging in double-barrier herterostructures. *Science*, Jan(255):313–5, 1992.

[27] J. V. Goldman, Bo Su, and J. E. Cunningham. Single-electron resonant tunneling through quantum dots. In Wiley P. Kirk and Mark A. Reed, editors, *Nanostructures and Mesoscopic Systems*, pages 173–82, Boston, 1991. Academic Press.

[28] M. Tewordt, L. Martin-Moreno, J. V. Law, M. J. Kelly, D. A. Ritchie, J. E. F. Frost, M. Pepper, and G. A. C. Jones. Fine structure in the current-voltage characteristics of a 200nm diameter AlGaAs-GaAs resonant tunneling diode in high magnetic fields. In Wiley P. Kirk and Mark A. Reed, editors, *Nanostructures and Mesoscopic Systems*, pages 217–23, Boston, 1991. Academic Press.

[29] Bo Su, J. V. Goldman, M. Santos, and M. Shayegan. Resonant tunneling in submicron double-barrier heterostructures. *Appl. Phys. Lett.*, 58(7):747–9, 1991.

[30] M. A. Reed, J. N. Randall, R. J. Aggarwal, R. J. Matyi, T. M. Moore, and A. E. Wetsel. Observation of discrete electronic states in a zero-dimensional semiconductor nanostructure. *Phys. Rev. Lett.*, 60(6):535–7, 1988.

[31] Seigo Tarucha, Yoshiro Hirayama, Tadashi Saku, and Tatsuya Kimura. Resonant tunneling through one– and zero–dimensional states constricted by $Al_xGa_{(1-x)}As/GaAs/Al_xGa_{(1-x)}As$ heterojunctions and high–resistance regions induced by focused *ga* ion-beam implantation. *Phys. Rev. B*, 41(8):5459–62, 1990.

[32] S. Tarucha, Y. Tokura, and Y. Hirayama. Resonant tunneling of three-dimensional electrons into degenerate zero-dimensional levels. *Phys. Rev. B*, 44(24):13815–8, 1991.

[33] E. J. van Loenen, D. Dijkkamp, A. J. Hoeven, J. M. Lenssinck, and J. Dieleman. *Appl. Phys. Lett.*, 55:1312, 1989.

[34] Attila Szabo and Neil S. Ostlund. *Modern Quantum Chemistry:Introduction to Advanced Electronic Structure Theory*. Macmillan, New York, 1982.

[35] R. F. Pierret. *Advanced Semiconductor Fundamentals*. Addison-Wesley, New York.

[36] Mark Lundstrom. *Fundamentals of Carrier Transport*. Addison-Wesley, New York, 1992.

[37] S. E. Laux, M. V. Fischetti, and D. J. Frank. Monte carlo analysis of semiconductor devices, the damokles program. *preprint.*

[38] Rolf Landauer. *IBM J. Res. Dev.*, 32:306, 1988.

[39] Y. Imry. *Directions in Condensed Matter Physics.* World Scientific, Singapore, 1986.

[40] Markus Büttiker. *Phys. Rev. Lett.*, 57:1961, 1986.

[41] Daniel S. Fisher and Patrick A. Lee. Relation between conductivity and transmission matrix. *Phys. Rev. B*, 23(12):6851–4, 1981.

[42] Supriyo Datta. *Quantum Phenomena.* Addison-Wesley, New York, 1989.

[43] L. L. Chang, E. E. Mendez, and C. Tejedor, editors. *Resonant Tunneling in Semiconductor Physics and Applications.* Plenum, New York, 1991.

[44] J. S. Blakemore. Semiconducting and other major properties of gallium arsenide. *J. Appl. Phys.*, 53(10):R123–R181, 1982.

[45] Sadao Adachi. GaAs, AlAs and $Al_xGa_{(1-x)}As$: Material parameters for use in research and device applications. *J. Appl. Phys.*, 58(3):R1–R29, 1985.

[46] A. Zaslavsky, J. V. Goldman, D. C. Tsui, and J. E. Cunningham. Resonant tunneling and intrinsic bistability in asymmetric double-barrier heterostructures. *Appl. Phys. Lett.*, 53(15):1408–1410, 1988.

[47] E. S. Alves, L. Eaves, M. Henini, O. H. Hughes, M. L. Leadbeater, F. W. Sheard, G. A. Toombs, G. Hill, and M. A. Pate. Observation of intrinsic bistability in resonant tunneling devices. *Electronics Letters*, 24(18):1190–1191, 1988.

[48] J. V. Goldman, D. C. Tsui, and J. E. Cunningham. Evidence fo lo-phonon-emission-assisted tunneling in double-barrier heterostructures. *Phys. Rev. B*, 36(14):7635–7637, 1987.

[49] M. L. Leadbeater, E. S. Alves, L. Eaves, M Henini, and O. H. Hughes. Magnetic field studies of elastic scattering and optic-phonon emission in resonant-tunneling devices. *Phys. Rev. B*, 39(5):3438–3441, 1989.

[50] M. S. Skolnick, D. G. Hayes, P. E. Simmonds, A. W. Higgs, G. W. Smith, H. J. Hutchinson, and C. R. Whitehouse. Electronic processes in double barrier resonant tunneling structures studied by photoluminescence spectroscopy in zero and finite magnetic fields. *Phys. Rev. B*, 41(15):10754–10766, 1990.

[51] P. J. Turley, C. R. Wallis, S. W. Teitsworth, W. Li, and P. K. Bhattacharya. Tunneling measurements of symmetric-interface phonons in GaAs/AlAs double-barrier structures. *Phys. Rev. B*, 47(19):12640–8, 1993.

[52] G. S. Boebinger, A. F. J. Levi, S. Schmitt-Rink, A. Passner, L. N. Pfeiffer, and K. W. West. Direct observation of two-dimensional magnetopolarons in a resonant tunneling junction. *Phys. Rev. Lett.*, 65(2):235–238, 1990.

[53] J. G. Chen, C. H. Yang, M. J. Yang, and R. A. Wilson. Observation of two-dimensional resonant magnetopolarons and phonon-assited resonant tunneling in double-barrier heterostructures. *Phys. Rev. B*, 43(5):4531–4533, 1991.

[54] P. J. Turley and S. W. Teitsworth. Effects of localized phonon modes on magnetotunneling spectra in double-barrier structures. *Phys. Rev. B*, 44(23):12959–12963, 1991.

[55] V. J. Goldman, D. C. Tsui, and J. E. Cunningham. Observation of intrinsic bistability in resonant-tunneling structures. *Phys. Rev. Lett.*, 58(12):1256–1259, 1987.

[56] Gerhard Klimeck, Roger K. Lake, Michael J. McLennan, and Supriyo Datta. Quest: User's manual. Technical Report TR-EE 93-17, School of Electrical Engineering, Purdue University, West Lafayette, IN 47907-1285, May 1993.

[57] L. V. Keldysh. *Sov. Phys. JETP*, 20:1018–1026, 1965.

[58] L. P. Kadanoff and G. Baym. *Quantum Statistical Mechanics*. Benjamin / Cummings, Reading, 1962.

[59] D. C. Langreth. *Linear and Non-linear Electron Transport in Solids*, volume 17. Plenum, New York, 1976.

[60] P. Danielewicz. *Annals of Physics*, 152:239–304, 1984.

[61] G. D. Mahan. *Physics Reports*, 145:251, 1987.

[62] J. Rammer and H. Smith. *Rev. Mod. Phys.*, 58:329–359, 1986.

[63] F. S. Khan, J. H. Davies, and J. W. Wilkins. *Phys. Rev. B.*, 36:2578, 1987.

[64] S. Datta. *J. Phys.: Condensed Matter*, 2:8023–8052, 1990.

[65] Supriyo Datta. *Electronic Transport in Mesoscopic Systems or Current Flow in Small Conductors*. Cambridge University Press, 1994. preprint.

[66] F. W. Sheard and G. A. Toombs. Space-charge buildup and bistability in resonant-tunneling double-barrier structures. *Appl. Phys. Lett.*, 52(15):1228–1230, 1988.

[67] Michael J. McLennan, Supriyo Datta, and Mark S. Lundstrom. Importance of space-charge effects in resonant tunneling devices. *Appl. Phys . Lett.*, 50:612, 1987.

[68] W. Pötz. Self-consistent model of transport in quantum in quantum well tunneling structures. *J. Appl. Phys.*, 66(6):2458–66, 1989.

[69] D. V. Averin, A. N. Korotkov, and K. K. Likharev. Theory of single-electron charging of quantum wells and dots. *Phys. Rev. B*, 44(12):6199–6211, 1991.

[70] C. W. J. Beenakker. Theory of coulomb-blockade oscillations in the conductance of a quantum dot. *Phys. Rev. B*, 44(4):1646–1656, 1991.

[71] Yigal Meir, Ned S. Wingreen, and Patrick A. Lee. Transport through a strongly interacting electron system: Theory of periodic conductance oscillations. *Phys. Rev. Lett.*, 66(23):3048–51, 1991.

[72] L. Y. Chen and C. S. Ting. Coulomb staircase in the i–v characteristic of an ultrasmall double-barrier resonant-tunneling structure. *Phys. Rev. B*, 44(11):5916–8, 1991.

[73] U. Meirav, M. A. Kastner, and S. J. Wind. Single-electron charging and periodic conductance resonances in GaAs nanostructures. *Phys. Rev. Lett.*, 65(6):771–774, 1990.

[74] Wingreen. *APS March Meeting Presentation*, 1992.

[75] E. B. Foxman, P. L. McEuen, U. Meirav, Ned S. Wingreen, Yigal Meir, Paul A. Belk, N. R. Belk, and M. A. Kastner. The effects of quantum levels on transport through a coulomb island. *Phys. Rev. B*, 47(15):10020–3, 1993.

[76] Roger Lake, Gerhard Klimeck, and Supriyo Datta. Rate equations from the keldysh formalism applied to the phonon peak in resonant tunneling diodes. *Phys. Rev. B*, 47(11):6427–38, 1993.

[77] Roger Lake, Gerhard Klimeck, M. P. Anantram, and Supriyo Datta. Rate equations for the phonon peak in resonant tunneling structures. *Phys. Rev. B*, 48(20):15132–7, 1993.

[78] Roger Lake, Gerhard Klimeck, and Supriyo Datta. Barrier asymmetry and the phonon peak in double barrier resonant tunneling structures. In *Bulletin of the American Physical Society*, volume 38, Seattle, WA, March 1993.

[79] Roger Lake, Gerhard Klimeck, Michael J. McLennan, and Supriyo Datta. A quantum device simulator based on the non-equilibrium green function equations of keldysh, kadanoff, and baym. In *Proceedings of the International Workshop on Computational Electronics, Urbana-Champaign*, pages 265–8, Urbana-Champaign, 1992. Beckmann Institute.

[80] Roger Lake, Gerhard Klimeck, and Supriyo Datta. Rate equations from the keldysh formalism applied to the phonon peak in resonant tunneling diodes. In *Second International Symposium on "New Phenomena in Mesoscopic Structures", Dec 7-11, Hawaii*, 1992.

[81] Gerhard Klimeck, Roger Lake, and Supriyo Datta. The phonon peak in resonant tunneling diodes. In *submitted to The Electrochemical Society*, San Francisco, May 1994.

[82] Gerhard Klimeck, Supriyo Datta, and Garnett Bryant. Elastic and inelastic scattering in quantum dots in the quantum blockade regime. *submitted to Phys. Rev. B.*, 1994.

[83] Gerhard Klimeck, Roger Lake, and Supriyo Datta. Effects of inelastic scattering on the i–v–staircase in the coulomb blockade regime. In *Bulletin of the American Physical Society*, volume 38, Seattle, WA, March 1993.

[84] Gerhard Klimeck, Roger Lake, and Supriyo Datta Garnett Bryant. High bias transport through quantum dots. In *Submitted to The Electrochemical Society*, San Francisco, May 1994.

[85] Gerhard Klimeck, Roger Lake, Supriyo Datta, and Garnett Bryant. High bias transport through quantum dots. In *To be presented to the Engineering Foundation*, Hawaii, April 1994.

[86] Gerhard Klimeck, Roger Lake, Supriyo Datta, and Garnett Bryant. High bias transport in quantum dots. In *submitted to the American Physical Society*, Pittsburg, March 1994.

[87] Gerhard Klimeck, Guanlong Chen, and Supriyo Datta. Conductance spectroscopy in coupled quantum dots. *submitted to Phys. Rev. B.*, 1993.

[88] Gerhard Klimeck, Guanlong Chen, and Supriyo Datta. Conductance spectroscopy in coupled quantum dots. In *submitted to American Physical Society*, Pittsburg, March 1994.

[89] Guanlong Chen, Gerhard Klimeck, and Supriyo Datta. Resonant tunneling through quantum-dot arrays. *submitted to Phys. Rev. Lett.*, 1993.

[90] Michael J. McLennan and Supriyo Datta. Sequal: A guide for the user. Technical Report TR-EE 89-17, School of Electrical Engineering, Purdue University, West Lafayette, IN 47907-1285, March 1989.

[91] Roger K. Lake and Supriyo Datta. Nonequilibrium green's-function method applied to double-barrier resonant-tunneling diodes. *Phys. Rev. B*, 45(12):6670–6685, 1992.

[92] Michael J. McLennan, Yong Lee, and Supriyo Datta. *Phys. Rev. B*, 43:13846, 1991.

[93] Roger K. Lake and Supriyo Datta. High-bias quantum electron transport. *Superlattices and Microstructures*, 11(1):83–7, 1992.

[94] Roger K. Lake and Supriyo Datta. Energy balance and heat exchange in mesoscopic systems. *Phys. Rev. B*, 46(8):4757–4763, 1992.

[95] Yong Lee, Michael J. McLennan, and Supriyo Datta. Anomalous R_{xx} in the quantum hall regime due to impurity-bound states. *Phys. Rev. B*, 43(17):14339, 1991.

[96] Yong Lee, Michael J. McLennan, Gerhard Klimeck, Roger K. Lake, and Supriyo Datta. Quantum kinetic analysis of mesoscopic systems: Linear response. *Superlattices and Microstructures*, 11(2):137–140, 1991.

[97] Roger K. Lake. *Physics and Modeling of Quantum Electron Transport in Semiconductor Nanostructures*. PhD thesis, Purdue University, School of Electrical Engineering, 1992.

[98] H. U. Baranger and A. D. Stone. *Phys. Rev. Lett.*, 63:414, 1989.

[99] A. Szafer and A. D. Stone. *Phys. Rev. Lett.*, 62:300, 1989.

[100] Markus Büttiker. *Phys. Rev. B*, 38:9375, 1988.

[101] A. D. Stone and A. Szafer. *IBM J. Res. Dev.*, 32:384, 1988.

[102] H. U. Baranger and A. D. Stone. *Phys. Rev. B*, 40:8169, 1989.

[103] P. G. N. de Vegvar, G. Timp, M. P. Mankiewich, J. E. Cunningham, and R. E. Howard. *Phys. Rev. B*, 38:4326, 1988.

[104] R. A. Webb, S. Washburn, and C. P. Umbach. *Phys. Rev. B*, 37:8455, 1988.

[105] W. R. Frensley. *Phys. Rev. B*, 36:1570, 1987.

[106] N. C. Kluksdahl, A. M. Kriman, D. K. Ferry, and C. Ringhofer. *Phys. Rev. B*, 39:7720, 1989.

[107] B. G. R. Rudberg. Optical phonons in resonant tunneling. *Semicond. Sci. Technol.*, 5:328–332, 1990.

[108] F. A. Riddoch and B. K. Ridley. On the scattering of electrons by polar optical phonons in quasi-1d quantum wells. *J. Phys. C: Solid State Phys.*, 16:6971–6982, 1983.

[109] N. S. Wingreen, K. W. Jakobsen, and J. W. Wilkins. Resonant tunneling with electron-phonon interaction: An exactly solvable model. *Phys. Rev. Lett.*, 61(12):1396–1399, 1988.

[110] W. Cai, T. F. Zheng, P. Hu, B. Yudanin, and M. Lax. Model of phonon-associated electron tunneling through a semiconductor dounble barrier. *Phys. Rev. Lett.*, 63(4):418–421, 1988.

[111] F. Chevoir and B. Vinter. Calculation of phonon-assited tunneling and valley current in a double barrier diode. *Appl. Phys. Lett.*, 55(18):1859–1861, 1989.

[112] F. Chevoir and B. Vinter. Resonant and scattering-assited magnetotunneling. In L. L. Chang, E. E. Mendez, and C. Tejedor, editors, *Resonant Tunneling in Semiconductors*, pages 255–263, New York, 1991. Plenum Press.

[113] F. Chevoir and B. Vinter. Scattering processes, coherent and incoherent transport in resonant tunneling structures. In L. L. Chang, E. E. Mendez, and C. Tejedor, editors, *Resonant Tunneling in Semiconductors*, page 201, New York, 1991. Plenum Press.

[114] M. Jonson and Anna Grincwajg. Effect of inelastic scattering on resonant and sequantial tunneling in double barrier heterostructures. *Appl. Phys. Lett.*, 51(21):1729–1731, 1987.

[115] Antti-Pekka Jauho. Numerical simulation of resonant tunneling in the presence of inelastic processes. *Phys. Rev. B*, 41(17):12327–12329, 1990.

[116] Per Hyldegaard and Antti-Pekka Jauho. Elasic and inelastic resonant tunneling in narrow-band systems: Application to transport in minibands of semiconductor superlattices. *J. Phys.: Condens. Matter*, 2:8725–8729, 1990.

[117] J. A. Stovneng, E. H. Hauge, P. Lipavsky, and V. Spicka. Tight-binding approach to resonant tunneling with electron-phonon coupling. *Phys. Rev. B*, 44(24):13595–13602, 1991.

[118] X. J. Lu and N. J. Horing. Tunneling current through a resonant structure. *preprint, Stevens Institute of Engineering Physics*, 1991.

[119] M. Jonson. Quantum-mechanical resonant tunneling in the presence of a boson field. *Phys. Rev. B*, 39(9):5924–5933, 1989.

[120] J. W. Gadzuk. Inelastic resonance scattering, tunneling, and desorption. *Phys. Rev. B*, 44(24):13466–13477, 1991.

[121] Patrick Roblin and Liou Wan-Rone. Scattering asisted tunneling in resonant tunneling diodes. *preprint, The Ohio State University*.

[122] E. V. Anda and F. Flores. The role of inelastic scattering in resonant tunneling heterostructures. *J. Phys.: Condens. Matter*, 3:9087–9101, 1991.

[123] P. J. Turley and S. W. Teitsworth. Electronic wavefunctions and electron-confined-phonon matrix elements in $GaAs/Al_xGa_{(1-x)}As$ double barrier resonant tunneling structures. *Phys. Rev. B*, 44(7):3199–3210, 1991.

[124] P. J. Turley and S. W. Teitsworth. Phonon-assited tunneling due to localized modes in double-barrier structures. *Phys. Rev. B*, 44(15):8181–8184, 1991.

[125] P. J. Turley and S. W. Teitsworth. Theory of localized phonon modes and their effects on electron tunneling in double barrier structures. *preprint, submitted to J. Appl. Phys.*, 1992.

[126] P. J. Turley, C. R. Wallis, and S. W. Teitsworth. Effects of localized phonon modes on electronic transport in GaAs/AlAs double barrier structures. *Proceedings of the International Workshop on Computational Electronics, Urbana-Champaign*, pages 297–300, 1992.

[127] T. Inoshita and H. Sakaki. Electron relaxation in a quantum dot: Significance of multiphonon preocesses. *Phys. Rev. B*, 46(11):7260–3, 1992.

[128] Garnett W. Bryant. Resonant tunneling in zero-dimensional nanostructures. *Phys. Rev. B*, 39(5):3145–52, 1989.

[129] Garnett W. Bryant. Understanding quantum-box resonant-tunneling spectroscopy: Fine structure at fermi-level crossings. *Phys. Rev. B*, 44(8):3782–6, 1991.

[130] Garnett W. Bryant. Nonadiabatic transport through quantum dots. *Phys. Rev. B*, 44(23):12837–47, 1991.

[131] H. C. Liu and G. C. Aers. Resonant tunneling through one-, two-, and three-dimensionally confined quantum wells. *J. Appl. Phys.*, 65(12):4908–14, 1989.

[132] Seigo Tarucha and Yoshiro Hirayama. Magnetotunneling in a coupled two-dimensional-one-dimensional electron system. *Phys. Rev. B*, 43(11):9373–6, 1991.

[133] Seigo Tarucha, Yoshiro Hirayama, and Yasuhiro Tokura. Subband mixing effect in double-barrier diodes with a restricted lateral dimension. *Appl. Phys. Lett.*, 58(15):1623–5, 1991.

[134] Garnett W. Bryant. Electronic structure of ultrasmall quantum-well boxes. *Phys. Rev. Lett.*, 59(10):1140–3, 1987.

[135] P. A. Maksym and Tapash Chakraborty. Quantum dots in a magnetic field: Role of electron-electron interactions. *Phys. Rev. Lett.*, 65(1):108–11, 1990.

[136] N. F. Johnson and M. C. Payne. Exactly solvable model of interacting particles in a quantum dot. *Phys. Rev. Lett.*, 67(9):1157–60, 1991.

[137] N. F. Johnson and M. C. Payne. Many-body effects in resonant tunneling through quantum dots. *Phys. Rev. B*, 45(7):3819–21, 1992.

[138] B. L. Johnson and G. Kirczenow. Electrons in quantum dots: A comparison of interaction energies. *Phys. Rev. B*, 47(16):10563–6, 1993.

[139] Wolfgang Häusler and Bernhard Kramer. Interacting electrons in a one-dimensional quantum dot. *Phys. Rev. B*, 47(24):16353–7, 1993.

[140] Arvind Kumar, Steven E. Laux, and Frank Stern. Electron states in a GaAs quantum dot in a magnetic field. *Phys. Rev. B*, 42(8):5166–75, 1990.

[141] Garnett W. Bryant. Resonant tunneling through coupled, double-quantum-box nanostructures. *Phys. Rev. B*, 44(7):3064–9, 1991.

[142] L. I. Glazman and V. Chandrasekhar. Coulomb blockade oscillations in a double-dot system. *Europhys. Lett.*, 19(7):623–8, 1992.

[143] A. Alan Middleton and Ned S. Wingreen. Collective transport in arrays of quantum dots. *preprint*, 1993.

[144] P. Delsing. *One-Dimensional Arrays of Small Tunnel Junctions*, chapter 7, pages 249–273. Plenum, New York, 1992.

[145] Leo P. Kouwenhoven, F. W. J. Hekking, B. J. van Wees, C. J. M. Harmans, C.E.Timmering, and C.T. Foxon. Transport through a finite one-dimensional crystal. *Phys. Rev. Lett.*, 65(3):361–4, 1990.

[146] M. Tewordt, H. Asahi, V.J. Law, R. T. Syme, M. J. Kelly, D. A. Ritchie, A. Chruchill, J. E. F. Frost, R. H. Hughes, and G. A. C. Jones. Resonant tunneling in coupled quantum dots. *Appl. Phys. Lett.*, 60(5):595–7, 1992.

[147] R. J. Haug, J.M. Hong, and K.Y. Lee. Electron transport through one quantum dot and through a string of quantum dots. *Surface Science*, 263:415–8, 1992.

[148] C.Y. Fong, J.S.Nelson, L.A. Hemstreet, R.F. Gallup, L.L. Chang, and L. Esaki. Resonant tunneling in coupled quantum dots. *Phys. Rev. B*, 46(15):9538–43, 1992.

[149] M. W. Dellow, P. H. Beton, M. Henini, P. C. Main, L. Eaves, S. P. Beaumont, and C. D. W. Wilkinson. Gated resonant tunneling devices. *Electr. Lett.*, 27(2):134–6, 1991.

[150] P. Guéret, N. Blanc, R. Germann, and H. Rothuizen. Confinement and single-electron tunneling in schottky-gated, laterally squeezed double-barrier quantum-well heterostructures. *Phys. Rev. Lett.*, 68(12):1896–99, 1992.

[151] E. Dagotto, A. Moreo, F. Ortolani, J. Riera, and D. J. Scalapino. Density of states of doped hubburd clusters. *Phys. Rev. Lett.*, 67(14):1918–21, 1991.

[152] Efthimoios Kaxiras and Efstratios Manousakis. Ground state of the strong-coupling hubbard hamiltonian: A numerical diagonalization study. *Phys. Rev. B*, 37(1):656–9, 1988.

[153] N. Mori and T. Ando. Electron-optical phonon interaction in single and double heterostructures. *Phys. Rev. B*, 40(9):6175–6188, 1989.

[154] M. Babiker. Coupling of polar optical phonons to electrons in superlattices and isolated quantum wells. *Semicond. Sci. Technol.*, 7:B52–9, 1992.

[155] H. Rucker, E. Molinari, and P. Lugli. Microscopic calculation of the electron-phonon interaction in quantum wells. *Phys. Rev. B*, 45(12):6747–56, 1992.

[156] Xi-Xia Liang and Xu Wang. Electron-phonon interaction in a quantum well. *Phys. Rev. B*, 43(6):5155–8, 1991.

[157] P. J. Turley, May 1992. Private Communication.

[158] J. A. Levenson, G. Dolique, J.L. Oudar, and I. Abram. Intersubband carrier relaxation in highly excited $GaAs/Ga_{(1-x)}Al_xAs$ multiple quantum wells. *Phys. Rev. B*, 41(6):3688–3694, 1990.

[159] T. Weil and B. Vinter. Equivalence between resonant tunneling and sequential tunneling in double-barrier diodes. *Appl. Phys. Lett.*, 50(18):1281–1283, 1987.

[160] L. Eaves, M. L. Leadbeater, D. G. Hayes, E. S. Alves, F. W. Sheard, G. A. Toombs, P. E. Simmonds, M. S. Skolnick, M. Henini, and O. H. Hughes. Electrical and spectroscopic studies of space-charge buildup, energy relaxation and magnetically enhanced bistability in resonant tunneling structures. *Solid-State Electronics*, 32(12):1101–1108, 1989.

[161] M. S. Skolnick, D. G. Hayes, C. R. H. White, P. E. Simmonds, L. Eaves, A. W. Higgs, G. W. Smith, C. R. Whitehouse, M. Henini, and O. H. Hughes. Optical investigations of vertical transport in double barrier resonant tunneling structures. In Wiley P. Kirk and Mark A. Reed, editors, *Nanostructures and Mesoscopic Systems*, pages 445–54, Boston, 1992. Academic Press.

[162] C. R. H. White, M. S. Skolnick, L. Eaves, M. L. Leadbeater, M. Henini, and O. H. Hughes. Optical investigation of a very asymmetric double barrier resonant tunneling structure. *Phys. Rev. B*, 45(12):6721–6730, 1992.

[163] M. S. Skolnick, P. E. Simmonds, D. G. Hayes, C. R. H. White, L. Eaves, A. W. Higgs, M. Henini, O. H. Hughes, G. W. Smith, and C. R. Whitehouse. Electron transport in double barrier resonant tunneling structures studied by optical spectroscopy. *Semicond. Sci. Technol.*, 7:B401–B408, 1992.

[164] Gerhard Klimeck. Electron-phonon interactions and electron charging effects in single and multi-quantum wells. Technical report, 1992. unpublished.

[165] T. Nakagawa, T. Fujita, Y. Matsumoto, T. Kojima, and K. Ohta. Thermally stimulated resonant current in AlGaAs/GaAs triple barrier diodes. *Appl. Phys. Lett.*, 51(6):445–447, 1987.

[166] D. X. Xu, G. D. Shen, M. Willander, and G. V. Hansson. The properties of resonant transmission in triple-barrier / double-quantum-well heterostructures. *J. Appl. Phys.*, 71(8):3859–64, 1992.

[167] D. A. Collins, D. H. Chow, D. Z.-Y. Ting, E. T. Yu, J. R. Söderström, T. C. McGill, and T. J. Watson Sr. Large peak-to-valley current ratios in triple barrier heterostructures. *Solid-State Electronics*, 32(12):1095–1099, 1989.

[168] T. Nakagawa, T. Fujita, Y. Matsumoto, T. Kojima, and K. Ohta. Sharp resonance characteristics in triple barrier diodes. *Jap. J. of Appl. Phys.*, 26(6):L980–L982, 1987.

[169] Rolf Landauer. Electrical resistance of disordered one-dimensional lattices. *Phil. Mag.*, 21:863–867, 1970.

[170] T. Nakagawa, H. Imamoto, T. Kojima, and K. Ohta. Observation of resonant tunneling in AlGaAs/GaAs triple barrier diodes. *Appl. Phys. Lett.*, 49(2):73–75, 1986.

[171] T. Nakagawa, T. Fujita, Y. Matsumoto, T. Kojima, and K. Ohta. Resonant tunneling of holes in AlAs/GaAs triple barrier diodes. *Appl. Phys. Lett.*, 50(15):974–976, 1987.

[172] T. Nakagawa, T Kojima, and K. Ohta. Tunneling of x-point electrons in triple barrier diodes. *Journal of Crystal Growth*, 95:357–359, 1989.

[173] P. Cheng, B. G. Park, S. Kim, and Jr. J. S. Harris. The x-valley transport in GaAs/AlAs triple barrier structures. *J. Appl. Phys.*, 65(12):5199–5201, 1989.

[174] H. Asahi, M. Tewordt, R. T. Syme, M. J. Kelly, V. J. Law, D. R. Mace, J. E. F. Frost, D. A. Ritchie, G. A. C. Jones, and M. Pepper. Tunneling between totally quantized levels in GaAs/AlGaAs asymmetric triple barrier heterostructures in high magnetic fields. *Appl. Phys. Lett.*, 59(7):803–805, 1991.

[175] H. Asahi, M. Tewordt, R. T. Syme, M. J. Kelly, V. J. Law, J. E. F. Frost, D. A. Ritchie, G. A. C. Jones, and M. Pepper. Fine structure in the i-v characteristics of GaAs/AlGaAs submicron diameter triple barrier diodes. *Surface Science*, 267:388–391, 1992.

[176] M. Tewordt, H. Asahi, V. J. Law, R. T. Syme, M. J. Kelly, D. A. Ritchie, A. Churchill, J. E. F. Frost, and R. H. Hughes. Resonant tunneling in coupled quantum dots. *Appl. Phys. Lett.*, 60(5):595–597, 1992.

[177] D. X. Xu, G. D. Shen, M. Willander, F. Schaffler, and J. F. Luy. Experimental studies on the ndr of $si_{(1-x)}ge_x$/si triple barrier resonant tunneling diodes. *Solid State Electronics*, 34(5):611–614, 1992.

[178] A. G. MacDonald, L. V. Iogansen, D. J. Day, M. Sweeny, and J. Xu. Well width dependence of tunneling current in double-quantum-well resonant interband tunnel diodes. *IEEE Electron Device Letters*, 13(3):155–157, 1992.

[179] L. Yang, J. F. Chen, and A. Y. Cho. New GaSb / AlSb / GaSb / AlSb / InAs / AlSb / InAs triple barrier interband tunneling diode. *Electronics Letters*, 26(16):1277–1279, 1990.

[180] H. Kawai, J. Kaneko, and N. Watanabe. Doublet state of resonantly coupled Al-GaAs.GaAs quantum wells grown by metalorganic chemical vapor deposition. *J. Apll. Phys.*, 58(3):1263–1269, 1985.

[181] Tomofumi Furuta, Kazuhiko Hirakawa, Junji Yoshino, and Hiroyuki Sakaki. Splitting of photoluminescence spectra and negative differential resistance caused by the electric field induced resonant coupling of quantized levels in GaAs-AlGaAs multi-quantum well structures. *Japn. J. of Appl. Phys.*, 26(2):L151–L154, 1986.

[182] Karl Leo, Jagdeep Shah, E. O. Göbel, J. P. Gordon, and Stefan Schmitt-Rink. Coherent and incoherent tunneling in asymmetric double quantum wells. *Semicond. Sci. Technol.*, 7:B394–B400, 1992.

[183] D. Y. Oberli, J. Shah, T. C. Damen, C. W. Tu, T. Y. Chang, D. A. B. Miller, J. E. Henry, R. F. Kopf, N. Sauer, and A. E. DiGiovanni. Direct measurement of resonant and nonresoanant tunneling times in asymmetric coupled quantum wells. *Phys. Rev. B*, 40(5):3028–3031, 1989.

[184] H. Q. Le, J. J. Zayhowsi, and W. D. Goodhue. Stark effect in $Al_xGa_{(1-x)}As/GaAs$ coupled quantum wells. *Appl. Phys. Lett.*, 50(21):1518–1520, 1987.

[185] H. W. Liu, R. Ferreira, G. Bastard, C. Delalande, J. F. Palmier, and B. Etienne. Optical evidences of assisted tunneling in a biased double quantum well structure. *Appl. Phys. Lett.*, 54(21):2082–2084, 1989.

[186] D. Y. Oberli, Jagdeep Shah, T. C. Damen, J. M. Kuo, J. E. Henry, Jennifer Lary, and Stephen M. Goodnick. Optical phonon-assisted tunneling in double quantum well structures. *Appl. Phys. Lett.*, 56(13):1239–1241, 1990.

[187] D. F. nelson, R. C. Miller, D. A. Kleinman, and A. C. Gossard. Tunneling-assited photon emission from quantum wells. *Phys. Rev. B*, 34(12):8671–8675, 1986.

[188] N. Sawaki, R. A. Hopfel, E. Gornik, and H. Kano. Time-resolved measuremnt of tunneling and energy relaxation of hot electrons in GaAs/AlGa.

[189] Garnett W. Bryant. Interdot tunneling and coulomb correlation. *Physica B*, 189:34–42, 1993.

[190] J. Hubbard. Electron correlations in narrow energy bands. *Proc. Roy. Soc.*, 276:238–57, 1963.

[191] J. Hubbard. Electron correlations in narrow energy bands iii. an improved solution. *Proc. Roy. Soc.*, 281:401–19, 1964.

[192] Gerald D. Mahan. *Many-Particle Physics*. Plenum, New York, 2 edition, 1990.

Appendix A

Keldysh Formalism

A.1   Introduction

The following sections are meant to provide a brief overview of the Green's function approach taken in our research group. We will show, how the dephasing of electrons and holes in the conduction band can be derived from a microscopic scattering model. The particle propagation at one energy will be described by Greens functions that are the solutions to an effective mass single-electron Hamiltonian which includes the electron-phonon interaction by a self-energy. The inclusion of many-body effects into the single-particle picture is based on a perturbation treatment, which means that this perturbation has to be weak. The perturbation treatment breaks down if particle correlations become strong, as for example in the case of single electron-electron correlations. For a more detailed discussion we refer the reader to References [64, 91, 92].

A.2   Green's Functions

The formalism that is the basis of our approach has been developed by Keldysh[57] and Kadanoff and Baym[58] less than 30 years ago. The two-time electron correlation function, $G^<$, is the central quantity in this formulation

$$-i\hbar G^<(\vec{r}, \vec{r}; t_1, t_2) = \langle \Psi^\dagger(\vec{r}, t_2)\, \Psi(\vec{r}, t_1) \rangle \ , \tag{A.1}$$

where $\Psi(\vec{r}_1, t_1)$ is the electron field operator. It is common to transform to relative time coordinates, $T = (t_1 + t_2)/2$ and $t = (t_1 - t_2)$, and Fourier transform with respect to the new time difference coordinate, t, to obtain $G^<(\vec{r}_1, \vec{r}_2; E, T)$. $G^<(\vec{r}_1, \vec{r}_2; E, T)$ can be related to the density matrix, $\rho(\vec{r}_1, \vec{r}_2, T)$, by setting $t_1 = t_2$ in $G^<$ which is equivalent to

$$\rho(\vec{r}_1, \vec{r}_2, T) = \int \frac{dE}{2\pi}\, G^<(\vec{r}_1, \vec{r}_2; E, T) \ . \tag{A.2}$$

In steady-state it is assumed that there is no variation with the variable $T = (t_1 + t_2)/2$ and we will neglect this coordinate from now on. Similar to approaches based on density

---

matrices, the correlation function, $G^<$, has the role of a distribution function from which macroscopic quantities may be calculated. From $G^<$ we can easily obtain the electron density and current density per unit energy by the following relations

$$n(\vec{r}, E) = -\frac{i}{2\pi} \ G^<(\vec{r}, \vec{r}; E) \ , \tag{A.3a}$$

$$\vec{J}(\vec{r}, E) = -\frac{e\hbar}{4\pi m} \ (\nabla - \nabla') \ G^<(\vec{r}, \vec{r}\,'; E)\Big|_{\vec{r}=\vec{r}\,'} \ + \ \frac{ie^2}{2\pi m} \ \vec{A}(\vec{r}) \ G^<(\vec{r}, \vec{r}; E) \ . \tag{A.3b}$$

The total electron and current density are obtained by integration over the energy coordinate of their respective densities

$$n(\vec{r}) = \int dE \ n(\vec{r}, E) \ , \tag{A.4a}$$

$$\vec{J}(\vec{r}) = \int dE \ \vec{J}(\vec{r}, E) \ . \tag{A.4b}$$

The correlation function, $G^<$, is based on a microscopic model that involves several Green's functions[61,63,64] as solutions to several microscopic Hamiltonians. To obtain $G^<$ we need to solve

$$G^{<(>)}(\vec{r}, \vec{r}\,'; E) = \int d\vec{r}_1 d\vec{r}_2 \ G^R(\vec{r}, \vec{r}_1; E) \ \Sigma^{<(>)}(\vec{r}_1, \vec{r}_2; E) \ G^A(\vec{r}_2, \vec{r}\,'; E) \ , \tag{A.5}$$

where the retarded and advanced Green's functions, G^R and G^A, are related by

$$G^A(\vec{r}, \vec{r}\,'; E) = \left(G^R(\vec{r}\,', \vec{r}; E) \right)^* \ . \tag{A.6}$$

The retarded Green's function, G^R, is based on a single-electron Hamiltonian involving the appropriate self-energy to incorporate the effects of the other Hamiltonians

$$(E - H_0(\vec{r})) \ G^R(\vec{r}, \vec{r}\,'; E) - \int d\vec{r}_1 \Sigma^R(\vec{r}, \vec{r}_1; E) \ G^R(\vec{r}_1, \vec{r}\,'; E) = \delta \left(\vec{r} - \vec{r}\,' \right) \ . \tag{A.7}$$

G^R is the impulse response of a single-electron Hamiltonian that incorporates the interaction with other particles via the self-energy, Σ^R. The retarded Green's function, G^R, is the causal response, the advanced Green's function, G^A, is the anti-causal impulse response. $G^{<(>)}$ has the role of an ensemble or distribution function that is based on a convolution with an appropriate ensemble self-energy.

After this brief interpretation of the electron Green's functions, we now need to provide some more insight in the meaning of the self-energies, Σ^R and $\Sigma^{<(>)}$. Σ^R can be written as the sum of a Hermitian and anti-Hermitian contribution

$$\Sigma^R(\vec{r}, \vec{r}\,'; E) = \sigma(\vec{r}, \vec{r}\,', E) - \frac{i}{2} \ \Gamma(\vec{r}, \vec{r}\,'; E) \ . \tag{A.8}$$

The anti-Hermitian contribution is due to self-energies, $\Sigma^{<(>)}$, that are nonzero. This anti-Hermitian contribution causes the system not to conserve particles for every energy anymore

(dissipation). The anti-Hermitian part of the retarded self-energy can be written terms of $\Sigma^{<(>)}$ as

$$\Gamma\left(\vec{r}, \vec{r}\,'; E\right) = -i\left(\Sigma^<\left(\vec{r}, \vec{r}\,'; E\right) - \Sigma^>\left(\vec{r}, \vec{r}\,'; E\right)\right) \ . \tag{A.9}$$

The Hermitian contribution contains the Hilbert transform of the anti-Hermitian part and contributions due to self-energies with $\Sigma^{<(>)} = 0$ (which do not have an anti-Hermitian contribution).

$$\sigma\left(\vec{r}, \vec{r}\,'; E\right) = \frac{1}{\pi}\ P\int \frac{dE'}{2\pi}\ \frac{\Gamma(\vec{r}, \vec{r}\,'; E)}{E - E'}\ +\ \Sigma^R_{HF} + \Sigma^R_{other\,\Sigma^{<(>)}=0} \ . \tag{A.10}$$

In all current work we have neglected this real part of the retarded self-energy, σ, and have only worked with the imaginary part, Γ, which allows for transitions between energies. $\Sigma^{<(>)}$ is determined by the type of interaction considered. The specification of $\Sigma^{<(>)}$ closes the set of equations (A.5) – (A.10) and the closed set needs to be solved self-consistently.

A.3   Microscopic Model

Datta[64] has introduced three Hamiltonians into his model. The single-electron effective mass Hamiltonian

$$H_0(\vec{r}) = \frac{\left(\vec{p} - e\vec{A}(\vec{r})\right)^2}{2m}\ +\ V(\vec{r}) \ , \tag{A.11}$$

describes electrons within one band, where the potential, $V(\vec{r})$, includes potential drops across the device and band discontinuities. Dephasing processes are due to a reservoir of independent oscillators assumed to be in thermal equilibrium

$$H^B = \sum_m\ \hbar\omega_m\ \left(a_m^\dagger a_m + \frac{1}{2}\right) \ , \tag{A.12}$$

which interacts with the the electrons through a δ-potential in space

$$H' = \sum_m\ U\ \delta(\vec{r} - \vec{r}_m)\ \left(a_m^\dagger + a_m\right) \ . \tag{A.13}$$

The sum over phonon modes, $\sum_m$, can be turned into an integral with the assumption of a continuum of modes characterized by a density of oscillator modes

$$\sum_m \longrightarrow \int d\vec{r}\int d\left(\hbar\omega\right)\ J_0(\vec{r}; \hbar\omega) \ . \tag{A.14}$$

In the current implementation of QUEST[56] we implemented two different spectra of oscillator modes, J_0

$$\bullet Einstein\,phonons:\quad J_0(\hbar\omega) \propto \delta(\omega \pm \omega_0)\ ;\ \hbar\omega_0 = 36meV \tag{A.15}$$
$$\bullet Debye\,phonons:\quad J_0(\hbar\omega) \propto \omega^2\Theta(\omega_D - |\omega|)\ ;\ \hbar\omega_D = 20meV.$$

Expressions for $\Sigma^{<(>)}$ have been derived using the Hamiltonians in Eqs. (A.12) and (A.13) with the following assumptions:

- The phonon reservoir is in local equilibrium and the oscillator coordinates can be traced out.
- Only one phonon scattering processes are allowed, this corresponds to the first Born-approximation, but it is carried out self-consistently to all orders

$$\Sigma^<(\vec{r}_1, \vec{r}_2; E) = +i\, \frac{\hbar}{\tau_p(\vec{r}_1; E)}\, \delta(\vec{r}_1 - \vec{r}_2)\ , \tag{A.16a}$$

$$\Sigma^>(\vec{r}_1, \vec{r}_2; E) = -i\, \frac{\hbar}{\tau_n(\vec{r}_1; E)}\, \delta(\vec{r}_1 - \vec{r}_2)\ , \tag{A.16b}$$

and

$$\Sigma^R(\vec{r}_1, \vec{r}_2; E) = \left(\sigma(\vec{r}_1, E)\ -\ i\, \frac{\hbar}{2\tau_\phi(\vec{r}_1; E)} \right)\, \delta(\vec{r}_1 - \vec{r}_2)\ , \tag{A.16c}$$

where $\frac{1}{\tau_n(\vec{r}; E)}$ is the electron out-scattering rate, $\frac{1}{\tau_p(\vec{r}; E)}$ is the hole out-scattering rate and $\frac{1}{\tau_\phi(\vec{r}; E)} = \frac{1}{\tau_n(\vec{r}; E)} + \frac{1}{\tau_p(\vec{r}; E)}$ is the total dephasing rate. So far we have just stated the locality in space of $\Sigma^{<(>)}$ which is due to the local interaction Hamiltonian H'. We still need to express the newly introduced scattering times in terms of oscillator densities. To bring the equations that we actually solve into a final form, we introduce the following quantities

$$n(\vec{r}; E) \quad = \quad -\frac{i}{2\pi}\, G^<(\vec{r}, \vec{r}; E)\ , \tag{A.17a}$$

$$p(\vec{r}; E) \quad = \quad +\frac{i}{2\pi}\, G^>(\vec{r}, \vec{r}; E)\ , \tag{A.17b}$$

$$N_0(\vec{r}; E) \quad = \quad n(\vec{r}; E) + p(\vec{r}; E) = -\frac{1}{\pi}\, Im G^R(\vec{r}, \vec{r}; E)\ , \tag{A.17c}$$

which are the electron density, hole density and local density of states all per unit area, respectively. Furthermore we define the non-equilibrium occupation factor, $f(\vec{r}; E)$, as

$$f(\vec{r}; E) = \frac{n(\vec{r}; E)}{N_0(\vec{r}; E)}\ , \tag{A.18}$$

which reduces to the Fermi-Dirac factor in equilibrium.

The final equations for the one electron Green's function, G^R, coupled to a bath of independent oscillators may now be written down as

$$\left(E - H_0(\vec{r}) - \sigma(\vec{r}; E) + i\frac{\hbar}{2\tau_\phi(\vec{r}; E)} \right) G^R(\vec{r}, \vec{r}\,'; E) = \delta(\vec{r} - \vec{r}\,')\ , \tag{A.19a}$$

$$N_0(\vec{r}; E) \quad = \quad -\frac{1}{\pi}\, Im\left\{ G^R(\vec{r}, \vec{r}; E) \right\}\ , \tag{A.19b}$$

$$f(\vec{r}; E) = \frac{1}{N_0(\vec{r}; E)}\, \frac{\hbar}{2\pi}\, \int d\vec{r}\,'\, \frac{\left| G^R(\vec{r}, \vec{r}\,'; E) \right|^2}{\tau_p(\vec{r}; E)}\ , \tag{A.19c}$$

$$\frac{1}{\tau_p(\vec{r}; E)} = \frac{2\pi}{\hbar} \int d(\hbar\omega) \ F(\vec{r}; \hbar\omega) \ N_0(\vec{r}; E - \hbar\omega) \ f(\vec{r}; E - \hbar\omega) \ , \quad \text{(A.19d)}$$

$$\frac{1}{\tau_n(\vec{r}; E)} = \frac{2\pi}{\hbar} \int d(\hbar\omega) \ F(\vec{r}; \hbar\omega) \ N_0(\vec{r}; E + \hbar\omega) \ f(\vec{r}; E + \hbar\omega) \ , \quad \text{(A.19e)}$$

$$\frac{1}{\tau_\phi(\vec{r}; E)} = \frac{1}{\tau_n(\vec{r}; E)} + \frac{1}{\tau_p(\vec{r}; E)} \ , \quad \text{(A.19f)}$$

where $F(\vec{r}; \hbar\omega)$ is a given function depending on the oscillator strength and spectrum $U^2 \ J_0(\vec{r}; \hbar\omega)$ and the average number $N(\omega)$ of phonons available with energy $\hbar\omega$ given by Bose-Einstein statistics

$$N(\omega) = \frac{1}{e^{\frac{\hbar\omega}{k_B T}} - 1} \ , \quad \text{(A.20)}$$

$$F(\vec{r}; \hbar\omega) = U^2 \ J_0(\vec{r}; \hbar\omega) \times \left\{ \begin{array}{ll} N(\omega) & ; \omega > 0 \\ N(|\omega|) + 1 & ; \omega < 0 \end{array} \right. . \quad \text{(A.21)}$$

Inserting Eq. (A.19d) into Eq. (A.19c) results in a homogeneous integral equation for the occupation factor

$$f(\vec{r}; E) = \frac{1}{N_0(\vec{r}; E)} \ \frac{\hbar}{2\pi} \int d\vec{r}\,' \int d(\hbar\omega) \ \left| G^R(\vec{r}, \vec{r}\,'; E) \right|^2 F(\vec{r}\,'; \hbar\omega)$$
$$\times N_0(\vec{r}\,'; E - \hbar\omega) \ f(\vec{r}\,'; E - \hbar\omega) \ , \quad \text{(A.22)}$$

which generally cannot be solved analytically. But this scheme lends itself nicely to an iterative solution procedure where initial guesses for the scattering rates, $1/\tau_p$ and $1/\tau_n$, and for the occupation, f, will get refined from iteration to iteration. Also note that that Eq. (A.19a) for the retarded Green's function is now of the form $OG^R = \delta$ and all energies are decoupled in the operator O. An equation of such structure is relatively easy to solve. An implementation on a tight-binding lattice couples only next neighbors, which results in a sparse matrix problem. A nonlocal potential in space would couple more than the next neighbors in the discretization grid and would result in a much more massive problem to be solved.

Since we have found a way to calculate the single-electron Green's function self-consistently with the self-energies, $\Sigma^{<(>)}$, we can now evaluate $G^{<(>)}(\vec{r}, \vec{r}\,'; E)$ from Eq. (A.5) and use this expression with Eq. (A.3b) to obtain a current density. This density needs to be integrated across the cross-section of the structure. In the contacts where the current is zero at infinity this surface integral can be converted into a volume integral and the resulting current per unit energy, per unit volume is

$$I(\vec{r}; E) = \frac{e\,\hbar}{2\pi} \int d\vec{r}\,' \ \frac{\left| G^R(\vec{r}, \vec{r}\,'; E) \right|^2}{\tau_\phi(\vec{r}; E) \ \tau_\phi(\vec{r}\,'; E)} \left(f(\vec{r}; E) - \frac{\tau_\phi(\vec{r}\,'; E)}{\tau_p(\vec{r}\,'; E)} \right) \ , \quad \text{(A.23)}$$

which can be be cast into the form of Eq. (2.4) by using Eq. (2.5) and defining the transmission coefficient as

$$T(\vec{r}, \vec{r}\,'; E) = \frac{\hbar^2 \left| G^R(\vec{r}, \vec{r}\,'; E) \right|^2}{\tau_\phi(\vec{r}; E) \ \tau_\phi(\vec{r}\,'; E)} \ . \tag{A.24}$$

$$I(\vec{r}; E) = \frac{e}{h} \int d\vec{r}\,' \ T(\vec{r}, \vec{r}\,'; E) \ \ (f(\vec{r}; E) - f_\tau(\vec{r}\,'; E)) \ , \ \ [c.f.2.4] \tag{A.25}$$

We have therefore obtained a transfer function $T(\vec{r}, \vec{r}\,'; E)$ in terms of a microscopic model.

The expression for the current was derived for any point $\vec{r}$ in the contact. Using Eq. (A.19c) one can show that $I(\vec{r}; E) = 0 \ \ \forall \{\vec{r}\} \in Device$. This corresponds to the current boundary condition given in Eq. (2.3). This boundary condition is being substituted by a condition on the Green's function in the contacts. The Green's functions in the contacts need to decay with a dephasing length such that the current density is zero at infinity and the surface integral over the contact can be closed and transformed into a volume integral. The solution to an open-ended one dimensional wire Green's function is known and we extend G^R from the numerical nodes analytically to infinity using the phase-breaking time obtained in the numerical nodes. Therefore, our model includes phase-breaking throughout the whole device *and* the contacts region.

The boundary condition on the occupancy, f, is an assumed Fermi-Dirac distribution function in the contacts with well defined chemical potentials as already discussed with Eq. (2.3).

In summary we can state that we have a formalism based on a microscopic Hamiltonian model for which we can solve for the non-equilibrium occupancy, $f(\vec{r}; E)$, in the device and and the current, $I(\vec{r}; E)$, in the contacts self-consistently with Eqs. (A.19) and (A.23).

A.4 Optical Phonons

We are now at the stage where we can consider a particular oscillator spectrum for a particular scattering mechanism. We will here consider an Einstein spectrum of optical phonons which we model using Eqs. (A.21) and (A.15) as

$$F(\vec{r}; \hbar\omega) = \tilde{U}^2 \times \begin{cases} \delta(\hbar\omega - \hbar\omega_0) \, N(\hbar\omega) & ; \hbar\omega > 0 \\ \delta(\hbar\omega + \hbar\omega_0) \, N(|\hbar\omega|) + 1 & ; \hbar\omega < 0 \end{cases} , \tag{A.26}$$

where we have simplified $\tilde{U}^2 = U^2 * J_0(\vec{r})$. Using U instead of $\tilde{U}$ from now on one can simplify Eq. (A.26) further to

$$F(\vec{r}; \hbar\omega) = U^2 \left\{ N\delta(\hbar\omega - \hbar\omega_0) + (N+1)\,\delta(\hbar\omega + \hbar\omega_0) \right\} , \tag{A.27}$$

with

$$N = \frac{1}{e^{\frac{\hbar\omega_0}{k_B T}} - 1} \ . \tag{A.28}$$

With this delta δ-function spectrum in Eq. (A.27) we can simplify Eqs. (A.19d) and (A.19e) by integrating out the energy dependence

$$\frac{\hbar}{\tau_n(\vec{r};E)} = 2\pi U^2 \ \{(N{+}1) \ N_0(\vec{r}, E{-}\hbar\omega_0) \ (1{-}f(\vec{r}, E{-}\hbar\omega_0))$$

$$+ \ N \ N_0(\vec{r}, E{+}\hbar\omega_0) \ (1{-}f(\vec{r}, E{+}\hbar\omega_0))\} \ , \qquad \text{(A.29a)}$$

$$\frac{\hbar}{\tau_p(\vec{r};E)} = 2\pi U^2 \ \{(N{+}1) \ N_0(\vec{r}, E{+}\hbar\omega_0) \ f(\vec{r}, E{+}\hbar\omega_0)$$

$$+ \ N \ N_0(\vec{r}, E{-}\hbar\omega_0) \ f(\vec{r}, E{-}\hbar\omega_0)\} \ . \qquad \text{(A.29b)}$$

The optical phonon energy in bulk GaAs is about 36meV. For $T = 77K$ and $T = 4K$ we have $k_B T = 6.6meV$ and $k_B T = 0.34meV$, respectively. Using Eq. (A.28) we can calculate $N \approx 4.4 \times 10^{-3}$ and $N \approx 4.6 \times 10^{-46}$, respectively. If we are in the regime where $k_B T \ll \hbar\omega_0$ we can assume $N \approx 0$ and Eqs. (A.29a) and (A.29b) simplify to

$$\frac{\hbar}{\tau_n(\vec{r};E)} = 2\pi U^2 \ N_0(\vec{r}, E{-}\hbar\omega_0) \ (1{-}f(\vec{r}, E{-}\hbar\omega_0)) \qquad \text{(A.30a)}$$

$$\frac{\hbar}{\tau_p(\vec{r};E)} = 2\pi U^2 \ N_0(\vec{r}, E{+}\hbar\omega_0) \ f(\vec{r}, E{+}\hbar\omega_0) \ . \qquad \text{(A.30b)}$$

Eqs. (A.29) and (A.30) define the scattering rates that we have been using for the problem of the phonon peak in Chapters 2, and 3 and in Appendix B.

Appendix B

Scattering Rates: A Simple Example

We have discussed in Chapter 2 Section 2.2.3 how the scattering rates, $\frac{1}{\tau_n}$ and $\frac{1}{\tau_p}$ connect different energy coordinates at one spatial coordinate. We will try to make this connection clearer using the phonon peak example. We assume here to have a Lorentzian shaped density of states (Fig. B.1) with some electrons injected one optical phonon energy above the resonance. We further assume that all the states right under the peak of the Lorentzian are about filled (99%).
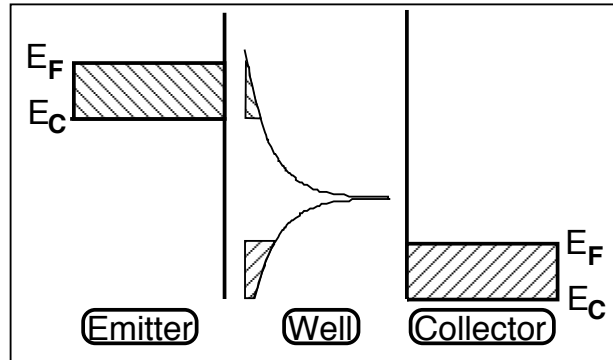
Figure B.1   Set-up for example calculation of scattering rates. Lorentzian shaped density of states in the well filled up in the bottom from the collector (right) side and filled with some electrons from the emitter (left) side.

Empty Resonant State
Let us first consider the case where the main resonance is empty (Fig. B.2a). Using only the information about the occupation, f, and the density of states, N_0, we can evaluate the scattering rates, $\frac{1}{\tau_n}$ and $\frac{1}{\tau_n}$ using Eq. 2.6 (see Fig B.2b). We can now see that the electron out-scattering, $\frac{1}{\tau_n}$, has a peaked feature one phonon energy above the resonance (at the incident energy, $E = +\hbar\omega_0$) and how the hole out-scattering rate, $\frac{1}{\tau_p}$, has a peaked

feature one phonon energy below the resonance. Note that the electron out-scattering rate, $\frac{1}{\tau_n}$, is the dominant scattering contribution by the relation of the total phase-breaking rate, $\frac{1}{\tau_\Phi} = \frac{1}{\tau_n} + \frac{1}{\tau_p}$, at the injection energy, $E = +\hbar\omega_0$. This means that at the incident energy electrons only leave (to lower energies). At the resonance energy, $E = 0$ the opposite scattering rate, the hole-out-scattering rate, $\frac{1}{\tau_p}$, is the dominant contribution and holes leave this energy (electrons are incident at this energy). This means that electrons are transported downward in energy from the incident energy to the resonance energy.

The first intuitive question that appeared to the author at this point was: "Why are the electron out-scattering rate at the incident energy and the electron in-scattering at the resonance different from each other?" The answer to this is that not the rates have to be equal, but the electron in- and out-scattering fluxes. Figure B.2c depicts the electron out-scattering flux[**], $\frac{n}{\tau_n}$, and the hole out-scattering flux, $\frac{p}{\tau_p}$. It can be seen now, that the hole-out-scattering flux is identical to the electron-out-scattering flux shifted downward in energy by one optical phonon energy. That means that all the injected electrons really arrive exactly one optical phonon energy below at the resonance.

Filled Resonant State:
Now that we have a more vivid picture of vertical flow, let us consider the effect of the filling of the resonance. Fig. B.2d is identical to Fig. B.2a except for the 99% filling of the resonance. The newly calculated electron out-scattering rate, $\frac{1}{\tau_n}$, at the injection energy in Fig. B.2e is clearly strongly reduced (see the comparing arrow between Fig. B.2b and B.2e. Since the number of injected electrons did not change (the occupation, f, was unchanged at the injection energy $E = +\hbar\omega_0$), the total downward electron flux has to be reduced due to the reduced scattering rate. This can be seen in Fig. B.2f as compared to Fig. B.2c.

With this lengthy example we have shown here:

- how the electron and hole out-scattering rates depend on energy,
- how the electron and hole out-scattering rates take care of the "vertical" energy flow of electron upon interaction with optical phonons,
- how the total particle flux between the different energies is conserved,
- how the Pauli-Exclusion-Principle is built into our scattering rate calculation.

Approximations for the Effective Occupation, f_τ
The scattering related quantity that appears explicitly in our transport equation (2.4) is the effective occupation, f_τ. It is defined as $f_\tau = \frac{\frac{1}{\tau_p}}{\frac{1}{\tau_n} + \frac{1}{\tau_p}}$ (c.f. Eq. (2.5)) and provides a relative measure of the electron in-scattering rate with respect to the total electron scattering rate. We have plotted the effective occupation, f_τ, in Fig. B.3 for the two different cases of filling discussed in Fig. B.2. We can see that effective occupation, f_τ, is negligible compared to the occupation, f, at the incident energy which means that there is no back-flow from the well into the emitter at the incident energy. At the resonance we see that the effective occupation, f_τ, is approximately 1 which implies that there is a large electron in-scattering

---

[**]See Eqs. A.17c and A.18 for the relations between the density of states, N_0, the occupation, f, the electron density, n, and the hole density, p.
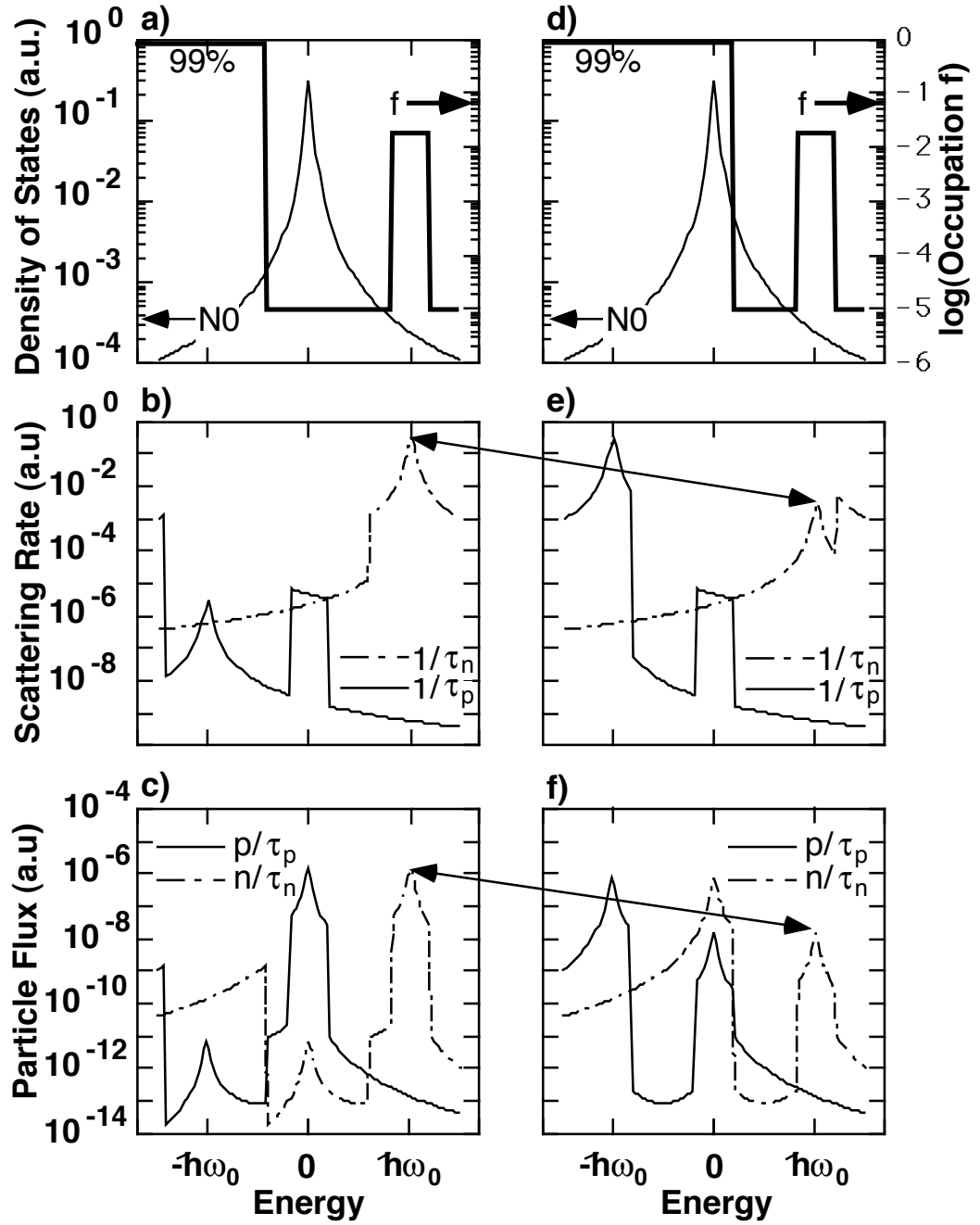
Figure B.2 Example for the energy dependence of the scattering rates, $\frac{1}{\tau_n}$ and $\frac{1}{\tau_p}$. a) Lorentzian Density of States, N_0, centered at zero energy, $E = 0$ and occupation, f, empty resonance. b) Scattering rates, $\frac{1}{\tau_n}$ and $\frac{1}{\tau_p}$, as calculated from Eqs. (2.6). c) Scattering fluxes, $\frac{n}{\tau_n}$ and $\frac{p}{\tau_p}$. d) Same as a) but full resonance (99%). e) Same as b), but based on d). f) Same as c), but based on d).

at this energy and that "back-scattering" from the device region (the resonance) to other probes (the collector) can be strong. Reference [76] assumes explicitly for the effective occupation, $f_\tau(E_i = +\hbar\omega_0) = 0$ and $f_\tau(E_r = 0) = 1$ for a significant simplification of analytic calculations explicitly neglecting back-flow into the emitter from the resonance.
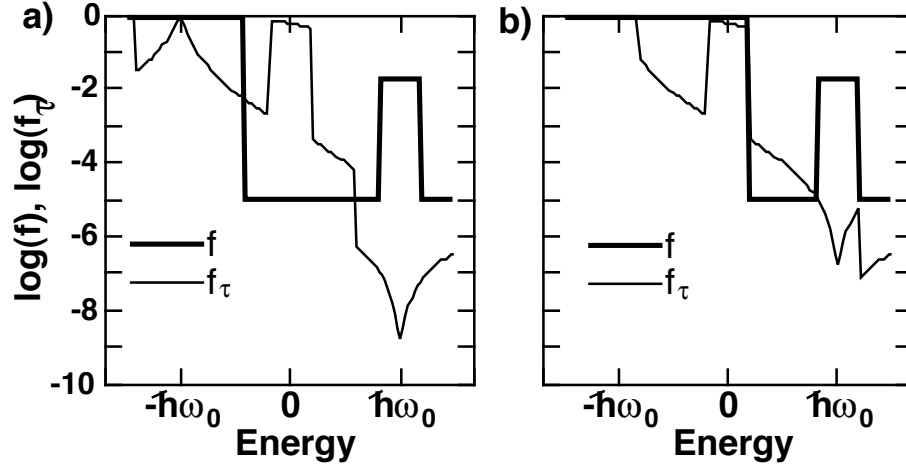
Figure B.3   Occupation, f, and effective occupation, f_τ, based on the example in Fig. B.2. a) and b) correspond to Fig. B.2a and B.2d, respectively.

Appendix C

Rate Equations for high Bias Transport in Coulomb Blockade Regime

C.1   Introduction

In this appendix we will first lay out the general rate equations used in the numerical simulations and discuss the origin and the limitation of the constant charging model. We then specialize the rate-equations for the 2 state case in which we derive analytical current expressions for transport through double barrier structures.

C.2   General Rate-Equations for the N-Particle Case

In Section 5.2, Figure 5.2 we have laid out the general idea of the configuration space and the coupling between the configurations. This approach has been put forward by Beenakker[70] for the treatment of Coulomb blockade problems. In Section 5.4.1 we discussed the single-electron spectrum that we are considering in this work and argued in Section 5.4.2 how the multiple degeneracy of the quantum states should be exploited to reduce the number of possible state configurations whose occupations need to be solved for. Beenakker's model is laid out for non-degenerate states and has to be extended to take care of multiple degeneracy. Furthermore we extend his model to include a finite intra-dot relaxation time.

We denote the eigen-energies of the quantum states as E_p and their corresponding degeneracies with d_p, where $p = 1, 2, \ldots$. The single-electron charging energy is assumed[69] to be

$$U(N) = N \left(N - 1 \right) \frac{e^2}{2C} \ , \tag{C.1}$$

where N is the total number of electrons in the quantum dot and C is the electro-static charge coupling of the quantum dot to the reservoirs. Beenakker assumed a charging energy of the form $U(N) = N^2 \frac{e^2}{2C}$ which is a good approximation for the case large N.

We assume here that the first electron does *not* have a charging energy against the reservoirs.[69] The coupling to the leads is assumed to be weak enough such that the single-electron states in the quantum dot are considered to be sharp compared to the temperature $(k_B T \gg \hbar\Gamma = \hbar\,(\Gamma_R + \Gamma_L + 1/\tau))$ and to the single-electron energy spectrum and charging energies $(\Delta E, U \gg \hbar\Gamma)$.

Energy-Balance: The transport trough the quantum dot is assumed to be based on sequential single-electron hopping into and out of the quantum dot via the connected reservoirs. The energy of each electron before and after the transition must be conserved. The conserved energy includes the single-particle energy, the charging energy against the other electrons in the quantum dot and the electro-static potential energy due to the applied bias across the structure (Fig. 5.1). Beenakker has denoted four energy balance equations for four electron tunneling processes:
1) into the quantum dot, being *initially* on the *Left* (index : i, L),
2) out of the quantum dot, being *finally* on the *Left* (index : f, L),
3) into the quantum dot, being *initially* on the *Right* (index : i, R), and
4) out of the quantum dot, being *finally* on the *Right* (index : f, R).
The energy balance equations corresponding to these processes are

$$E_{p,N}^{i,L} = E_p + U(N+1) - U(N) + \eta eV \ , \tag{C.2a}$$

$$E_{p,N}^{f,L} = E_p + U(N) - U(N-1) + \eta eV \ , \tag{C.2b}$$

$$E_{p,N}^{i,R} = E_p + U(N+1) - U(N) - (1-\eta)\,eV \ , \tag{C.2c}$$

$$E_{p,N}^{f,R} = E_p + U(N) - U(N-1) - (1-\eta)\,eV \ , \tag{C.2d}$$

where N is the number of electrons in the dot *before* the tunneling event and η is the fraction of the applied voltage that drops over the left barrier (Fig. 5.1). E_p is the single particle eigen-energy of the quantum level p.

Occupation number notation: The usual[34,70] notation for many-electron Slater determinants is formulated in terms of Fermi-particle destruction and creation operators. Given, for example, two spin-degenerate quantum states, the Slater determinants are usually denoted as $|n_{1\uparrow}, n_{1\downarrow}, n_{2\uparrow}, n_{2\downarrow}\rangle$, where the n_i can take on only values 0 and 1. For this particular example with a maximum of 4 fermions in a limited basis set of 4 states we have $2^4 = 16$ possible Slater determinants. Here we are interested in the average population of these Slater determinant states, given that they are weakly coupled to two leads. The system of equations to be solved is of dimension 16×16. Several of these 16 states are equally occupied, for example $|1,0,0,0\rangle$ and $|0,1,0,0\rangle$, if the coupling to the leads is spin independent. Figure C.1 depicts all 16 states and groups them according to equal occupation probability. Instead of the 16 unknowns, only 9 unknowns have to be calculated. We introduce a new notation for these 9 groups, in which we simply count the number of electrons in the degenerate subgroup, as indicated in the example in Figure C.1. The 9 possible configurations are now described by 2 numbers $\{m_1, m_2\}$, where $m_1 = n_{1\uparrow} + n_{1\downarrow}$ and $m_2 = n_{2\uparrow} + n_{2\downarrow}$. Each "state" m_1 and m_2 is two-fold degenerate and its index can take on values 0, 1 and 2. Including also lateral state degeneracies as well as the spin degeneracies we have discussed

$\mid n_{1\uparrow}\, n_{1\downarrow}\, n_{2\uparrow}\, n_{2\downarrow}\rangle\ \}\xrightarrow{cd}\ \{m_1 m_2\}$	
$\mid 0\,0\,0\,0\rangle\quad\}\xrightarrow{1}\{0,0\}$	$\left.\begin{array}{l}\mid 1\,0\,1\,0\rangle\\ \mid 1\,0\,0\,1\rangle\\ \mid 0\,1\,1\,0\rangle\\ \mid 0\,1\,0\,1\rangle\end{array}\right\}\xrightarrow{4}\{1,1\}$
$\left.\begin{array}{l}\mid 1\,0\,0\,0\rangle\\ \mid 0\,1\,0\,0\rangle\end{array}\right\}\xrightarrow{2}\{1,0\}$	
$\left.\begin{array}{l}\mid 0\,0\,1\,0\rangle\\ \mid 0\,0\,0\,1\rangle\end{array}\right\}\xrightarrow{2}\{0,1\}$	$\left.\begin{array}{l}\mid 1\,1\,1\,0\rangle\\ \mid 1\,1\,0\,1\rangle\end{array}\right\}\xrightarrow{2}\{2,1\}$
$\mid 1\,1\,0\,0\rangle\quad\}\xrightarrow{1}\{2,0\}$	$\left.\begin{array}{l}\mid 1\,0\,1\,1\rangle\\ \mid 0\,1\,1\,1\rangle\end{array}\right\}\xrightarrow{2}\{1,2\}$
$\mid 0\,0\,1\,1\rangle\quad\}\xrightarrow{1}\{0,2\}$	$\mid 1\,1\,1\,1\rangle\quad\}\xrightarrow{1}\{2,2\}$

Figure C.1 Example of a compression of non-degenerate to degenerate state notation. Orbitals (n_1, n_2) and (n_3, n_4) are each assumed to be degenerate in energy and coupling to the leads. The new configuration (m_1, m_2) has $m_1 = n_1 + n_2$ and $m_2 = n_3 + n_4$ with the configuration degeneracy, cd, as indicated above the arrows. 16 configurations were converted to 9. We use this scheme to convert the $2^{26} = 6.7 \times 10^6$ non-degenerate configurations for 26 electrons (Fig. 5.5) to 8.4×10^4 configurations in the degenerate notation.

above, that our system consists of five 4-fold and three 2-fold degenerate states. We denote each "state" m_p to have the degeneracy d_p and the index m_p can take on values $\{0 \dots d_p\}$. While the reduction from 16 to 9 configurations does not appear significant, larger systems show a dramatic reduction. As discussed above we reduce our system from $2^{26} = 67,108,864$ to $\prod_{p=1}^{N_{group}}(d_p + 1) = 5^5 \times 3^3 = 84,375$, which is a reduction by a factor of about 800. To keep track of the multiple degeneracies we have introduced the configuration degeneracy, cd, as indicated in Fig. C.1. The configuration degeneracy, cd, takes on values of 1,2 and 4, depending on the configuration $\{m_1, m_2\}$ in the example in Fig. C.1. Formally, the configuration degeneracy, $cd\{m_1, m_2, \dots, m_{N_{group}}\}$, can be defined as a product over binomial coefficients $^{d_p}C_{m_p} = \frac{d_p!}{m_p!(d_p - m_p)!}$.

$$cd(\{m_k\}) = \prod_{p=1}^{N_{group}} {}^{d_p}C_{m_p} \ , \tag{C.3}$$

where we use short form $\{m_k\} = \{m_1, m_2, \dots, m_p, \dots, m_{N_{group}}\}$ and $m_p \in \{0 \dots d_p\}$.

  Current: Given the probability of occupation of each configuration $P(\{m_k\})$ and a Fermi-Dirac distribution in the reservoirs of $f(E) = \left[1 + exp\left(\frac{E - E_F}{k_B T}\right)\right]^{-1}$ the current through the left barrier (which equals the current through the right barrier) is given by

$$I = -e \sum_{\{m_k\}} cd(\{m_k\})\, P(\{m_k\}) \sum_{p=1}^{N_{group}} (d_p - m_p)\, \Gamma_{p,N}^{i,L} f_{p,N}^{i,L} - m_p \Gamma_{p,N}^{f,L}\left(1 - f_{p,N}^{f,L}\right) \ , \tag{C.4}$$

where m_p is the number of electrons in group p, N_{group} is the number of quantum levels considered (8 on our case, see Fig. 5.5), d_p is degeneracy of each single level and $cd(\{m_k\})$

indicates the configuration degeneracy. Γ and f carry four indices indicating the energy dependence of the transition as indicated in Eq. (C.2). The index p on Γ is also used to keep track of the lateral mode dependent, i.e. state dependent, coupling to the subbands in the leads.

    Rate-Equations: The set of rate-equations that needs to be solved including the degeneracy read

$$
\begin{aligned}
0 \;=\;& \frac{\partial}{\partial t} P(\{m_k\}) = \\
&- \sum_p P(\{m_k\}) \; (d_p - m_p) \; \left\{ \Gamma_{p,N}^{i,L} f_{p,N}^{i,L} + \Gamma_{p,N}^{i,R} f_{p,N}^{i,R} \right\} \\
&- \sum_p P(\{m_k\}) \; m_p \; \left\{ \Gamma_{p,N}^{f,L} \left[1 - f_{p,N}^{f,L} \right] + \Gamma_{p,N}^{f,R} \left[1 - f_{p,N}^{f,R} \right] \right\} \\
&+ \sum_p P(\ldots, m_{p-1}, m_p+1, m_{p+1}, \ldots) (d_p - m_p) \\
&\qquad\qquad \left\{ \Gamma_{p,N+1}^{f,L} \left[1 - f_{p,N+1}^{f,L} \right] + \Gamma_{p,N+1}^{f,R} \left[1 - f_{p,N+1}^{f,R} \right] \right\} \\
&+ \sum_p P(\ldots, m_{p-1}, m_p-1, m_{p+1}, \ldots) \; m_p \; \left\{ \Gamma_{p,N-1}^{i,L} f_{p,N-1}^{i,L} + \Gamma_{p,N-1}^{i,R} f_{p,N-1}^{i,R} \right\} \\
&- cd(\{m_k\}) \; \frac{P(\{m_k\}) - P_0(\{m_k\})}{\tau} \;, \forall \{m_k\} \,.
\end{aligned}
\tag{C.5}
$$

The set of equations (C.5) contains $\prod_{p=1}^{N_{group}}(d_p+1)$ equations for the same number of unknowns. However, one of the equations is a linear combination of the others and the system is under-determined by one equation. The normalization of the probabilities to 1 closes the system

$$
\sum_{\{m_k\}} cd(\{m_k\}) \; P(\{m_k\}) = 1 \,.
\tag{C.6}
$$

Equation (C.6) is equivalent to Eq. (2.12) in reference[70] except for the phenomenological intra quantum dot relaxation and the degenerate state notation. The canonical probability distribution $P_0(\{n_i\})$ depends on the free energy of the internal degrees of freedom with a fixed number of electrons in the quantum dot and the probability to have that particular number

$$
P_0(\{m_k\}) = \frac{cd(\{m_k\}) \; exp\left(\frac{\sum_{p=1}^{\infty} E_p m_p}{k_B T} \right)}{\sum_{\{o_k\}} cd(\{o_k\}) \; exp\left(\frac{\sum_{p=1}^{\infty} E_p o_p}{k_B T} \right) \; \delta_{N, \sum_p o_p}} \; P(N) \,.
\tag{C.7}
$$

The probability $P(N)$ represents the probability to have a total number N electrons in the quantum dot regardless of electron configuration. It is the sum of all configurations with the total number of N electrons

$$
P(N) = \sum_{\{m_k\}} cd(\{m_k\}) \; P(\{m_k\}) \; \delta_{N, \sum_p m_p} \,.
\tag{C.8}
$$

The introduction of the relaxation rate couples all configurations with the same total number of electrons N with each other, since $P_0(\{m_k\})$ depends now on all configurations with N electrons $\left(\sum_{\{m_k\}} \delta_{N, \sum_p m_p} \right)$.

Initial Guess: In order to solve this large system of equations iteratively, we need to find a "good" guess for the solution. We obtain our guess for the most likely configuration by looking at the diagonal elements of the probability matrix C.5. The diagonal elements indicate the leakage of the corresponding configuration to other configurations. The configuration with the smallest leakage rate to other configurations is the most stable one and will be the most likely one to occur. We use this physical argument to justify our initial guess of probability distribution and achieve satisfactory convergence in the iterative procedure.

C.3 Strong Inelastic Scattering

Beenakker[70] has given equations for the non-equilibrium number of electrons in the quantum dot similar to Averin.[69] We continue to use the same notation and extend Beenakker's[70] equation (5.1) to multiple degeneracy. The modified equation reads now

$$P(N+1) \sum_{p=1}^{N_{group}} F_{eq}(E_p|N+1) \left\{ \Gamma_{p,N+1}^{f,L} \left[1 - f_{p,N+1}^{f,L} \right] + \Gamma_{p,N+1}^{f,R} \left[1 - f_{p,N+1}^{f,R} \right] \right\}$$

$$= P(N) \sum_{p=1}^{N_{group}} [d_p - F_{eq}(E_p|N)] \left[\Gamma_{p,N}^{i,L} f_{p,N}^{i,L} + \Gamma_{p,N}^{i,R} f_{p,N}^{i,R} \right] , \qquad \text{(C.9)}$$

where $F_{eq}(E_p|N)$, the equilibrium probability to find state p occupied, given that N electrons are in the quantum dot, is defined as

$$F_{eq}(E_p|N) = \frac{\sum_{\{m_k\}} \delta_{N, \sum_i m_i} \; (1 - \delta_{m_p,0}) \; cd(\{m_i\}) \; exp\left(\frac{\sum_{i=1}^{N_{group}} E_i m_i}{k_B T} \right)}{\sum_{\{m_i\}} \delta_{N, \sum_i m_k} \; cd(\{m_k\}) \; exp\left(\frac{\sum_{i=1}^{N_{group}} E_i m_i}{k_B T} \right)} . \qquad \text{(C.10)}$$

The set of N Equations (C.9) for $N+1$ unknowns is closed by the normalization condition

$$\sum_{N=0}^{N_{total}} P(N) = 1 . \qquad \text{(C.11)}$$

After solving for $P(N)$ with Eqs. (C.9) and (C.11) we use Eq. (C.7) to determine $P(\{m_k\}) = P_0(\{m_k\})$ and evaluate the current through the structure using Eq. (C.4).

C.4 Constant Charging Interaction

Several calculations of the many-body eigen energies of quantum dots have been performed.[134–140] The critical ingredient in these calculations is the form of the electron-electron interaction potential. The cited references differ in their choices of this potential.

Many-body spectra using the un-screened[134, 135] Coulomb potential, $\frac{1}{|\vec{r}_i - \vec{r}_j|}$, were analyzed first and strong spatial electron-electron correlations were found in the case of comparable interaction energy and single-electron quantum state spacing. The many-body ground state has significant contributions of excited single-particle states indicating that electrons arrange themselves spatially to reduce the charging energy in this limit. Johnson et *al* introduced[136, 137] a modified interaction potential of parabolic form. The problem becomes exactly solvable and its results have been shown to be comparable[138] to the Coulomb potential interaction in the limit of strong confinement. Häusler[139] has used a screened interaction potential of the form $\frac{1}{\left((|\vec{r}_i - \vec{r}_j|^2 + \lambda^2)\right)^{1/2}}$ and pointed out the limitations of the state independent charging model.

The purpose of this section is to relate the state independent charging energy to the microscopic calculations. Starting from there we argue similar to a discussion in Ref. [134] that the simple charging model may give reasonable results for structures in which the single particle quantization energy is the dominant energy scale. Figure C.2 depicts the
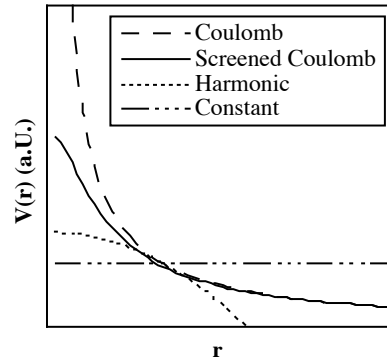
Figure C.2 Electron-electron charge interaction potentials $V(r)$. Screened and un-screened Coulomb, harmonic, and constant potential.

forms of the three investigated electron-electron potentials: un-screened Coulomb, screened Coulomb, and parabolic potential. If the region of confinement is small and screening by spatially closely located ground planes is reasonable to assume, then a constant interaction potential as indicated by a horizontal line in Figure C.2 may be a reasonable assumption.

Starting with the definitions of one- and two-electron integrals over spin and spatial orbitals in Szabo[34] on pg. 68 we substitute the two-electron operator r_{ij}^{-1} by a spatially independent constant U and calculate the N-particle Hamiltonian matrix on the basis set of N-particle Slater determinants. The choice of orthonormal single particle basis set for the generation of the N-particle Slater determinants and the spatially independent electron-electron interaction potential allows an easy analytic calculation of the Hamiltonian matrix elements. The Hamiltonian matrix turns out to be diagonal and with an expression for a N-particle Slater determinant denoted in configuration space as $\{n_i\} = \{n_1, n_2, \ldots, n_p\}$ we

obtain for the diagonal elements

$$E_{\{n_i\}} = \sum_i E_i \delta_{n_i,1} + \frac{U}{2} N (N-1) \qquad (C.12)$$

where E_i is the single-particle eigen-energy of the ith spin orbital. This approach allows a natural derivation of the charging energy expression (Eq. (C.1)) which we are using in this work. The charging energy of single electrons against image charges in surrounding ground planes is not considered here.

For our numerical simulations we chose the device parameters such that the single-particle energy separation, ΔE, is larger than the charging energy, U. This is the parameter region in which the constant charging interaction model is still valid.[134] In general we could implement a given many-body spectrum with all its ground states and excitations into the rate equation approach used here. However we feel that at this stage detailed calculations of state spectra may not improve our discussion on general phenomena discussed in this report. Also we feel that the confinement potentials and interaction potentials are not well enough known to justify detailed device calculations. Only to allow for a simplified discussion of the general charging phenomena in the case of a two-electron system we assume that the charging energy, U, is larger than the single-particle separation, ΔE, in the analytic section of the paper.

C.5 Rate Equations for 2 States

In Section C.2 we have laid out the model equations for an arbitrary number of states. We will now specialize these equations for the case of 2 single-particle non-degenerate states. The set of kinetic equations (C.5) for two states represented by $\{n_1, n_2\}$ corresponding to the single-particle energies $\{E_1, E_2\}$ reduces to four equations. Eq. (C.13), for example, models the time evolution of the probability distribution $P_{1,0}$ ($P(\{n_1, n_2\})$ was shortened to P_{n_1,n_2}), where we have denoted the energy and state dependence of the Fermi factors, f, and transition rates, Γ, according to Figure 5.2 via indices $1 \dots 4$

$$
\begin{aligned}
0 \quad = \quad & \frac{\partial}{\partial t} P_{1,0} = \\
\{1,0\} \rightarrow \{1,1\} : \quad & - \quad P_{1,0} \{\Gamma_{L,4} f_{L,4} + \Gamma_{R,4} f_{R,4}\} \\
\{1,0\} \rightarrow \{0,0\} : \quad & - \quad P_{1,0} \{\Gamma_{L,1} [1 - f_{L,1}] + \Gamma_{R,1} [1 - f_{R,1}]\} \\
\{1,1\} \rightarrow \{1,0\} : \quad & + \quad P_{1,1} \{\Gamma_{L,4} [1 - f_{L,4}] + \Gamma_{R,4} [1 - f_{R,4}]\} \\
\{0,0\} \rightarrow \{1,0\} : \quad & + \quad P_{0,0} \{\Gamma_{L,1} f_{L,1} + \Gamma_{R,1} f_{R,1}\} \\
\text{relaxation} : \quad & - \quad \frac{P_{1,0} - P_{1,0;eq}}{\tau} \ ,
\end{aligned}
\qquad (C.13)
$$

$P_{1,0}$ decreases in time due to evolution to $\{1,1\}$ and $\{0,0\}$ configurations ("-" sign). $P_{1,0}$ increases in time due to transitions from states $\{1,1\}$ and $\{0,0\}$ ("+" sign). Relaxation tries to bring the non-equilibrium distribution of constant N back to equilibrium. The other

three equations for the time development of $P_{0,0}$, $P_{0,1}$, and $P_{1,1}$ are very similar. For the solution of P_{n_1,n_2} one of the four equations is redundant and the system is closed by the normalization condition

$$1 = P_{0,0} + P_{1,0} + P_{0,1} + P_{1,1} \tag{C.14}$$

We simplify the kinetic equations like Eq. (C.13) further for the double barrier structure depicted in Figure 5.3a. The single-particle state energies are assumed to be above the Fermi-sea in the left and the right. The quantum dot is therefore empty in flat band condition $(E_1 - E_F \gg k_B T)$. To simplify the analytical work we assume that the bias is applied such that the conduction band on the left side is pulled under the conduction band on the right side (Fig. 5.1). We therefore assume $f_{L,1} = f_{L,2} = f_{L,3} = f_{L,4} = 0$ such that electrons can always tunnel to the left (collector), but there is no electron flow back from the left. The energy balance equations for tunneling through the right barrier include the critical excitation energies that we discussed in Section C.2. We have abbreviated the corresponding Fermi functions as

$$f_1 \;=\; f_{R,1} = f\left(E_{1,0}^{i,R}\right) = f\left(E_{1,1}^{f,R}\right) = f(E_1 - (1-\eta)\,eV)\ , \tag{C.15a}$$

$$f_2 \;=\; f_{R,2} = f\left(E_{2,0}^{i,R}\right) = f\left(E_{2,1}^{f,R}\right) = f(E_2 - (1-\eta)\,eV)\ , \tag{C.15b}$$

$$f_3 \;=\; f_{R,3} = f\left(E_{1,1}^{i,R}\right) = f\left(E_{1,2}^{f,R}\right) = f(E_1 + U - (1-\eta)\,eV)\ , \tag{C.15c}$$

$$f_4 \;=\; f_{R,4} = f\left(E_{1,1}^{i,R}\right) = f\left(E_{2,2}^{f,R}\right) = f(E_2 + U - (1-\eta)\,eV)\ , \tag{C.15d}$$

where $U = U(2) - U(1)$ with Eq. (C.1).

We have made the same simplification in notation with respect to the right barrier transmission rate $\Gamma_R(E) = \Gamma_R \times \Theta(E)$. All energies are measured against the right/emitter conduction band. For electron energies smaller than zero we assume a zero transmission rate, since tunneling under the emitter conduction band edge is not allowed. We further simplify the transmission rate through the left barrier Γ_L to be completely energy independent, $\Gamma_L(E) = \Gamma_L$.

Some other simplifications can be introduced with respect to inelastic scattering. Inelastic scattering couples only states $\{1, 0\}$ and $\{0, 1\}$ (Fig. 5.2). Using Eq. (C.7) for $P_{1,0;eq}$ we have for the relaxation contribution in Eq. (C.13)

$$P_{1,0} - P_{1,0;eq} = P_{1,0} - \frac{exp\left(-\frac{E_1}{k_B T}\right)}{exp\left(-\frac{E_1}{k_B T}\right) + exp\left(-\frac{E_2}{k_B T}\right)}\,(P_{1,0} + P_{0,1}) = d_2 P_{1,0} - d_1 P_{0,1}\ ; \tag{C.16}$$

where we have defined $d_1 = \frac{exp(-E_1/k_B T)}{exp(-E_1/k_B T) + exp(-E_2/k_B T)}$ and $d_2 = 1 - d_1$. Note that the limit $E_2 - E_1 \gg k_B T$ results in $d_1 \to 1$ and $d_2 \to 0$ indicating the thermal occupation probability of E_1 and E_2, respectively, given $N = 1$. With all these simplifications we can now contract

the rate-equations for $P_{0,0}$, $P_{1,0}$, $P_{0,1}$ and Eq. (C.14) into a matrix form

$$
\begin{pmatrix}
-(\Gamma_1 f_1 + \Gamma_2 f_2) & (\Gamma_L + \Gamma_1(1-f_1)) & (\Gamma_L + \Gamma_2(1-f_2)) & 0 \\
\Gamma_1 f_1 & -\left(\Gamma_4 f_4 + \Gamma_L + \Gamma_1(1-f_1) + \frac{d_2}{\tau}\right) & \frac{d_1}{\tau} & (\Gamma_L + \Gamma_4(1-f_4)) \\
\Gamma_2 f_2 & \frac{d_2}{\tau} & -\left(\Gamma_3 f_3 + \Gamma_L + \Gamma_2(1-f_2) + \frac{d_1}{\tau}\right) & (\Gamma_L + \Gamma_3(1-f_3)) \\
1 & 1 & 1 & 1
\end{pmatrix}
\begin{pmatrix}
P_{0,0} \\
P_{1,0} \\
P_{0,1} \\
P_{1,1}
\end{pmatrix}
=
\begin{pmatrix}
0 \\
0 \\
0 \\
1
\end{pmatrix}
\quad \text{(C.17)}
$$

Eq. (C.17) needs to be solved for all P_{n_1,n_2} such that the current

$$
I = e\Gamma_L \left(P_{1,0} + P_{0,1} + 2\,P_{1,1}\right) = e\Gamma_L N \tag{C.18}
$$

can be calculated. Eq. (C.18) shows nicely how the current through the quantum dot scales directly with the filling N in the limit of energy independent barrier transmission. We have obtained a general solution for the current in Eq. (C.18) in terms of f_i, Γ_i, τ, and Γ_L. However it is quite lengthy and does not give any particular physical insight.

Section 5.2 discussed the transition energies in a 2 state system and Section 5.3.1 identified the voltage regions in which these transition energies can be excited by tunneling trough the right barrier. The applied voltage enters the system of equations (C.17) via the the occupation factors, f_i and Γ_i, defined in Eqs. (C.15). We consider $k_B T$ to be small and treat the occupation factors f_i and the transition rate Γ_i as step functions. $f_i = 1$ for energies under the Fermi-energy of the emitter, $\Gamma_i = \Gamma_R$ for energies above the conduction band edge of the emitter, and both quantities are zero otherwise. In the case of no charge interaction, $U = 0$, we start with the the values of f and Γ in each voltage region noted in Table C.1. Note that $E_3 = E_1 + U = E_1$ and $E_4 = E_2 + U = E_2$ implies that $f_3 = f_1$, $f_4 = f_2$, $\Gamma_3 = \Gamma_1$, and $\Gamma_4 = \Gamma_2$ (see Eqs. (C.15)). The bottom line of Table C.1 indicates the labels for the analytical current expressions obtained with the corresponding coefficients. Using the notation $\Gamma_\tau = 1/\tau$ the three currents are

$$
I_1 = e\,\frac{\Gamma_L\,\Gamma_R}{\Gamma_L + \Gamma_R} \tag{C.19a}
$$

$$
I_2 = 2e\,\frac{\Gamma_L\,\Gamma_R}{\Gamma_L + \Gamma_R} \tag{C.19b}
$$

$$
I_3 = e\,\frac{\Gamma_L\,\Gamma_R\left[\Gamma_L\,(2\,\Gamma_L + \Gamma_R) + 2\,\Gamma_\tau\,(\Gamma_L + \Gamma_R\,\{1 - d_2\})\right]}{\Gamma_L\,\left[2\,\Gamma_L^2 + 3\,\Gamma_L\,\Gamma_R + \Gamma_R^2\right] + \Gamma_\tau\,\left[2\,\Gamma_L^2 + 2\,\Gamma_R\,\Gamma_L + \{1 - d_2\}\,\Gamma_R^2\right]} \tag{C.19c}
$$

Note that *only* the valley current I_3 is dependent on inelastic scattering (Γ_τ and d_2). Eq. (C.19c) has been series expanded in $\frac{1}{\tau} = \Gamma_\tau$ to yield Eq. (5.1) in the low temperature limit where $E_2 - E_1 \gg k_B T$ yields $d_2 \to 0$. An expansion for small scattering times $\tau = \frac{1}{\Gamma_\tau}$ yields Eq. (5.2).

Table C.2 contains the occupation coefficients, f, and the right barrier transmission rates, Γ_R, for the bias regions the correspond to different transitions in the case of large charging energy, $U > E_2 - E_1$. The last line indicates the labels for the corresponding current

Table C.1 Occupation factors, f, and transmission rates, Γ_R, in the no-charging case, $U = 0$, for the relevant bias ranges. Entries for I_i correspond to Eqs. (C.19).

$\alpha V + E_F$	$[0,E_1]$	$[E_1,E_2]$	$[E_2,E_1+E_F]$	$[E_1+E_F,E_2+E_F]$	$[E_2+E_F,\infty]$
$f_1 = f_3$	0	1	1	1	1
$f_2 = f_4$	0	0	1	1	1
$\Gamma_1 = \Gamma_3$	Γ_R	Γ_R	Γ_R	0	0
$\Gamma_2 = \Gamma_4$	Γ_R	Γ_R	Γ_R	Γ_R	0
I	0	I_1	I_2	I_3	0

Equations (C.20). The currents are

$$I_1 = e\frac{\Gamma_L\,\Gamma_R\,(\Gamma_L+\Gamma_R+\Gamma_\tau)}{(\Gamma_L+\Gamma_R)^2 + \Gamma_\tau\,(\Gamma_L+\{1+d_2\}\,\Gamma_R)} \quad \xrightarrow{d_2 \to 0} \quad e\frac{\Gamma_L\,\Gamma_R}{\Gamma_L+\Gamma_R} \tag{C.20a}$$

$$I_2 = e\frac{\Gamma_L\,2\,\Gamma_R}{\Gamma_L+2\,\Gamma_R} \tag{C.20b}$$

$$I_3 = 2e\frac{\Gamma_L\,\Gamma_R\,[(2\,\Gamma_L+\Gamma_R)\,(\Gamma_L+\Gamma_R) + \Gamma_\tau\,(2\,\Gamma_L+\{1+2\,d_2\}\,\Gamma_R)]}{2\,(\Gamma_L+\Gamma_R)^3 + \Gamma_\tau\,(2\,\Gamma_L^2+5\,\Gamma_L\,\Gamma_R+2\,(1+d_2)\,\Gamma_R^2)} \tag{C.20c}$$

$$I_4 = 2e\frac{\Gamma_L\,\Gamma_R}{\Gamma_L+\Gamma_R} \tag{C.20d}$$

$$I_5 = 2e\frac{\Gamma_L\,\Gamma_R\,(\Gamma_L+\Gamma_R)}{2\,\Gamma_L^2+2\,\Gamma_L\,\Gamma_R+\Gamma_R^2} \tag{C.20e}$$

Note that *only* I_1 and I_3 are explicitly dependent on inelastic scattering (Γ_τ and d_2). The perturbation due to relaxation on current I_1 is vanishing with $d_2 \to 0$. Current I_3 has been series expanded in $\tau = \frac{1}{\Gamma_\tau}$ to yield Eq. (5.5) for the limit of strong inelastic scattering. For the limit of small inelastic scattering a series expansion in $\Gamma_\tau = \frac{1}{\tau}$ Eq. (5.6) has been obtained.

Table C.2 Occupation factors, f, and transmission rates, Γ_R, for the limit $U > E_2 - E_2$. Entries for I_i correspond to Eqs. (C.20).

$\alpha V + E_F$	$[0,E_1]$	$[E_1,E_2]$	$[E_2,E_1+U]$	$[E_1+U,E_2+U]$	$[E_2+U,E_1+E_F]$	$[E_1+E_F,E_2+E_F]$	$[E_2+E_F,\infty]$
f_1	0	1	1	1	1	1	1
f_2	0	0	1	1	1	1	1
f_3	0	0	0	1	1	1	1
f_4	0	0	0	0	1	1	1
Γ_1	Γ_R	Γ_R	Γ_R	Γ_R	Γ_R	0	0
Γ_2	Γ_R	Γ_R	Γ_R	Γ_R	Γ_R	Γ_R	0
Γ_3	Γ_R	Γ_R	Γ_R	Γ_R	Γ_R	Γ_R	Γ_R
Γ_4	Γ_R	Γ_R	Γ_R	Γ_R	Γ_R	Γ_R	Γ_R
I	0	I_1	I_2	I_3	I_4	I_5	0

Appendix D

Analytical Treatment of the Coupled Quantum Dot System

D.1   Introduction

We now consider the mathematical analysis of the coupled dot system consisting of one doubly spin-degenerate state in each quantum dot. We are solving the Hamiltonian in Eq. (6.1) exactly in the terms $H_D + H_C$. The coupling to the leads is assumed to be weak enough such that it can be treated in first-order perturbation theory. The temperature is assumed to be high enough such that correlations of electrons in the quantum dot system and lead electrons can be neglected. We denote the electronic states in the quantum dot as Slater determinants without any k-state notation of the adjoining leads. The notation for the many-particle Slater determinants is $|n_{1\uparrow}, n_{1\downarrow}, n_{2\uparrow}, n_{2\downarrow}\rangle$ where the subscript 1(2) is the label of the left (right) quantum dot, respectively and $\uparrow$ and $\downarrow$ are spin-indices in a limited set of basis states. The next highest lateral states are assumed to be separated in their decoupled eigen-energy, such that they do not need to be included in this analysis. Given these 4 occupation numbers we have $2^4 = 16$ possible configurations. The number of particles in the central quantum system, can only change by tunneling processes from the leads. These processes are assumed to be weak and we only treat the inner quantum-dot system described by $H_D + H_C$ exactly in the sub-set of constant numbers of electrons $N = const$. The dimensions in terms of basis states of these sub-sets are $D \in \{1, 4, 6, 4, 1\}$ for $N \in \{0, 1, 2, 3, 4\}$.

D.2   The Sub-Set Hamiltonians

The basis Set for $N = 1$ sub-set of states consists of 4 states: $|1, 0, 0, 0\rangle_1$, $|0, 1, 0, 0\rangle_2$, $|0, 0, 1, 0\rangle_3$, and $|0, 0, 0, 1\rangle_4$. The order given by the subscripts is the one in which the Hamiltonian matrix is formatted as well. The basis state $|1, 0, 0, 0\rangle_1$, for example will have a diagonal element $_1\langle 1, 0, 0, 0|H_D + H_C|1, 0, 0, 0\rangle_1 = \epsilon_1 = H_{1,1}^1$, where the superscript 1 indicates the $N = 1$ sub-set here. The single particle eigen-energies of the states in the the two

quantum dots are ϵ_1 and ϵ_2. The inter-dot coupling Hamiltonian, H_C, couples only states with the same spin in the neighboring dots. The $|1,0,0,0\rangle_1$ state is therefore coupled only to the $|0,0,1,0\rangle_3$ state. The corresponding matrix element is $_1\langle 1,0,0,0|H_D+H_C|0,0,1,0\rangle_3 = t = H^1_{1,3}$. With these two examples, we can see how the Hamiltonian of the $N=1$ sub-set takes on the following form

$$H^1 = \begin{pmatrix} \epsilon_1 & 0 & t & 0 \\ 0 & \epsilon_1 & 0 & t \\ t & 0 & \epsilon_2 & 0 \\ 0 & t & 0 & \epsilon_2 \end{pmatrix} . \tag{D.1}$$

The basis set for $N=2$ sub-set of states consists of $|1,1,0,0\rangle_1, |1,0,1,0\rangle_2$, $|1,0,0,1\rangle_3$, $|0,1,1,0\rangle_4$, $|0,1,0,1\rangle_5$, and $|0,0,1,1\rangle_6$ and the Hamiltonian can be denoted in a similar matrix form as the $N=1$ case, but with dimension 6×6

$$H^2 = \begin{pmatrix} 2\epsilon_1+U_1 & 0 & t & t & 0 & 0 \\ 0 & \epsilon_1+\epsilon_2+W & 0 & 0 & 0 & 0 \\ t & 0 & \epsilon_1+\epsilon_2+W & 0 & 0 & t \\ t & 0 & 0 & \epsilon_1+\epsilon_2+W & 0 & 0 \\ 0 & 0 & 0 & 0 & \epsilon_1+\epsilon_2+W & 0 \\ 0 & 0 & t & t & 0 & 2\epsilon_2+U_2 \end{pmatrix}, \tag{D.2}$$

where U_1 (U_2) is the intra-dot charging energy in dot 1 (2) and W is the inter-dot charging energy. Note that the states $|1,0,1,0\rangle_2$ and $|0,1,0,1\rangle_5$ are decoupled[§] from the other states since all the up- and the down-spin states are occupied in these basis states. These two states will therefore be eigen-states of the coupled system as well.

The basis states for the $N=3$ sub-set are: $|1,1,1,0\rangle_1$, $|1,1,0,1\rangle_2$, $|1,0,1,1\rangle_3$, and $|0,1,1,1\rangle_4$ resulting in a Hamiltonian

$$H^3 = \begin{pmatrix} 2\epsilon_1+\epsilon_2+U_1+2W & 0 & t & 0 \\ 0 & 2\epsilon_1+\epsilon_2+U_1+2W & 0 & t \\ t & 0 & \epsilon_1+2\epsilon_2+U_2+2W & 0 \\ 0 & t & 0 & \epsilon_1+2\epsilon_2+U_2+2W \end{pmatrix} . \tag{D.3}$$

The $N=0$ sub-set Hamiltonian, eigen-value, and eigen-state are trivial with $H^0=(0)$, $E^0_1 = 0$, and $|\psi^0_1\rangle = |0,0,0,0\rangle$, respectively, since there is only one state in this basis set. The $N=4$ sub-set Hamiltonian, eigen-value, and eigen-state are similarly trivial with $H^4 = (2\epsilon_1+2\epsilon_2+U_1+U_2+4W)$, $E^4_1 = 2\epsilon_1+2\epsilon_2+U_1+U_2+4W$, and $|\psi^4_1\rangle = |1,1,1,1\rangle$.

[§]$H^2_{2,i\neq 2} = H^2_{i\neq 2,2} = 0$ and $H^2_{5,i\neq 5} = H^2_{i\neq 5,5} = 0$.

D.3 The Sub-Set Eigen-Values and Eigen-Vectors

The eigen-values and eigen-vectors of the Hamiltonian matrices H^i can be evaluated analytically using software tools like MAPLE or MATHEMATICA. The general expressions of these new eigen vectors are quite lengthy and do not lend significant insight into the physics. The simplified ideal system of identical quantum dots with $\epsilon_1 = \epsilon_2 = \epsilon$, $U_1 = U_2$ and no inter-dot charging, $W = 0$, provides physical insight into the coupled system eigen-vectors and eigen-values.

The $N = 1$ system is of dimension 4×4 and will be described by a bonding and anti-bonding state which is doubly degenerate. The bonding states have the eigen-energy $E_1^1 = E_2^1 = \epsilon - t$ with the corresponding two eigen-vectors

$$\left| \psi_1^1 \right\rangle = \frac{1}{\sqrt{2}} \begin{pmatrix} 1 \\ 0 \\ -1 \\ 0 \end{pmatrix} = \frac{1}{\sqrt{2}} \left(\left| 1,0,0,0 \right\rangle_1 - \left| 0,0,1,0 \right\rangle_3 \right) \tag{D.4a}$$

$$\left| \psi_2^1 \right\rangle = \frac{1}{\sqrt{2}} \begin{pmatrix} 0 \\ 1 \\ 0 \\ -1 \end{pmatrix} = \frac{1}{\sqrt{2}} \left(\left| 0,1,0,0 \right\rangle_2 - \left| 0,0,0,1 \right\rangle_4 \right) \tag{D.4b}$$

Note that the states are not mixed in spin components. The spin of $\left| \psi_2^1 \right\rangle$ and $\left| \psi_2^1 \right\rangle$ are purely up-spin and purely down-spin, respectively. The anti-bonding states have a higher eigen-energy of $E_3^1 = E_4^1 = \epsilon + t$ with the eigen-states

$$\left| \psi_3^1 \right\rangle = \frac{1}{\sqrt{2}} \begin{pmatrix} 1 \\ 0 \\ 1 \\ 0 \end{pmatrix} \tag{D.5a}$$

$$\left| \psi_4^1 \right\rangle = \frac{1}{\sqrt{2}} \begin{pmatrix} 0 \\ 1 \\ 0 \\ 1 \end{pmatrix} \tag{D.5b}$$

The eigen-values and eigen-vectors of the $N = 2$ system H^2 are somewhat more complicated. The ground state is non-degenerate with energy $E_1^2 = 2\epsilon - \frac{1}{2}(\Delta - U)$, where $\Delta = \sqrt{U^2 + 16t^2}$ and has an eigen-vector of

$$\left| \psi_1^2 \right\rangle = \frac{1}{2\sqrt{\Delta^2 + \Delta U}} \begin{pmatrix} U + \Delta \\ 0 \\ -4t \\ -4t \\ 0 \\ U + \Delta \end{pmatrix}$$

$$
\begin{aligned}
&= -\frac{1}{2}\sqrt{1+\frac{U}{\Delta}}\left(|1,0,0,1\rangle_3+|0,1,1,0\rangle_4\right) \\
&+ \frac{2t}{\sqrt{\Delta(\Delta+U)}}\left(|1,1,0,0\rangle_1+|0,0,1,1\rangle_6\right)
\end{aligned}
\tag{D.6}
$$

Note that the ground state consists of two groups of states. The first group with coefficients

$$
\frac{1}{2}\sqrt{1+\frac{U}{\Delta}} \approx \frac{1}{\sqrt{2}} - \sqrt{2}\left(\frac{t}{U}\right)^2 + O\left(\left(\frac{t}{U}\right)^4\right)
\tag{D.7a}
$$

consists of basis states that have one electron in each quantum dot ($|1,0,0,1\rangle_3$ and $|0,1,1,0\rangle_4$). Their strength in the ground state depends only weakly on the inter-dot coupling, t. These states do not have to "pay" the charging energy, U. The corresponding diagonal elements in H^2 ($H^2_{3,3}$ and $H^2_{4,4}$ in Eq. (D.2)) are 2ϵ. However, note that the total spin of these states is 0, consisting of one up-spin and one down-spin electron and they are *not* coupled to each other. In order to "utilize" the inter-dot coupling, t, states that "link" these two states, have to be mixed into the ground state. These links are: $|1,0,0,1\rangle_3 \leftrightarrow |1,1,0,0\rangle_1 \leftrightarrow |0,1,1,0\rangle_4$ and $|1,0,0,1\rangle_3 \leftrightarrow |0,0,1,1\rangle_6 \leftrightarrow |0,1,1,0\rangle_4$. However these "link"-states have to "pay" the charging energy, U, and are first order in $\frac{t}{U}$

$$
\frac{2t}{\sqrt{\delta^2+\Delta U}} \approx \sqrt{2}\frac{t}{U} - \left(O\left(\frac{t}{U}\right)^3\right) .
\tag{D.7b}
$$

The lowest excited states in the sub-set $N=2$ are grouped into a triplet of energy $E^2_2 = E^2_3 = E^2_4 = 2\epsilon$ with the corresponding states

$$
\left|\psi^2_2\right\rangle = \begin{pmatrix} 0 \\ 1 \\ 0 \\ 0 \\ 0 \\ 0 \end{pmatrix} = |1,0,1,0\rangle_2
\tag{D.8a}
$$

$$
\left|\psi^2_3\right\rangle = \begin{pmatrix} 0 \\ 0 \\ 0 \\ 0 \\ 1 \\ 0 \end{pmatrix} = |0,1,0,1\rangle_5
\tag{D.8b}
$$

$$
\left|\psi^2_4\right\rangle = \frac{1}{\sqrt{2}}\begin{pmatrix} 0 \\ 0 \\ 1 \\ -1 \\ 0 \\ 0 \end{pmatrix} = \frac{1}{\sqrt{2}}\left(|1,0,0,1\rangle_3-|0,1,1,0\rangle_4\right)
\tag{D.8c}
$$

Two states, $\left|\psi_2^2\right\rangle$ and $\left|\psi_3^2\right\rangle$, are decoupled from the other basis states as mentioned in Section D.2 with Eq. (D.2) and they have a total spin of ± 1. The third state in this triplet is a superposition of states $|1,0,0,1\rangle_3$ and $|0,1,1,0\rangle_4$ with a total spin of 0.

The fifth eigen vector of the coupled system with $N=2$ has an eigen-value of $E_5^2 = 2\epsilon + U$ with

$$\left|\psi_5^2\right\rangle \;=\; \frac{1}{\sqrt{2}} \begin{pmatrix} 1 \\ 0 \\ 0 \\ 0 \\ 0 \\ -1 \end{pmatrix} = \frac{1}{\sqrt{2}} \left(|1,1,0,0\rangle_1 - |0,0,1,1\rangle_6\right) \; . \tag{D.9}$$

It consists only of basis states with two electrons in each quantum dot with diagonal elements $2\epsilon + U$.

The sixth eigen state, $\left|\psi_6^2\right\rangle$, in the H^2 Hamiltonian is the anti-bonding state to the ground state, $\left|\psi_1^2\right\rangle$, with eigen-energy $E_6^2 = 2\epsilon + \frac{1}{2}\left(\Delta + U\right)$. The eigen vector is

$$\begin{aligned} \left|\psi_6^2\right\rangle \;=\;& \frac{1}{2\sqrt{\Delta^2 - \Delta U}} \begin{pmatrix} 4t \\ 0 \\ \Delta - U \\ \Delta - U \\ 0 \\ 4t \end{pmatrix} \\ =\;& \frac{1}{2}\sqrt{1 - \frac{U}{\Delta}}\left(|1,0,0,1\rangle_3 + |0,1,1,0\rangle_4\right) \\ +\;& \frac{2t}{\sqrt{\Delta(\Delta - U)}}\left(|1,1,0,0\rangle_1 + |0,0,1,1\rangle_6\right) \end{aligned} \tag{D.10}$$

The coefficients to basis states $|1,1,0,0\rangle_1$ and $|0,0,1,1\rangle_6$ are large with small inter-dot coupling, t (Eq. D.7a). The coefficients to the basis states $|1,0,0,1\rangle$ and $|0,1,1,0\rangle$ are small in $\frac{t}{U}$ (Eq. D.7b).

The $N=3$ sub-set Hamiltonian H^3 is identical in structure as the H^1 for the case of parameters discussed here. We therefore state only the eigen-values of $E_1^3 = E_2^3 = 3\epsilon + U - t$ and $E_3^3 = E_4^3 = 3\epsilon + U + t$. The bonding and anti-bonding structure of the eigen-states $\left|\psi_i^3\right\rangle$ is identical to the structure of the $\left|\psi_i^1\right\rangle$ states.

The $N=0$ ($N=4$) sub-set Hamiltonian H^0 (H^4) is trivial since it consists only of one basis state $|0,0,0,0\rangle$ ($|1,1,1,1\rangle$). The eigen-value is $E_1^0 = 0$ ($E_1^4 = 2\epsilon + 2U$).

D.4   Coupling to the Leads

After the spatially complicated eigen-states $|\psi_i^n\rangle$ have been calculated for the decoupled Hamiltonians, H^n, we will now calculate transition rates between these sub-sets in first-order perturbation. For convenience we repeat here the Tunneling Hamiltonian stated in Eq. (6.1)

$$H_T = H_{T,L\uparrow} + H_{T,L\downarrow} + H_{T,R\uparrow} + H_{T,R\downarrow} \tag{D.11a}$$

$$H_{T,L\uparrow} = \sum_{k \in L} \left(V_{k\uparrow}^L c_{1\uparrow}^\dagger c_{k\uparrow} + c.c. \right) \tag{D.11b}$$

$$H_{T,L\downarrow} = \sum_{k \in L} \left(V_{k\downarrow}^L c_{1\downarrow}^\dagger c_{k\downarrow} + c.c. \right) \tag{D.11c}$$

$$H_{T,R\uparrow} = \sum_{k \in R} \left(V_{k\uparrow}^R c_{2\uparrow}^\dagger c_{k\uparrow} + c.c. \right) \tag{D.11d}$$

$$H_{T,R\downarrow} = \sum_{k \in R} \left(V_{k\downarrow}^R c_{2\downarrow}^\dagger c_{k\downarrow} + c.c. \right) \tag{D.11e}$$

In our notation of basis states $|n_{1\uparrow}, n_{1\downarrow}, n_{2\uparrow}, n_{2\downarrow}\rangle$ of the quantum dot system we have not included any quantum numbers k indicating lead states. We separate the coupling to the left and the right lead and up- and down-spin and keep the sum over all k-states. We define $\Gamma_{nij}^L/\hbar$ as the transition rate from n-particle state i, ($|\psi_i^n\rangle$), to the $(n-1)$-particle state j, ($|\psi_j^{n-1}\rangle$), through the left barrier as:

$$\Gamma_{nij}^L = 2\pi \sum_{k \in L} \left| V_k^L \right|^2 \delta\left(E - (E_i^n - E_j^{n-1}) \right) \left(|\langle \psi_j^{n-1} | c_{1\uparrow} | \psi_i^n \rangle|^2 + |\langle \psi_j^{n-1} | c_{1\downarrow} | \psi_i^n \rangle|^2 \right) \tag{D.12}$$

We treat the up-spin and the down-spin transition independently and assume that the coupling elements, V_k^L, are spin independent. The expression for the transmission rates through the right barrier is equivalent to the ones through the left barrier with a substitution of superscripts L by R and index 1 by 2 in Eq. (D.12).

The eigen-states $|\psi_i^n\rangle$ and $|\psi_j^{n-1}\rangle$ involved in this expression are a linear superposition of the basis states $|n_{1\uparrow}, n_{1\downarrow}, n_{2\uparrow}, n_{2\downarrow}\rangle$ in which the creation and destruction operators $c_{1\uparrow}$, $c_{1\uparrow}^\dagger$, $c_{1\downarrow}$, $c_{1\downarrow}^\dagger$, $c_{2\uparrow}$, $c_{2\uparrow}^\dagger$, $c_{2\downarrow}$, and $c_{2\downarrow}^\dagger$ are defined. In order to evaluate matrix elements of the sort $\langle \psi_j^{n-1} | c_{1\downarrow} | \psi_i^n \rangle$ we need to express the states $|\psi_i^n\rangle$ and $|\psi_j^{n-1}\rangle$ in terms of these basis states.

Before we state the general procedure in matrix notation we will consider two simple examples of the calculation of matrix elements for transitions between ground states. We consider first a $N = 0 \rightarrow 1$ transition from state $|\psi_1^0\rangle$ to $|\psi_1^1\rangle$ via transitions through the left barrier, i.e. via $c_{1\uparrow}$ and $c_{1\downarrow}$.

$$
\begin{aligned}
\langle \psi_1^0 | c_{1\uparrow} | \psi_1^1 \rangle &= \frac{1}{\sqrt{2}} \langle 0,0,0,0 | c_{1\uparrow} \left(|1,0,0,0\rangle - |0,0,1,0\rangle \right) \\
&= \frac{1}{\sqrt{2}} \left(\langle 0,0,0,0 | c_{1\uparrow} | 1,0,0,0\rangle - \langle 0,0,0,0 | c_{1\uparrow} | 0,0,1,0\rangle \right)
\end{aligned}
$$

$$= \frac{1}{\sqrt{2}} \left(\langle 0,0,0,0|0,0,0,0 \rangle - 0 \right)$$

$$= \frac{1}{\sqrt{2}}$$

$$\langle \psi_1^0|c_{1\downarrow}|\psi_1^1 \rangle = \frac{1}{\sqrt{2}} \langle 0,0,0,0|c_{1\downarrow} \left(|1,0,0,0\rangle - |0,0,1,0\rangle \right)$$

$$= \frac{1}{\sqrt{2}} \left(\langle 0,0,0,0|c_{1\downarrow}|1,0,0,0\rangle - \langle 0,0,0,0|c_{1\downarrow}|0,0,1,0\rangle \right)$$

$$= \frac{1}{\sqrt{2}} (0 - 0)$$

$$= 0$$

We therefore obtain for the transition rate through the left barrier

$$\Gamma_{111}^L \propto \left(\left| \langle \psi_1^0|c_{1\uparrow}|\psi_1^1 \rangle \right|^2 + \left| \langle \psi_1^0|c_{1\downarrow}|\psi_1^1 \rangle \right|^2 \right) = \frac{1}{2} \tag{D.13}$$

By symmetry we can obtain for the second degenerate $N=1$ ground state $|\psi_2^1\rangle$ the same transition rate

$$\Gamma_{121}^L \propto \left(\left| \langle \psi_1^0|c_{1\uparrow}|\psi_2^1 \rangle \right|^2 + \left| \langle \psi_1^0|c_{1\downarrow}|\psi_2^1 \rangle \right|^2 \right) = \frac{1}{2} \tag{D.14}$$

The values for the right barrier transmission rates are the same by symmetry. Note here that the the operator $c_{1\uparrow}$ connects only state $|1,0,0,0\rangle$ to state $|0,0,0,0\rangle$. The three other basis states $|0,1,0,0\rangle$, $|0,0,1,0\rangle$, and $|0,0,0,1\rangle$ do not connect to $|0,0,0,0\rangle$ via $c_{1\uparrow}$. So $c_{1\uparrow}$ connects 1 out of 4 basis states in the $N=1$ set to the one basis state of the $N=0$ set.

For the transitions between the $N=1$ and $N=2$ ground states the equations become a little bit more messy. We can calculate the $c_{1\downarrow}$ and $c_{1\uparrow}$ matrix elements for $|\psi_1^1\rangle$ to $|\psi_1^2\rangle$ transitions as

$$\langle \psi_1^1|c_{1\downarrow}|\psi_1^2 \rangle = \frac{1}{\sqrt{2}} \frac{1}{2\sqrt{\Delta^2+\Delta U}} \left(\langle 1,0,0,0| - \langle 0,0,1,0| \right) c_{1\downarrow}$$
$$\left[(U+\Delta) \left(|1,1,0,0\rangle + |0,0,1,1\rangle \right) - 4t \left(|1,0,0,1\rangle + |0,1,1,0\rangle \right) \right]$$
$$= \frac{1}{\sqrt{2}} \frac{1}{2\sqrt{\Delta^2+\Delta U}} \left((U+\Delta)\langle 1,0,0,0|c_{1\downarrow}|1,1,0,0\rangle \right.$$
$$\left. + 4t\langle 0,0,1,0|c_{1\downarrow}|0,1,1,0\rangle \right)$$
$$= \frac{4t+U+\Delta}{2\sqrt{2}\sqrt{\Delta^2+\Delta U}}$$

$$\langle \psi_1^1|c_{1\uparrow}|\psi_1^2 \rangle = 0$$

For the left barrier transition rate we therefore obtain:

$$\Gamma_{211}^L \propto \left(\left| \langle \psi_1^1|c_{1\downarrow}|\psi_1^2 \rangle \right|^2 + \left| \langle \psi_1^1|c_{1\uparrow}|\psi_1^2 \rangle \right|^2 \right)$$

$$= \frac{1}{8} \frac{\left(4t + U + \sqrt{U^2 + 16t^2}\right)^2}{16t^2 + U^2 + U\sqrt{U^2 + 16t^2}}$$

$$= \frac{1}{4} + \frac{t}{U} - 8\left(\frac{t}{U}\right)^3 + O\left(\left(\frac{t}{U}\right)^4\right)$$

By symmetry of the ground states we can show that all possible transitions between the 2 fold degenerate 1-particle ground state and the non-degenerate 2-particle ground state have the same value.

The operator $c_{1\downarrow}$ connects only few basis states in the $N = n \to n-1$ transition. For the case of a $N = 2 \to 1$ transitions, for example, we have $\langle 1, 0, 0, 0 | c_{1\downarrow} | 1, 1, 0, 0 \rangle = 1$ but $\langle 0, 1, 0, 0 | c_{1\downarrow} | 1, 1, 0, 0 \rangle = 0$. With 6 elements in the $N = 2$ sub-set and 4 elements in the $N = 1$ we can build a 4×6 matrix representation of $c_{1\downarrow}$, and similarly for the other three destruction operators $c_{1\uparrow}$, $c_{2\downarrow}$, and $c_{2\uparrow}$. The corresponding 4 destruction operators $c^\dagger_{1(2)\uparrow(\downarrow)}$ can be represented with a 6×4 matrix.

Given the vector representation of the eigen-states $|\psi_i^n\rangle$ as $[\psi_i^n]_{D_n \times 1}$ with dimension $D_n \times 1$ we can evaluate the matrix element now as

$$\langle \psi_j^{n-1} | c_{1\downarrow} | \psi_i^n \rangle = [\psi_j^{n-1}]^\dagger_{D_{n-1} \times 1} [c_{1\downarrow}]_{D_{n-1} \times D_n} [\psi_i^n]_{D_n \times 1} \tag{D.15}$$

This matrix representation can be readily implemented numerically. We have implemented this procedure for coupled quantum dots (see chapter 6) including lateral modes and chains of quantum dots.[89] A sparse matrix notation was used to facilitate vectorized product execution for the evaluation of the coupling elements, Γ.